STUDIES ON INTERFACIAL BEHAVIOR AND STRUCTURAL
TRANSFORMATIONS IN A REACTING MONOLAYER SYSTEM

By

STEPHEN AARON RELAYO CARINO

A DISSERTATION PRESENTED TO THE GRADUATE SCHOOL
OF THE UNIVERSITY OF FLORIDA IN PARTIAL FULFILLMENT
OF THE REQUIREMENTS FOR THE DEGREE OF
DOCTOR OF PHILOSOPHY

UNIVERSITY OF FLORIDA

2002

To Mama — thanks for everything

# TABLE OF CONTENTS

LIST OF TABLES

LIST OF FIGURES

Abstract of Dissertation Presented to the Graduate School
of the University of Florida in Partial Fulfillment of the
Requirements for the Degree of Doctor of Philosophy

STUDIES ON INTERFACIAL BEHAVIOR AND STRUCTURAL
TRANSFORMATIONS IN A REACTING MONOLAYER SYSTEM

By

Stephen Aaron Relayo Carino

August 2002

Chairman: Dr. Randolph S. Duran
Major Department: Chemistry

The network formation in trialkoxysilane monolayers at the air-water interface
has been the focus of contention over the years. While it can be intuitively assumed that a
network architecture is feasible, it is likely that the cross-linking in a 2D geometry may
not be as effective as in the bulk due to the geometrical restrictions around the silane
functional group. This work attempts to address this issue by investigating the surface
behavior and dynamics of film formation in a reacting n-octadecyltrimethoxysilane
(OTMS) monolayer system at the air-water interface.

Monolayer studies of OTMS showed that it forms a stable monolayer at the air-
water interface. When spread on an acidic subphase, a hydrolysis reaction is initiated and
observed to follow a general acid-catalyzed first-order kinetics. The subsequent conden-
sation reactions result in a cross-linked product, as determined from surface rheological
experiments consisting of compressional modulus and viscosity measurements. The re-
sults of rheological experiments also showed that the cross-linked product exhibited gross

behavior similar to a percolating network although the scaling behavior is different from that of the ideal system. Subsequent Brewster angle microscopy determined that the network architecture in this system is loose and dominated by linear segments.

Real time grazing incidence x-ray diffraction (GIXD) studies have shown that OTMS monolayer self-assembles into small domains showing characteristic in-plane ordering of close-packed alkyl chains in a hexagonal lattice. Further GIXD investigations have shown that the short-range positional ordering between the alkyl chains does not significantly change during the course of the reaction.

Overall, the study showed that the network formation is possible in this system although the creation of network junctions is indeed frustrated and inefficient. Considering the results from rheology and x-ray studies, it is speculated that the network junctions are found in the amorphous region and that the ordered domains are primarily made of linear segments and partially reacted OTMS.

# CHAPTER 1
## INTRODUCTION

The original motivation of this work was to investigate the surface behavior of an alkylalkoxysilanes surfactant, especially its behavior in the quasi–two-dimensional environment of a planar air-aqueous monolayer. Alkylalkoxysilane compounds have excellent adsorption to various substrates and therefore are most often used to modify surface properties of materials for various applications. For example, Finnie et al. used docosyltrichlorosilane compound to mask the surface of silicon to act as a chemical etch resist.[1] A similar application was undertaken by Zheng et al., in which the surface of a silicon substrate was modified by an alkylsilane prior to selective electrochemical etching.[2]

It would be interesting to correlate the results obtained from these monolayer studies to those of the curved interfaces of emulsions and microemulsions as applied to the preparation of core-shell particles. This class of particulate system designed to have a soft core and a hard silicate shell has promising applications as nanoscale vehicles for chemical delivery and recovery.

The method of preparing the core-shell particles would start with the alkylalkoxysilanes being dispersed in an oil/water mixture to create emulsion droplets. In this scheme, the alkoxysilane functional group is expected to be at the oil-water interface while the alkyl groups would be solubilized within the oil core. By polymerizing the alkoxysilane groups, the droplets are expected to be stabilized against coalescence and phase separation.

The above-described process should depend greatly on the extent of polymerization of the alkoxysilane groups. Thus, one aspect of this work is laid out.

Another interest that has motivated this work is the mechanism of formation of alkoxysilane self-assembled monolayers (SAM) on metal oxide surfaces. Several researchers[3-7] have investigated these phenomena in detail and the plausible mechanism involves the formation of a Langmuir monolayer-like intermediate[8] that eventually gets adsorbed to the oxide surface. Hence, by spreading alkoxysilanes at the air-water interface, it might be possible to investigate the intrinsic mechanism involved in the lateral growth of these types of SAM.

In the succeeding chapters, a thorough discussion on the various aspects of this work will be presented. A discussion on the nature of Langmuir films is given in Chapter 2. This chapter also covers some historical background as well as a review of recent literature on the area.

Experimental instrumentation and various characterization techniques are the topics of Chapter 3. The discussion is divided into three main sections encompassing basic isotherm measurements, rheological measurements as applied to monolayers, and finally techniques to characterize morphology and structure in Langmuir monolayers. Emphasis is given to techniques that are significant to this work although certain alternative and complementary techniques are also discussed to broaden the background on the topic.

Chapter 4 is the first of two parts where actual experimental results are discussed. It is in this chapter that the chemistry and surface behavior of alkoxysilanes will be addressed. A discussion on surface viscometry and on the determination of instantaneous compressibility modulus in a reacting monolayer is explored.

Chapter 5 is the other half of the results and discussion section and covers mostly x-ray diffraction work done at the Advanced Photon Source at Argonne National Laboratories. This particular section arose after recognizing the significance of x-ray structural studies towards understanding the mechanism of film growth in the monolayers.

Finally, Chapter 6 presents a summary of this work and recommendations for future work.

CHAPTER 2

LANGMUIR MONOLAYERS: STRUCTURE AND PHASE BEHAVIOR

The phenomenon of monolayer adsorption of surface-active molecules at the air-water interface had been noted since about 100 A.D. during the times of Pliny the Elder and Plutarch. Dynarowicz-Latka et al. describes some ancient references to oil film spreading on water.[9]

Surface-active molecules are usually lipids, fatty acids and proteins but they can also be any molecules with polar functional group at one end attached to a substantially non-polar moiety. Generally, these molecules are called *surfactants*, because of their surface activity or *amphiphiles* due to their dual hydrophilic and lipophilic character. In rare instances, these compounds are also called by these names: association colloids; colloidal electrolytes; paraffin chain salts; and tensides.

The historical background related to Langmuir monolayers at the air/water interface is discussed in various books, including those of Gaines,[10] Davis and Rideal,[11] Adam,[12] and many others. Several other related books also cover this topic along with an extensive discussion of Langmuir-Blodgett films, the term that applies to Langmuir films that have been transferred on to solid substrates.[13-15]

The first reported scientific study of "oily films" on water was made by Benjamin Franklin in 1774.[16] Based on the simple estimate of the area covered by a given amount of oil, he concluded that the film is monomolecularly thick. Centuries later in 1917, Langmuir[17] developed a theoretical framework and experimental methods to investigate the behavior of insoluble monolayers. His work was recognized with the 1932 Nobel

Prize in Chemistry and was the basis of numerous subsequent studies in the intervening decades.

Other significant works related to this area are summarized in the table below.

Table 2-1. Important seminal works in Langmuir and Langmuir-Blodgett research

| 1891 | Agnes Pockels[18] described a method of manipulating oil films on water. |
| 1899 | Lord Rayleigh[19] proposed that the films were only one molecule thick. |
| 1912 | Hardy[20,21] noted that only oil with polar functional groups will spread on water. |
| 1913 | Devaux[22] speculated that films behave both as liquid and solid. |
| 1916 | Langmuir[23] published papers responsible for laying out the scientific foundation of monolayer films |
| 1919 | Blodgett[24] transferred monolayer films to solid substrates; work was not published until 1935 |
| 1941-1945 | Harkins and Copeland;[25] Stållberg-Stenhagen and Stenhagen;[26] and Adam;[12] published seminal works on the phase transitions in monolayers |
| 1987 | Dutta et al.[27] and Kjaer et al.[28] elucidated the structure of the various condensed phases found in monolayer films |
| 1995 | Kaganer and Loginov[29] elaborated on the theoretical basis of phase transitions in monolayers |

Recent interest in organic thin films has been revitalized by the discovery of new surface-active materials and development of new methods in studying the properties and dynamics of these materials. There has also been the emergence of technologies requiring these techniques, and these are described in the latter part of this chapter.

### Interfacial Phenomenon and Thermodynamics

The boundary between two phases, a transition region of steadily varying composition and properties, has been described by Langmuir as a very thin region of no more than one to two molecules thick.[17,23] The molecules lying in this region behave differently than those in the bulk. Molecules in the bulk have forces distributed isotropically around

them; those at the interface encounter a net cohesive force that tends to draw them toward the interior. This condition is depicted in Figure 2-1 below. The cohesive force tends to minimize the surface area of the interface and is responsible for the formation of near spherical-shaped droplets as commonly observed in dispersions. This cohesive force has been originally referred to by Langmuir[30] and independently by Harkins[31,32] as the *surface tension* or *interfacial tension* of the liquid.



Figure 2-1. Forces (indicated by arrows) acting on molecules in the bulk and at the interface. Adapted from Tadros.[33]

The concept of surface tension in liquids is conveniently illustrated by a practical experiment described by Gibbs and more recently by Chattoraj and Birdi.[34]

Consider a thin liquid film (*see* Figure 2-2) confined in a wire frame with area $A = w \times l$ and being stretched by $dl$ with a force $f$. The work done by the extension corresponds to a change in surface energy $\gamma dA$. That is,

$$f dl = \gamma dA \qquad \qquad 2\text{-}1$$

or

$$\gamma = f \left( \frac{dl}{dA} \right)$$

where $dx$ is the displacement involved in the work and $dA$ is the resulting area change in

the film. The quantity $\gamma$ represents *surface tension* and has the dimensions of *force per unit length of surface*. Usually, the surface tension takes the units of dynes/cm or mN/m, which have equal numerical values. In certain instances, the unit *energy per unit area* such as joules per square meter (J/m$^2$) is also used.
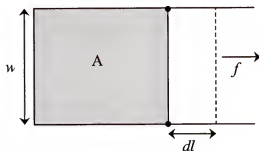


Figure 2-2. Surface film confined in a wire frame.

A full treatment of surface and interfacial thermodynamics was thoroughly investigated by Gibbs et al.[35] and Guggenheim.[36] The mathematical models adapted by Gibbs et al. and Guggenheim both consist of geometrical surfaces representing the phase boundaries of the bulk material and the vapor phase above it. What distinguishes the two approaches from each other is the presence of an interfacial region in Guggenheim's formulation that is nonexistent in the model by Gibbs et al. In essence, Guggenheim's model approaches a real system better than that adapted by Gibbs et al.

For any homogenous system at equilibrium, the internal energy is a function of the independent variables $S$, $V$ and $n$, representing entropy, volume, and molar number, respectively.

$$U = U(S,V,n) \qquad\qquad 2\text{-}2$$

$$dU = \left(\frac{\partial U}{\partial S}\right)_{V,n} dS + \left(\frac{\partial U}{\partial V}\right)_{S,n} dV + \left(\frac{\partial U}{\partial n}\right)_{S,V} dn \qquad\qquad 2\text{-}3$$

$$dU = TdS - PdV + \sum_i \mu_i dn_i \qquad\qquad 2\text{-}4$$

In Guggenheim's approach, the internal energy for the surface layer $s$ lying at the interface has a fundamental form similar to that of a homogeneous phase. The only modification is the inclusion of a $\gamma dA$ term that accounts for the work due to surface expansion. That is,

$$dU^s = TdS^s - pdV^s + \gamma dA + \sum_i \mu_i dn_i^s \; . \qquad\qquad 2\text{-}5$$

and the Gibbs function is

$$dG^s = -S^s dT + V^s dP - Ad\gamma + \sum_i \mu_i dn_i^s \qquad\qquad 2\text{-}6$$

Since the system variables $S$, $U$, $V$, and $n$ are linear sums of the contributions from each component of the system, they can be represented by the following equations

$$S^t = S^v + S^l + S^s \qquad\qquad 2\text{-}7$$

$$U^t = U^v + U^l + U^s \qquad\qquad 2\text{-}8$$

$$V^t = V^v + V^l + V^s \qquad\qquad 2\text{-}9$$

$$n^t = n^v + n^l + n^s \qquad\qquad 2\text{-}10$$

where the $t$, $v$, $l$, and $s$ represents system, vapor, liquid and surface phases. It can be shown that for a planar boundary, the value of $\gamma A$ is invariant.

If the interfacial layer has negligible thickness, i.e., $V^s = 0$ and the phase boundary is made to coincide in a single surface called the *Gibbs geometrical surface*, then the Guggenheim formulation reduces to that of Gibbs':

$$dG^s = -S^s dT - Ad\gamma + \sum_i \mu_i dn_i^s \qquad\qquad 2\text{-}11$$

The resulting Gibbs-Duhem relation,

$$S^s dT + A d\gamma + \sum_i n_i^s d\mu_i = 0 \qquad\qquad 2\text{-}12$$

gives the dependence of surface tension on the temperature and the chemical potentials of

the components. It follows that at constant temperature and composition

$$\gamma = \left(\frac{\partial G}{\partial A}\right)_{T, n_i} \qquad\qquad 2\text{-}13$$

At the interface, the quantity surface pressure $\Pi$ is defined as

$$\Pi = \gamma - \gamma_o \qquad\qquad 2\text{-}14$$

where $\gamma$ is the measured surface tension at the surface and $\gamma_o$ is the surface tension of the

pure liquid.

<u>Structure of Langmuir Films</u>

The formation of insoluble monolayers is strongly influenced by the way the

molecules pack together, their molecular weight and a suitable balance of the lipophilic-

hydrophilic properties of the molecule. A delicate balance of intermolecular repulsive and

attractive forces between the amphiphiles themselves is also important.

As has been noted by Hardy, molecules consisting of hydrophobic and hydro-

philic parts are able to form monolayers, and the hydrophilic part must be oriented to-

wards the water surface for the spreading to occur.[20,21] Adam[12] in his book outlined a

classification of different hydrophilic head groups in aliphatic compounds in terms of

their "effectiveness" in providing interaction with water. In this classification, halo-

genated compounds and pure hydrocarbons are categorized as "very weak" while alco-

hols, carboxylic acids, amines and other polar functional groups are categorized as

"strong." Highly ionizable functional groups such as quaternary amines, phosphates and

sulfates are ranked as "very strong."

General Description

   Pockels[18] was first to illustrate the effect of a small amount of oil on the surface tension of water. At very small amounts of oil, no apparent effect was observed until a certain specific amount of oil per unit area is reached, at which point the surface tension is observed to change abruptly. It was not until Langmuir in 1917 published his classic paper, "The Constitution and Fundamental Properties of Solids and Liquids," that the significance of this phenomenon was understood.[17] Langmuir described that upon spreading, the adsorbed molecules behave as a perfect gas at very large molecular areas. In this state, the free energy of the surface (i.e., surface tension) is unchanged. As the area is reduced, the film transforms into a liquid, and then to a solid as the area is further reduced. Langmuir also suggested that the solid-like phase corresponds to packed-molecules standing upright, with the hydrophilic ends being "dissolved" in the water subphase. As the compression of the amphiphile is continued, Langmuir proposed the solid phase collapses into multi-layered, three-dimensional structures.

   Figure 1-3 shows a generalized isotherm illustrating the different monolayer phases as originally suggested by Langmuir. The area in which the straight segment at high surface pressure is extrapolated to ordinate axis is denoted by $A_o$, a characteristic of the film-forming material. For most carboxylic acids and alcohols with unsaturated alkyl chains, the packing is unhindered and this area corresponds to closest packing of the molecules.
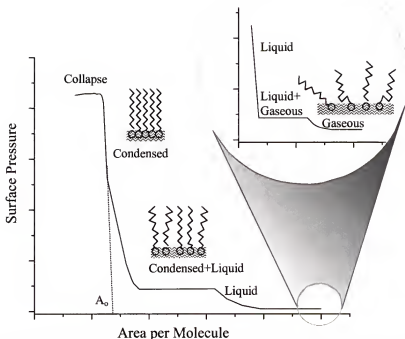
Figure 2-3. Generalized Π-$A$ isotherm of a Langmuir monolayer as proposed by Langmuir. Inset is an expanded view of the region in the isotherm where the gaseous to liquid transition occurs.

From Equations 2-11 and 2-14,

$$\left(\frac{\partial G}{\partial \Pi}\right)_{P,T} = A \qquad\qquad 2\text{-}15$$

Hence, the plateau regions correspond to a first-order phase transition according to the Ehrenfest classification,[37] showing a discontinuous change of area at constant pressure and temperature.

The existence of a "solid" phase in the isotherm was supported by Adam's [12] observation that the compressibility of the film in this region compares favorably with analogous materials in the bulk. Also analogous to materials in the bulk, Miyano et al.[38] was able to show that during stress relaxation experiments, the "solid" phase manifests an

elastic deformation and shows residual stress. The "liquid phase," on the other hand, relaxes completely, leaving no residual stress in the film regardless of its viscosity.

<u>Condensed Phases</u>

In the succeeding years, broadened discussions of the phase transitions occurring in adsorbed monolayers were introduced. Harkins[25] suggested that for the case of oleic acid and other amphiphiles in which there is no clear liquid to solid phase transition, films compressed at higher surface pressure should be described as *liquid condensed* ($L_2$) and that the corresponding film formed at lower surface pressure should be termed as *liquid expanded* ($L_1$). The driving mechanism for the first order liquid-liquid transition arises from a competition between the conformational entropy of the chains, which stabilizes the expanded phase, and a tendency to parallel alignment, which stabilizes the condensed phase. The importance of the conformational entropy for the transition had already been demonstrated by experiments of Barton et al.: if one reduces the chain flexibility by substituting for hydrogen with fluorine, the liquid expanded phase will disappear.[39]

Later, Harkins also introduced the idea of an *intermediate* (*I*) phase as a transition between $L_2$ and $L_1$.[25] Unlike the distinctive first-order *gas $\leftrightarrows$ liquid* transition, the $L_1 \leftrightarrows I$ and $I \leftrightarrows L_2$ transitions are very unclear. Harkins described that the $L_1 \leftrightarrows I$ transition resembles that for a first-order change except that the transition on the $\Pi$-$A$ diagram is not entirely abrupt and the surface pressure does not remain constant as the area is reduced. The subsequent $I \leftrightarrows L_2$ transition was described by Harkins as a possible third- or second-order. However, Gaines argued that it is a kinetic artifact and is not an equilibrium state.[40] Lifschitz argued that the intermediate phase is a metastable state since it violates

the symmetry principles of higher order transitions.[41] Following on Harkins' work, Ställ-berg-Stenhagen studied the Π-*A* isotherms of behenic acids with varying temperatures. As previously suggested by Harkins and Copeland[25] and confirmed by Ställberg-Stenhagen, a superliquid phase was found at a lower molecular area than the *L₂* phase. This phase transition is deduced from the decrease in viscosity and film rigidity in this state.[26] The phase designation was in agreement with Lundquist's later assignment for the long-chain acetates.[42] More detailed inspection of the isotherm also revealed another liquid phase, labeled as *L₂'*, at slightly lower molecular area. The more compressed monolayer state revealed the solid phases *S* and *CS*. The successive $LS \leftrightarrows S$ and $S \leftrightarrows CS$ transitions have been suggested to be second order but the corresponding $L_2 \leftrightarrows CS$ and $L_2' \leftrightarrows CS$ transitions are definitely first-order.

With the introduction of newer microscopic and spectroscopic characterization techniques, the phase behavior of Langmuir monolayers has been elucidated in more detail. In the first attempt to visualize phase transformations involving electron microscopy, the variation of surface film density was noted to correspond to changes in surface pressure[43] and that multilayer films show close-packed structures in a hexagonal lattice.[44] Teissie,[45] McConnell and coworkers,[46-48] and Lösche and coworkers[49,50] introduced the epifluorescence microscopy (EFM) technique as a means of investigating Langmuir monolayers in situ. By using a fluorescent monolayer material or the addition of a minute amount of a fluorescent probe (< 1 mole%) in the spread monolayer, the phase transition is visualized due to different solubility, orientation or density of probes in the various phases.[49] Lösche et al. pointed out several inconsistencies with von Tscharner's results to theirs and those of Albrecht et al.[51] and Cadenhead et al.[52]. One of these inconsistencies is

von Tscharner's suggestion that the liquid expanded phase $L_1$ is a two-phase region. Lösche et al. found no evidence of such inhomogeneity in this phase and suggested that the discrepancies are most probably due to different preparation technique of the monolayer.

At pressures where the monolayer starts to form a highly condensed phase, the fluorescence microscopy technique tends to be ineffective as a tool to characterize phase behavior. Aside from the fact that it is resolution-limited typical of microscopic techniques, the ability of EFM to visualize phase domains becomes limited by the diffusion and solubility in the condensed phase of the fluorescence probe. To circumvent these limitations, a new microscopic technique was developed by the groups of Möbius[53] and Meunier.[54] The new technique is based on the alteration of the Brewster angle condition (hence the name Brewster Angle Microscopy or BAM) of the air-water interface in the presence of a thin film. This resulted in the direct observation of additional phases in the condensed phase without the addition of any probe that might cause experimental artifact. For example, Overbeck and Mobius has shown the existence of a phase transition within the $L_2$ phase (later to be known as the $Ov$ phase) that was previously undetected from isotherm measurements and fluorescence microscopy.[55] Later, Lautz and coworkers developed a Brewster-angle microscopy coupled with autocorrelation technique that is capable of accurately detecting molecular tilt and orientation.[56-60]

As a complementary technique to both EFM and BAM techniques, several others have developed methods based on infrared reflection-absorption spectroscopy.[61] The observed IR frequencies, mainly the hydrocarbon $CH_2$ symmetric and antisymmetric stretching modes, for films of amphiphilic species provide information about the confor-

mational states of the hydrocarbon chains and the hydrogen bonding and ionization states of the polar head groups, under conditions of controlled surface pressure.[62] Detailed consideration of the reflection-absorption properties of the three-phase (air-monolayer-water) system can give an insight on the molecular orientation in the various phases. This technique has been exploited by the Baekmark group[63-65] to study the mushroom-to-polymer brush transformation in lipopolymers; and by Buontempo and Rice in looking at the tilting transition as the surface pressure increases.[66]

Molecular Packing

No direct and quantitative proof regarding the structure of Langmuir monolayers has been obtained experimentally until in 1987 when scattering measurements using high-intensity x-ray from a synchrotron source were done by Dutta et al.[27] and Kjaer et al.[28] They successfully obtained structural information from a monolayer at the air-water interface and showed that the monolayer does indeed form organized domains with a characteristic 2D-powder diffraction pattern. Lin et al.[67] showed that the lattice packing of the alkyl chains for a $C_{21}$ fatty acid is a distorted hexagon and that the molecules themselves undergo a tilting transition as an intermediate process towards a fully vertical state in the S phase, referred to as A' phase by Lin. At least two types of tilting have been determined: a tilt towards the nearest neighbor (NN) in the lattice or towards the next-nearest neighbor (NNN).

At the LS phase, Shih et al.[68] described phases that are analogous to the rotator phase[69] in the lamellar structure in bulk paraffins. In these phases termed Rotator I and Rotator II by Shih et al., the hydrogen atoms along the alkyl chains are thought to be frozen in a random orientation or that the entire molecule can freely rotate around its long axis. Although the analogy has been put in doubt by Sirota,[70] the existence of well de-

fined structures in these "liquid" phases is well established. It has also been established that the translational degree of freedom is the same as that in the "solid" phase. Hence, the use of the term *liquid condensed* and *solid* to describe the less compressible region of the isotherm has been discouraged, most recently by Kaganer et al.[71] As recommended by Kaganer et al., these regions should be labeled simply as *condensed*. Kaganer et al. further suggested that that the *condensed* regions of the isotherms be distinguished by simply calling them *tilted condensed* and *untilted condensed*.

Table 2-2. Monolayer condensed phases and deduced molecular tilts and lattice cell distortion. Adapted from Kaganer et al.[71]

| Harkins, Adam, Ställberg-Stenhagen, Lundquist | $L_1$ | $L_2$ |  |  | $L_2'$ |  | $LS$ | $S$ | $CS$ |
|---|---|---|---|---|---|---|---|---|---|
| Kaganer |  | $L_{2d}$ | $L_{2h}$ | $Ov$ | $L_2'$ | $L_2''$ | $LS$ | $S$ | $CS$ |
| Azimuth of tilt |  | *NN* | *NN* | *NNN* | *NNN* | *NN* | *U* | *U* | *U* |
| Azimuth of unit cell distortion (normal to chains) |  | *U* | *NNN* | *U* | *NN* | *NN* | *U* | *NN* | *NN* |

*NN* = tilt or distortion to the nearest-neighbor molecule; *NNN* = to the next-nearest neighbor; *U* = untilted or undistorted hexagonal

Table 2-2 shows the classical phase nomenclature as originally suggested by Harkins and the deduced molecular tilts of the molecules in these states. The $L_{2d}$ and $L_{2h}$ phases [29,72] are subdivisions of the well-known $L_2$ phase, distinguished only by symmetry difference: the $L_{2h}$ is a rotator phase whereas $L_{2d}$ is not and is characterized by a positional order.

Kaganer also suggested the classification of the phase transition in the condensed region into three main groups of phase transitions:

(i)     between an isotropic and anisotropic phase (e.g., $L_2' \leftrightarrows LS$, $L_2 \leftrightarrows LS$)

(ii)     between highly anisotropic tilted phase and a weakly anisotropic untilted phase (e.g., $L_2$' ⇆ $CS$, $L_2$' ⇆ $S$)

(iii)    between two anisotropic phases with approximately the same degree of anisotropy (e.g., $L_2$ ⇆ $Ov$, $S$ ⇆ $CS$).

Analogous Liquid Crystal Smectic Structures

As the structure of amphiphiles became known, an analogy with thin films of liquid crystals (LCs) was established.[73,74] Not only that they exhibit molecular ordering characteristic of LCs, but monolayers have also been shown to have optical textures similar to those in smectics.[75,76]

The smectic phase in LCs have the characteristic long-range order in which the molecules align themselves in layers (see Figure 2-4). A single layer of this structure resembles the mesophase structure in Langmuir monolayers in that they both have some positional correlation in two dimensions in addition to orientational ordering. Comparison between specific structures in monolayers and LC smectics is provided in Table 2-3.

The isotropic *liquid expanded* or $L_1$ phase is analogous to a smectic-A ($S_A$) where the centers of gravity of the molecules are ordered at random in a liquid-like fashion. In addition, they have considerable freedom of translation and of rotation around their principal axis. Schwartz et al.[77] noted that low-density, inhomogenous films in the $L_2$ and $L_2$' show diffraction patterns similar to the tilted smectic-I ($S_I$) and smectic-F ($S_F$) phases.[78] The $LS$ phase is characterized by an untilted hexatic structure which may have rotator phase properties and is similar to the hexatic LC smectic-BH ($S_{BH}$) phase.
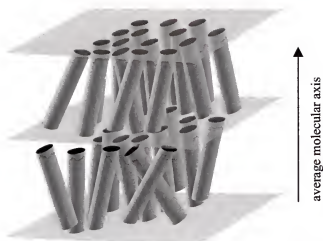
Figure 2-4. A bilayer of liquid crystal molecules represented by rigid rods in the smectic phase. The molecules have an average molecular orientation that is normal to the pseudo-surface dividing the layers. Adapted from Singh.[79]

Table 2-3. Comparison between monolayer phases and LC smectic phases [73,77]

| Monolayer phase | State | Related LC phase |
|---|---|---|
| $G$ | Gas | no equivalent |
| $L_1$ | Isotropic 2D liquid | $S_A$ |
| $L_1'$ | Mesophase | $S_L$ |
| $L_2$ | Mesophase | $S_I$ |
| $L_1'$ | Mesophase | $S_F$ |
| $L_2^*$ | Mesophase | $S_H$ |
| $L_2''$ | Undetermined | $(S_K)$ |
| $LS$ | Mesophase | $S_{BH}$ |
| $S$ | Mesophase | $S_E$ |
| $CS$ | True 2D Crystal | no equivalent |

The phase transition in docosaoic acid has been investigated and the resulting phase diagram is shown in Figure 2-5 below.[80] Direct comparison with LC smectic phases have been made based on x-ray studies.
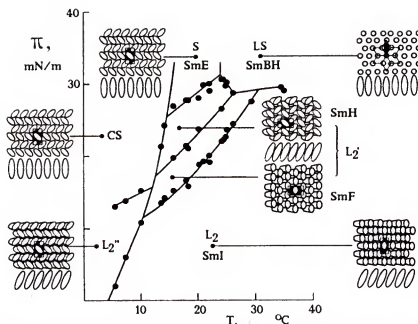
Figure 2-5. Direct comparison of docosanoic monolayer phases and liquid crystalline smectic phases. The figure also shows the local structure of the monolayer, viewed from the top and the side, as deduced from x-ray studies. From Peterson.[80]

Dependence on Environmental Effects and Molecular Structure of Phase Diagrams

The Principle of Corresponding States

Devaux initially showed that the phase transitions observed during compression and decompression can also be induced by changing the temperature.[22] Similar to 3-dimensional materials, condensed and crystalline phases were observed at high pressures and low temperature while low-density phases are observed at low pressures and high temperature. Later, Ställberg-Stenhagen and Stenhagen found that the temperatures at which the various transitions occur are raised by about 5°C for each added CH$_2$ group.[26] Bibo and Peterson confirmed this observation in their studies of homologous series of aliphatic acids.[81] Peterson later introduced the principle of corresponding states to account for the identical molecular packings in different monolayer materials, albeit at different surface pressures and temperature.[80] This idea was originally discussed in the con-

text of the relevance of monolayer phase behavior to the structure of phopholipid bilayers found in cell membranes.[51,82]

In the work done by Bibo and Peterson, the $C_{14}$-$C_{22}$ homologous fatty acid series was investigated. To match the triple points into correspondence, the temperature axis was offset by an amount depending on the chain length, Figure 2-6 shows the phase diagrams of the materials investigated. The variation in their triple points was found to be about 6-10°C for every methylene group. Similar results were also observed in the case of acetates[83] and acrylamides.[84] In effect, the addition of $CH_2$ units is comparable to lowering the temperature of the system, or similarly, causing the increase in the temperature at which phase transitions occur.[81,85] Later, Peterson et al. attempted to quantitatively describe the principle of corresponding states in terms of the free-energy of the system consisting of monolayers with the same head groups, kept at the same environmental conditions (i.e, same temperature and subphase), and have the same local packing parameters (i.e., tilt and lattice spacing).[86] The linear scaling of the phase transitions temperatures is attributed to the fact that internal energy per molecule scales linearly with the chain length and that the change in entropy during the transition is approximately chain independent.[87]

In the case of fatty acids and most amphiphiles with ionizable headgroups, numerical simulations done by Polimeno et al. using coarse-grained models (i.e., each methylene group in an alkyl chain is represented by a single atom and connected by a spring to the next unit) pointed out that the extent of *LE* and *LC* regions are determined by attractive interactions between the chains and the repulsive interactions between the headgroups.[88]

Alkyl Chain Structure

The presence of "kinks" in the side chain caused by unsaturated double or triple bonds also changes the characteristics of the phase diagrams. Essentially, unsaturated bonds restrict the flexibility of the alkyl chain and disrupt ordering. In galactosylceramides, the introduction of acyl chains that are short and saturated or that are long but contain two *cis* double bonds causes the monolayer to display only *LE* behavior instead of the *LE* to *LC* transition seen in the saturated analogs.[89]
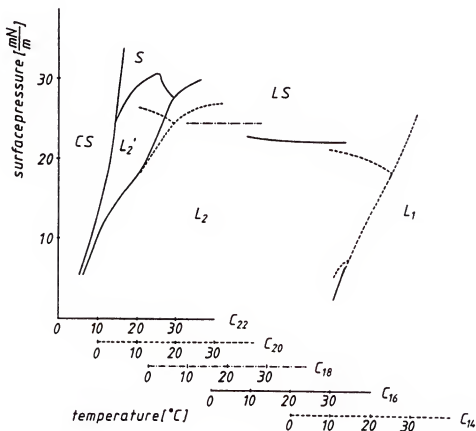


Figure 2-6. Corresponding states in the $C_{14}$-$C_{16}$ fatty acid homologous series. The temperature scale has been displaced to roughly match the triple-points. From Bibo and Peterson[81]

The effect of the nature of the side chains to the phase behavior can be directly related to its stiffness. Schmid and coworkers noted that for flexible chains, conformational entropy stabilizes the tilted phase and that it favors phases at lowed surface coverage.[90,91] For very stiff chains approaching rigid rods, the increase in the alkyl chain rigidity gives rise to a single transition from the gaseous to the condensed phase. Schmid distinguished different regimes of side chain stiffness and what kind of phase behavior can be expected from them.[92]

Table 2-4. Chain stiffness and predicted behavior. Adapted from Schmid.[92]

| Degree of Stiffness | Behavior |
| --- | --- |
| Very stiff chains (rigid rod) | single 1$^{st}$ order phase transition: gas $\leftrightarrows$ untilted $LC$ phase. |
| Stiff chains (short chain) | gas $\leftrightarrows$ $LE$ followed by $LE \leftrightarrows LC$ |
| Intermediate stiffness | tilted phase can be stable; $LE$ can co-exist with tilted and untilted $LC$ |
| Flexible chains (long chains) | $LE$ coexists with tilted $LC$ phase; tilted $\rightarrow$ untilted transition upon compression |

Multiple Side Chains and Chain Branching

Several biologically relevant molecules having multiple alkyl chains such as phospholipids and glycerides are routinely studied as Langmuir monolayers. A typical phospholipid has two long-chain fatty ester groups connected to a single zwitterionic headgroup. Glycerides on the other hand, are esters of fatty acids with glycerol and can be mono-, di-, or tri-esterified. In addition, the fatty acid in monoglycerides and diglycerides can be attached to the terminal (1-monoglycerides) or to the middle carbon (2-glycerides).

(a) phospholipid        (b) diglyceride
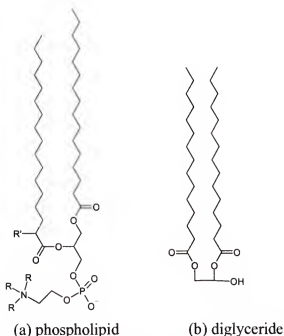
Figure 2-7. Structures of typical phospholipids and glycerides.

The presence of multiple tailgroups in these molecules restricts both rotational and translational degrees of freedom and the position of the headgroup can add to the complexity of the ordering. Figure 2-8(a-c) shows all the possible arrangement in ordered domains consisting of molecules that have two tailgroups. In the case of a phospholipid which has identical tailgroups, three tail-head positional and orientational arrangements are possible: (a) disorder in both tail and head positions and orientations; (b) the molecular centers are disordered but the molecules are orientated in a general direction; and (c) complete positional and orientational ordering.[71]

(a)                          (b)                          (c)
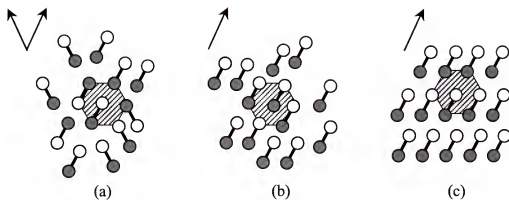
Figure 2-8. Ordering of tailgroups and headgroups in molecules with two tailgroups. The circles indicate the tails and are identified by the different shading. The hexagonal area shows the lattice packing; the arrows indicate the mean orientational ordering. Adapted from Kaganer et al.[71]

The addition of branching (usually positioned as R' in Figure 2-7a) imposes additional disruption on the ordering of the alkyl chain. Systematic studies of a series of branched chain phospholipids showed that as the branching gets bigger, from a methyl to a hexadecyl group, the molecular cross-sectional area increased from approximately 50 Å$^2$ to 60 Å$^2$.[93] The latter represents the approximate cross-section area equivalent to three alkyl chains. Isotherm measurements revealed that the degree of disruption varies in direct relation to the length of the side chain. However, as the length of the branching approaches that of the main side chain, the disruption is lessened and an ordered lattice is observed in grazing incidence x-ray diffraction.[93] The packing of branched phospholipid has also been found to be determined by the area requirement of the side chain. In the case of straight-chain phospholipids, the size of the large head group is compensated for in the lattice by the tilting of the alkyl chains.[94]

Langmuir Monolayers of Polymeric Materials

The behavior of polymers at the air-water interface is far more complex than that of any molecules discussed earlier. Due to the high conformational entropy in the polymer chain, these materials do not have sharp phase transition and their isotherms are usually featureless. In addition, the significance of mean molecular area measured from isotherms often cannot be straightforwardly attributed to some molecular length scale, unlike in the case of small molecules. Qualitative assignment of phases has been attempted[95,96] based on the slope of the curve in the isotherm. Similar to earlier description of isotherms of small-molecules, the low-coverage, lesser slope region was described as "expanded"; and the high-coverage, steep region as "condensed." Fowkes suggested that the condensed region can also have ordered structures similar to that in small amphiphiles.[97]
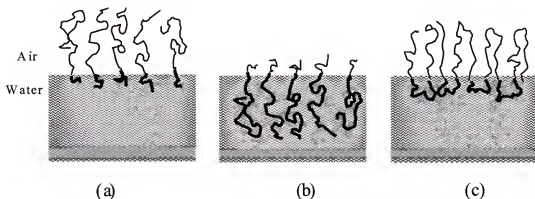


Figure 2-9. Conformation of polymers at the air-water interface. Thin and thick lines indicate the hydrophobic and hydrophilic moeties, respectively.

A telechelic polymer, or a short block copolymer where one segment differing in hydrophobic character can be regarded as an amphiphilic molecule. At the air-water interface, they can either be in a non-solvated state (Figure 2-9a) or in a solvated state (Fig-

ure 2-9b) depending on how the chains interact with the subphase.[98] In the first case, there is a strong interaction between individual chains and there is a finite concentration of segments approaching bulk density. In the other case, the chains are highly interacting with the subphase and so the concentration can be variable.[98]

The conformation and structure of polymer chains tethered at the air-water interface have also been investigated in more detail. A theoretical description describing the variation in the surface pressure with the chain length has been developed. If the chains assume Gaussian statistics, the surface pressure was predicted to vary with the chain length to the third power at a given area per head group ($A/n$). In the case of non-Gaussian statistics, the slope can be expressed as a polynomial of ($A/n$). Experimental data obtained from polyisoprene monolayers confirmed the theoretical predictions.[99]

Penetration of certain parts of the polymeric chain into the subphase (see Figure 2-9c) becomes important for linear polymers such as poly(ethylene oxide) (PEO) and polystyrene (PS)-PEO copolymer.[100-102]

There have been reports of polymers forming self-assembled structures at the air-water interface. Diblocks of polystyrene-poly(n-butyl methacrylate) and polystyrene-poly(t- butylmethacrylate) were observed to form surface micelles with starfish, rod and planar morphologies.[103] Monolayers of a polystyrene/poly-4-vinylpyridine AB diblock ionomers, quaternized with decyl iodide have been shown to form circular surface micelles. The distance between the micelles (measured from Langmuire-Blodgett films transferred at low surface pressures) is consistent with fully extended decylated PVP, extending radially from a central core of PS coils.[104]

Dendrimers based on poly(propylene imine) has also been observed to form cylindrical shaped self-assembled structures. In this configuration, all the chains are aligned perpendicular to the water surface, and the dendritic poly(propylene imine) core faces the aqueous phase.[105]

## Applications of Langmuir and Langmuir-Blodgett Films

The primary application of Langmuir films has been the preparation of materials for subsequent deposition on substrates, either as plain Langmuir-Blodgett (LB) films or variations.[14] Langmuir-Blodgett films have found a number of applications and Langmuir and Blodgett themselves have acquired several patents for these materials. These include the use of LB films in image reproduction, as optical devices, as step gauges, and as ultrafine filters.[14] Both Roberts[14] and Ullman[15] provide an extensive discussion on this topic.

The ability of monolayer films to modify interfacial properties has been found to be important in several industrial processes. For example, one critical aspect in the production of liquid-crystal displays is the alignment of the liquid crystal molecules on a substrate. Treating the surface with lecithin[106] or alkylsiloxane[107] provides the necessary physico-chemical interaction between the substrate and the liquid crystal.

As adsorbed monolayers at the liquid-vapor interface, Langmuir films also have their own relevant applications. Studying monolayers at the air-water interface provides ease of control of several important parameters including molecular conformation and surface concentrations. In addition, a number of theoretical concepts can be directly tested experimentally by virtue of the unique geometrical environment that monolayers provide. The following section discusses some of the more recent interests in Langmuir and Langmuir-Blodgett films.

Molecular Electronics and Microdevices

As technology advances, devices have become smaller and smaller so much so that current technology has approached control down to molecular level.[108] Langmuir-Blodgett technique, along with spin coating, solution casting and micro-printing, has been used to prepare field-effect transistors from poly(3-alkylthiophene).[109,110]

Langmuir-Blodgett films have also been used as photoresists. Barraud, et al.[111-113] have obtained negative fine resist patterns with 60 nm resolution using electron beam polymerization of ω-tricosenoic acid (TA). Lando, et al.[114] used α-octadecyl acrylate multilayers both as positive and negative electron resist with 80 nm and 50 nm resolution, respectively.

Another area where LB technology has received recognition is in the field of microelectromechanical (MEMs) devices.[115] It is known that the presence of Langmuir-Blodgett films can change the tribological properties of the surface on the nanoscale.[15,116] This attribute of monolayers has been exploited for their use as molecular lubricants and glues in the fabrication of microdevices. The use of polymeric and dendritic supramolecular films have received special attention because of their mechanical robustness.[115]

Langmuir and Langmuir-Blodgett Films as Model Systems

Monolayers at the air-water interface are interesting because the interface is structurally well-defined. This was the basis for several studies of hydrophobic non glassy polymers with ionic head groups as model systems to investigate thermodynamics of "polymer melt brushes."[98,99] Polymers at the air-water interface can be thought as being similar to a chain tethered to the planar surface, and are free to assume a distorted 3-dimensional conformation. The adaptation of this model system made it possible to give

the polymer brushes a well-defined orientation and made them accessible to experimental techniques not available in the bulk.[98]

Other applications of Langmuir films as model systems were inspired from the original work pursued by Kuhn and coworkers.[117,118] Langmuir-Blodgett technique provided a method for Kuhn and coworkers to prepare well-defined layers of molecules in which they were able to measure intermolecular interactions involved in photophysical processes.

Charych and coworkers described the fabrication of an artificial membrane from LB films of polydiacetylenic lipid. Their results pointed to a possible molecular recognition at the surface of a membrane and that a concentration of 20 ppm of the analyte protein could be detected using the polymerized thin films.[119]

Intermolecular interactions of biologically important molecules have also been probed using Langmuir monolayer techniques. The penetration of the drugs chlorcyclizine and ampicillin into phospholipids have been assessed by simple surface pressure and surface potential measurements.[120]

## Summary

Amphiphilic molecules with a sufficient balance of hydrophobic and hydrophilic character can adsorb at the air-water interface and form monomolecular-thick films. These monolayer films can exhibit behavior very similar to that found in bulk materials. Using modern analytical tools, several interesting phases have been found, especially in the condensed phase of the films. These monolayer states are summarized in Table 2-5.

Table 2-5. States of monolayers. Adapted from Gaines[10] and Kaganer et al.[71] Nomenclature follows the Harkins-Stenhagen notation of phases.[26,121,122]

| | Increasing Density → | | | | | | | | | | |
|---|---|---|---|---|---|---|---|---|---|---|---|
| Devaux, Langmuir | $G$ | $L$ | | | | | | | | $S$ | |
| Harkins, Adam, Ställberg-Stenhagen | $G$ | $L_1$ | $I$ | $L_2$ | | | | | $LS$ | $S$ | $CS$ |
| Dervichian | | | | | | | *mesomorphous* | | | | |
| Lundquist | | $L_1$ | | $L_2$ | | | $L_2'$ | | $LS$ | $S$ | $CS$ |
| Lin, Shih | | | | $D$ | | | $C$ | $B$ | $RI$-$RII$ | $A'$ | $A$ |
| Bibo, Knobler and Peterson | | | | $L_2/L_1'$ | | | $S'/L_2^{\bullet}$ | $L_2''$ | $LS$ | $S$ | $CS$ |
| Overbeck and Möbius, Durbin, Reviére | | | | $L_2$ | | $Ov$ | $L_2'$ | $L_2''$ | $LS$ | $S$ | $CS$ |
| Durbin | | | | $L_2$ | | | $I$-$L_2'$ | | $LS$ | $S$ | |
| Kaganer and Loginov | | | | $L_{2d}$ | $L_{2h}$ | $Ov$ | $L_2'$ | $L_2''$ | $LS$ | $S$ | $CS$ |

Note: $G$ gaseous; $L$ liquid; $S$ solid; $L_1$ liquid expanded; $I$ intermediate; $L_2$ liquid condensed; $LS$ super liquid; $RI$-$RII$ rotator phases

Insight into the behavior of monolayers at the interface will contribute to a better understanding of a variety of systems that are fundamentally similar to monolayer films.

## CHAPTER 3
## GENERAL EXPERIMENTAL TECHNIQUES

The study of monolayer materials is still fraught with challenges notwithstanding the fact that this scientific area has been active for much of the 20th century. The problems arise principally due to the limited quantity of materials at hand and the lack of available techniques that can be utilized, not to mention that most of the time the sample has to be analyzed *in situ* at a liquid interface to get results that are relevant to the system being studied. Most techniques that have been used to characterize these materials have limitations that are usually associated with low instrumental signal-to-noise ratio and high statistical sampling errors. The former have undergone tremendous improvement over the years with the development of modern microelectronics and the improvement of a diverse number of analytical tools. Unfortunately, the problem related to statistical sampling cannot be resolved too easily except through careful experimentation. Better understanding of the results can be attained by confirming them with complementary techniques, including corroboration with theoretical methods.[15]

Standard chemical analytical techniques such as uv-vis and infrared spectroscopies have been successfully modified to characterize amphiphiles both *in situ* at the air-water interface and as LB films. Several techniques have been developed specific for the study of Langmuir films. These include Brewster angle microscopy and several rheological measurement techniques for 2-dimensional fluids. Elucidation of the structure and phases of monolayers had remained qualitative and macroscopic until the introduction of synchrotron techniques by the groups of Dutta et al.[27] and Kjaer et al.[28] These and

other recent developments such as the scanning probe techniques have ushered a new era in the study of Langmuir and Langmuir-Blodgett films. Dynarowicz-Latka et al. covers most of these advances in a recently published review article.[9]

In this chapter, an overview of both classical and modern methods of physico-chemical characterization of monolayers and related materials will be discussed. Emphasis will be given on techniques and methodologies that were principally used in this study. These include the basic thermodynamics and kinetics measurements and several techniques related to morphological and structural analysis.

## The Langmuir Trough Setup

The Langmuir trough is the basis of all studies of Langmuir monolayers and the main equipment used for the preparation of Langmuir-Blodgett films. Of course, the original trough system was not called a *Langmuir trough* and it did not feature the kind of automation found in most modern trough systems. In fact the very first "trough" was designed by Pockels out of a rectangular tin can she found in her kitchen![18]

In a typical trough system (see Figure 3-1), four components are essential to perform an experiment: (a) a container (or trough) to hold the liquid subphase; (b) a barrier used to limit the area of confinement of the monolayer; (c) a surface balance to measure the surface tension or surface pressure; and the (d) control electronics. Optional components may include a dipper to hold the substrate during the preparation of LB films and a system to control the temperature in the trough.

## Troughs and Barriers

The trough is usually constructed out of inert materials and needs to be mechanically rigid or can be mounted on a rigid support. It is designed to hold a large volume of liquid and have a large area of the liquid exposed for manipulation. The typical surface

geometry is rectangular with depths that can range from 1-10 cm and can contain volumes anywhere from 200 mL to several liters. Other trough geometries such as circular[123-125] and constant perimeter barrier[126] have also been designed.

Another requirement which is of utmost practical importance is that the trough and barriers have to be easy to clean and simple to operate. To obtain high stability and precision in the measurement, the whole trough assembly is usually mounted on top of a vibration isolation table or a heavy granite slab.
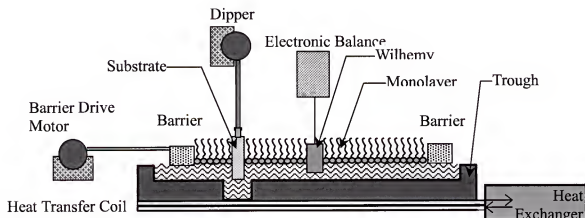


Figure 3-1. Basic components of a modern Langmuir trough system which include a dipper control to transfer films to a solid substrate.

The edge of the trough where the barriers rest has to be smooth so that the frictional force between the trough and the barrier is minimized. It is also important that the trough edge is non-wettable so that the subphase liquid forms a nice meniscus on the edges and does not spill out.

Most modern trough systems are constructed out of plastic materials such as polytetrafluoroethylene (PTFE) or nylon. PTFE has an advantage of being hydrophobic and oleophobic making it possible to use both aqueous- and organic-based subphases.

Being hydrophobic also eliminates the need to apply coatings such as ferric stearate,[127] and paraffin wax,[10] avoiding possible contamination that might result from leachates. Moreover, PTFE, unlike nylon, is chemically resistant and stable over a wide range of pH.

An additional feature of a Langmuir trough is a well, where a substrate can be lowered and coated with the monolayer materials to obtain a Langmuir-Blodgett film. There can also be a provision for temperature regulation via heat exchange coils located underneath the Teflon trough.

The materials used for barriers are similar to those used in the construction of troughs. Similar restrictions also exist with regards to chemical stability and mechanical rigidity.

Surface Balance

One of the most fundamental quantities measured from a monolayer is its surface pressure $\Pi$, which is related to surface tension by

$$\Pi = \gamma - \gamma_o \qquad\qquad 3\text{-}1$$

In Pockels' work, the surface tension was measured as the amount of force necessary to lift a small disk off the water surface.[18] Current systems work from the same principles but use fundamentally different techniques.

There are at least two best-known techniques that have been commonly adapted for continuous monitoring of surface pressure. One of these systems was originally designed by Langmuir himself and uses a differential technique.[17] The other is based on an absolute technique developed by Wilhelmy[128] and exploited extensibly by Dervichian[129,130] and by Harkins and Anderson.[131]

Langmuir balance

Langmuir balance (see Figure 3-2) works by measuring the force acting on a piece of waxed paper (*B*) that separates the area containing the monolayer (between *A* and *D*) to the clean water surface (*H*). The float is coupled via two rods (*R* and *R'*) to a conventional balance (assembly consists of *S*, *K*, *G*, *K'*, and *P*) that measures the force directly. One inherent problem in this design is that the float is made narrower than the width of the trough to allow the float to easily slide thru. As a result, monolayer has a chance to leak out between the gaps especially at high surface pressures. The initial solution used by Langmuir was to blow air jets between the gaps. This presents a significant experimental problem since it disturbs the float. In recent designs, the gap is blocked with the use of thin flexible PTFE ribbon as introduced by Adam and Jessop.[132]
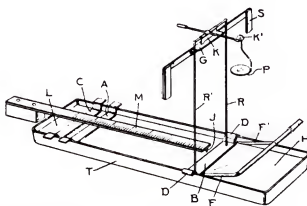


Figure 3-2. The original design of Langmuir balance.[17]

The force transduction mechanism in Langmuir balances has also been modified. Instead of a mechanical balance, the typical approach uses a linear variable differential transformer (LVDT) which provides very sensitive displacement measurement in the order of 10 μm.[133] Designs involving optical lever mechanism have also been explored resulting in the development of a novel system for low surface pressure measurements.[134]

Wilhelmy technique

   The method introduced by Wilhelmy,[128] subsequently developed by Dervichian[129] and Harkins, [131] has been widely adopted thus far. It involves the use of a wettable thin plate that is partially submerged in the subphase and suspended on a balance. The force acting on the plate is defined by the surface tension of the liquid, the gravitational pull and the buoyant effect due to the displaced liquid. The net force $F$ acting on a thin plate with dimensions shown in Figure 3-3 is expressed by

$$F = \rho_p glwt + 2\gamma(t+w)\cos\theta - \rho_l gtwh \qquad 3\text{-}2$$

where $\rho_p$ and $\rho_l$ are the densities of the thin plate material and of the liquid, respectively; $g$ is the gravitational constant; and $\gamma$ is the surface tension of the liquid. The angle $\theta$ is the contact angle made by the liquid to the surface of the plate, which is generally 0° for a completely wetted surface.



(a)                          (b)
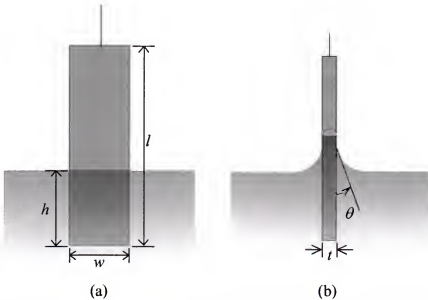
Figure 3-3. A diagram of a Wilhemy plate immersed in a water subphase. (a) front view, (b) side view

There are two methods of performing surface pressure measurements using the Wilhelmy technique: either (a) by measuring the change in $F$ for a stationary plate; or b) measuring the change in $h$ for a constant applied force. In the former case, Equation 3-2 reduces to

$$\Delta F = 2\Delta\gamma(t + w) \qquad\qquad 3\text{-}3$$

or

$$\Pi = -\Delta\gamma = -\frac{\Delta F}{2(t + w)} \qquad\qquad 3\text{-}4$$

where $\Pi$ is defined by Equation 3-1.

In the other case where the force is constant,

$$\Pi = -\Delta\gamma = -\frac{\rho_l g t w}{2(t + w)}\Delta h \qquad\qquad 3\text{-}5$$

If the plate is thin enough so that $t$ is negligibly small compared to $w$,

$$\Pi = -\frac{\rho_l g t}{2}\Delta h, \text{ if } t << w \qquad\qquad 3\text{-}6$$

The values of $\rho_l$, $g$, and $t$ are usually evaluated during the calibration procedure thus only the vertical displacement of the Wilhelmy plate needs to be measured to get the value of the surface pressure.

Miscellaneous methods of measuring surface pressure

Reports were made in reference to the use of "piston oils" or indicator oils as relative surface pressure indicators. Langmuir and coworkers,[127] in particular, made extensive use of piston oils. The have also been used to investigate the phase behavior of amphiphilic alcohols.[135-137] Piston oils are materials that spread quickly and reversibly, attaining a fixed surface pressure almost instantaneously. They are added at the surface,

separated from the rest of the film being investigated by a movable boundary. The boundary usually consists of silk thread or any thin and flexible partition.

Indicator oils, on the other hand, are used by observing the interference pattern produced from a tiny droplet place on the water surface. The extent of spreading of the tiny droplet of indicator oil is dependent on the surface tension. Upon addition of a monolayer material and with compression, its thickness will vary correspondingly resulting in the appearance of interference color that changes with the pressure.[10]

Recently, a new design for measuring surface pressure has been introduced and a diagram of such design is shown in Figure 3-4 below. The design was intended to provide a local probe (< 250 µm) of film inhomogeneity which is crucial in the development of optical and molecular devices prepared from Langmuir-Blodgett films.
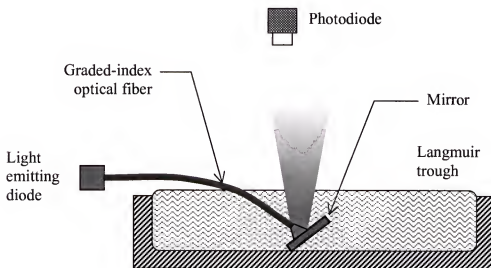


Figure 3-4. Schematic of an optical-fiber sensor for surface pressure measurement. Adapted from Zhu.[138]

A graded-index optical fiber is bent obliquely and introduced into the subphase. When the monolayer is compressed, surface tension upon the end of the optical fiber will

decrease and consequently, the bending state of the optical fiber will thus change.[138] The bending state is measured from the displacement of the light reflected off the mirror under the trough. The signal coming from a fixed photodiode positioned on top of the trough and opposite to the mirror provides a convenient measure of the displacement. By treating the optical fiber as an elastic cantilever beam, the surface tension can be derived.[138]

Control Systems and Electronics

Modern setups of Langmuir troughs use microprocessors, are programmable and equipped for digital data acquisition for automated operation.[133,139] The degree of automation can range from very simple, to one where surface cleaning and sample addition is controlled.[140] Figure 3-5 shows a general configuration of a Langmuir trough system linked to a PC via RS-232 communication protocol. The PC runs dedicated software that provides convenient means of controlling the devices attached to the system. Including the surface balance, other devices may include:

1. *display devices* to show current system status such as surface pressure, current dipping arm position, etc;

2. *deposition system* to facilitate dipping of substrate during Langmuir-Blodgett film preparation;

3. *positioning elevator* that control both vertical and horizontal positions of the balance or the dipping arm.

4. the *barrier driving system* consisting of DC motor and related components to control the movement of the barrier.

5. *manual control system* to allow control of the barriers, deposition arm and elevators without software control; and

6. optional *analog-to-digital (A/D)* and *digital-to-analog (D/A)* converters for custom application such as temperature control.
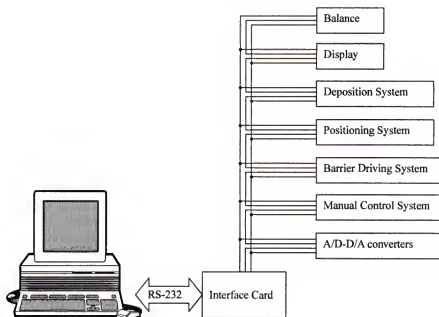
Figure 3-5. General configuration of a Langmuir trough system. Adapted from the LB5000 manual by KSV Instruments Ltd.[141]

All these individual devices are connected to a common data bus in the interface card that, in turn, is connected to the serial port of the PC. Feedback loops between devices allow convenient and simultaneous control of several parameters in the experiment. For example, Figure 3-6 below shows a simple feedback loop that controls both the barrier speed and surface pressure. In this diagram, both the target pressure and barrier speeds are set via the software. Input voltages measured from the speed transducer (consisting of a position encoder and a timer) and the electrobalance are compared to the desired values. The differential signal originating from the comparators then drives the barrier motor either in the compression or expansion mode to compensate for the input voltages. Similar feedback loops can be set up, for instance, to maintain the level of the water in the trough during extended experiments where subphase evaporation might be substantial.
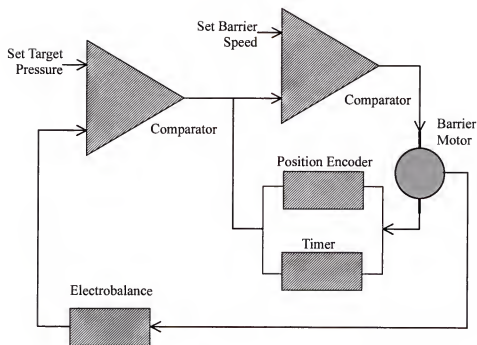
Figure 3-6. Basic feedback loop to control surface pressure and barrier speed.

The barrier motors that are used to drive the barriers are generally of DC types, which are characterized by smooth and fine movement required for Langmuir trough application. For better precision, stepping motors are used with some modification in driving circuitry to improve their resolution.[142]

### Pressure-Area Isotherm

The pressure-area ($\Pi$-$A$) isotherm is the most fundamental characteristic indicator of monolayer properties. It provides direct information on the monolayer purity, molecular area, intermolecular interaction, conformation, compressibility, collapse behavior, chemical reaction, crystallization and the thermodynamics of mixing.

General Technique

The usual approach in conducting a pressure-area isotherm is to spread a known amount of material unto the surface then vary the area by moving the barriers. The mate-

rial of interest is dissolved in a volatile solvent such as chloroform or methylene chloride. Once the solvent has evaporated, the material is left floating at the surface and compression can be initiated by reducing the area between the barriers. The mean molecular area (shown in the equation as $A_M$ but commonly known as MMA) that is shown in a typical $\Pi$-$A$ curve is calculated from

$$A_M = \frac{A \cdot M_w}{c \cdot V \cdot N_A} \qquad\qquad 3\text{-}7$$

where $A$ is the area of the trough; $M_w$ is the molecular weight of the materials; $c$ is its concentration in the spread solution in units of mg/mL or other similar units; $V$ is the volume; and $N_A$ is the Avogadro's constant.

Spreading Solvent

The selection of the solvent is very important. The main requirement is that it has to be highly volatile and that that the solvent must have very limited solubility in water to avoid dissolution of the material into the aqueous subphase.[143] Of course, for amphiphiles with short alkyl chains (12 carbon atoms or less) dissolution is a paramount problem regardless of what solvent is used.[144]

It is also important that the solvent is suitable for the material and that it does not react or complex with the monolayer material. This is especially a concern for macromolecules containing large polar groups. Collins and coworkers studied the effect of spreading solvents on the monolayer properties of poly(methyl methacrylate) (PMMA). The association of a polar solvent with the polymer causes local structural changes in the ester backbone, and this was manifested by the variations in the isotherms obtained from different spreading solvents.[145]

In certain cases, the use of a mixed solvent system is necessary. The addition of a mere 25 parts per million of n-pentanol, or n-hexanol, to chloroform as the spreading solvent was shown to improve the spreading behavior of certain organometallic nickel complexes as monolayers.[146] For highly insoluble materials, Hasegawa et al. suggested dispersing the molecules in the water surface by evaporation. As a demonstration, unsubstituted quinacridone LB films have been prepared using this method.[147]

Sources of Errors in Isotherm Experiments

There are several areas in which possible errors can arise in $\Pi$-$A$ measurements. The most obvious sources of error are inaccuracies in the measurements of the trough area and uncertainty in the concentration and volume of the solution that is spread.

One aspect that is not given much importance, but is non-negligible in certain cases is the error in trough area measurements due to surface curvature and Wilhelmy plate effect. Welzel and coworkers investigated these possible sources of errors and confirmed that theses effects are only significant for small troughs. Welzel et al. showed that for a small trough area of 22 cm$^2$, the area increment could be as high as 7% and 26% for errors due to meniscus curvature and Wilhelmy plate, respectively.[148] This is in agreement with the earlier estimates made by Gaines[10].

The increase in area due to meniscus curvature can be calculated[149] as

$$\Delta A_m = 2(l + w)\left[ a - \left(a^2 - y_o^2\right)^{1/2}\right] \text{ with } a = 2\left(\frac{\gamma}{\Delta\rho g}\right)^{1/2} \qquad 3\text{-}8$$

where $l$ and $w$ are the length and width of the trough. In addition to geometrical factors, the extension in the area is also dependent on the surface tension $\gamma$, the difference in the density between the gas and the condensed phase $\Delta\rho$, the gravitational acceleration $g$,

and the height meniscus edge $y_o$, measured with respect to the free liquid level away from the trough edge.

With the use of large troughs, both of the abovementioned sources of errors can easily be corrected and considered insignificant.[148]

There has also been concern about surface pressure gradient brought about by the lack of fluidity in the monolayer. This is especially important in polymeric films.[150] and becomes a real problem in the preparation of oriented LB films.[151] Usually, when a monolayer is compressed in a conventional trough, a pressure gradient occurs as the section of the film close to the edge moves slower relative to the section in the middle. In addition, the forward motion of the barriers induces a compression gradient near the edge of the moving barrier. Consequently, surface pressure measurement is dependent on where the Wilhelmy plate is positioned relative to the barriers in the trough and how it is oriented relative to the direction of compression. Malcolm resolved this problem by constructing a trough where compression at a uniform shear can be done.[152] In most instances, this problem is neglected and can be assumed part of experimental error of indeterminate uncertainty.

<u>Surface Film Rheology</u>

The rheological characteristics of a Langmuir monolayer describe its resistance to tangential motion. It is important in the studies of foam stability[153] and lateral interactions in protein monolayers,[154] to cite a few examples. It has been described in the literature[10,11,155,156] and Goodrich[157] provides a good analysis of the hydrodynamics involved in the various techniques.

The interpretation of measurements is usually complex and in most cases not well defined.[10] Hühnerfuss suggested that viscosity measurements are only meaningful for the

particular technique that was used, and any reported surface viscosity value has to include the description of the status of the systems, i.e., whether the value refers to the dynamic part of the measurement or to the equilibrium part, the spreading solvent, canal width, surface pressure gradient, and temperature.[158]

In most cases, the methods are adaptations of techniques for three-dimensional bulk viscosity measurements. Several methods will be described here but emphasis will be on the two most common techniques.

Canal viscometry

This technique is the classic adaptation of the Ostwald viscometer for bulk liquids. The surface viscosity of a floating monolayer can be calculated analogous to the Poiseuille formula for the flow of liquids in capillary channel.[159]
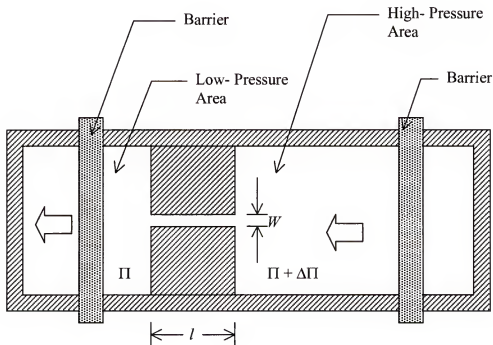


Figure 3-7. Top view of a Langmuir trough configured for canal viscometry. The block arrows indicate the direction of motion of the barriers.

Figure 3-7 shows a Langmuir trough configured for viscosity measurement. The trough is divided into two sections which are joined together by a canal with length $l$ and width $w$. Monolayer solution is spread in the high-pressure area and a constant surface pressure difference $\Delta\Pi$ is maintained between the two sections to force a constant flow of material. This is done by controlling the movement of barriers so that the pressure difference is maintained during the experiment. The surface viscosity is calculated from

$$\eta_s = \frac{\Delta\Pi w^3}{12Ql} - \frac{w\eta_o}{\pi} \qquad\qquad 3\text{-}9$$

where $Q$ is the area flow rate, $\eta_o$ is the subphase viscosity and $\pi$ takes the usual value. The second term is the correction factor that accounts for the drag due to the subphase viscosity, introduced by Harkins and Kirkwood.[160]

Goodrich pointed out that the model adapted by Harkins and Kirkwood [157] is only applicable to incompressible surface films, hence the surface pressure difference between the two sections of the trough should be as low as possible.

Damping methods

The second commonly used technique relates the damping of a body moving on the surface. There are several geometries possible for this measurement but the most popular configuration uses a Couette-type setup where a knife-edge ring rest at the interface and the dish containing the subphase is made to rotate it at a constant speed. A variation of this technique uses a double rotating ring as shown in Figure 3-8. The hydrodynamic considerations for this class of techniques have been described in detail by both Gaines[10] and Goodrich.[157]

In general, the shear viscosity is calculated from the force $F$ applied on the inner ring to keep it from moving is related to the shear viscosity by the equation

$$\eta_s = \frac{F}{2\pi r} \frac{dv_r}{dr} \qquad\qquad 3\text{-}10$$

where $2\pi r$ represents the circumference of the outer ring and $dv_r/dr$ is the velocity gradient of the interface in the gap between the rings.
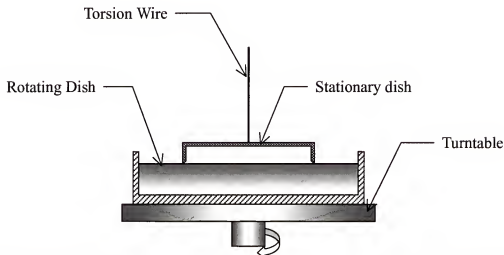


Figure 3-8. Schematic for torsion method viscometry using a Couette-type apparatus. Adapted from Davies and Rideal.[11]

The main advantage of the canal viscometer is its sensitivity. Goodrich[157] cited that a canal with width $w = 0.15$ mm the technique should be sensitive for $\eta \leq 10^{-2}$ surface poise (sP, g sec$^{-1}$). In contrast, damping methods are insensitive for $\eta_s < 10^{-3}$ sP. On the other hand, damping techniques can provide information on the surface shear modulus in addition to surface viscosity.[10]

<u>Morphology and Structure</u>

Microscopic studies of Langmuir films allowed the direct investigations of their phase behavior and the kinetics of phase transformations.[75] The original epifluorescence technique[49,50] has now been superseded by Brewster angle microscopy (BAM).[53,54] The latter avoids the use of probe molecules that might otherwise show experimental artifacts.

Information obtained from BAM has proved to be of great value and stimulate an effort to reevaluate the understanding of the phase behavior in Langmuir monolayers.

Of equal importance in this area is x-ray diffraction. This technique has become complementary to optical techniques in studying morphologies and structures of Langmuir films and was responsible for elucidating the molecular packing in the different condensed phases.[27,28]

Brewster Angle Microscopy

At the Brewster angle of incidence, p-polarized light has zero reflectance. This is the angle that meets the criterion

$$\tan \alpha = \frac{n_{water}}{n_{air}} \qquad \qquad 3\text{-}11$$

where $n$ is the refractive index of the corresponding phases.
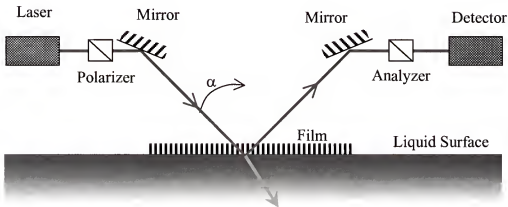


Figure 3-9. A schematic diagram of a Brewster angle microscope setup.

The basic setup is shown in Figure 3-9 and consists of a polarized laser source incident at the Brewster angle and a detector opposite to it. In the presence of a thin film at

the interface with a refractive index different from the bulk liquid, the Brewster angle criterion is modified and the laser beam is reflected. The reflection is typically detected using a charge-coupled device (CCD) camera. Subsequently, an image is captured and digitally processed.

The presence of phase separation due to difference in molecular tilts and orientation[55] or demixing in monolayer mixtures[161] are conveniently observed using this technique.

Scanning Probe Microscopy

Scanning probe microscopy (SPM) has so far proven to be one of the most useful and convenient ways of characterizing structure and morphology of transferred films down to the molecular level.

Scanning probe microscopy is a collection of techniques that include atomic force microscopy, scanning tunneling microscopy and an assortment of other related methods. Over the span of two decades since the techniques have been developed,[162-164] they have had remarkable impacts in the fields of material science, physics, chemistry, and in the biological sciences.[165] Studies in the area of polymer thin films, wear and lubrication, sensor development, biomaterials, microelectronics, and in many other areas have experienced tremendous impetus in a very short period due to the rapid progress in SPM techniques.[166,167]

The main advantage of SPM over other microscopy techniques is the ease at which measurement at an unprecedented resolution can be done at a dynamic length scale. This scale can range from sub-nanometer to micrometer scale. Moreover, a three-dimensional digital profile is obtainable, available for digital signal processing and quantitative analysis. This is one feature that even the most advanced scanning electron micro-

scope does not have. In addition, the technique is exceptionally non-destructive at the macroscopic scale.

The interest in the use of SPM to characterize thin films is both of practical and fundamental reasons. Essentially, the technique is rapid and can be operated in ambient conditions yet it can provide information that can be as fundamental as lattice order,[168] adhesion and friction at the molecular scale.[116]

Among the various SPM techniques, atomic force microscopy and scanning tunneling microscopy stand out as the most basic and important in the study of Langmuir-Blodgett films. Atomic force microscopy (AFM), in particular, is useful since the technique does not require a conducting sample, unlike scanning tunneling microscopy.

The basic AFM setup (see Figure 3-10) consists of a scanner, a probe, and the feedback electronics. The scanner usually consists of a tube mounted with several independently controllable piezo elements. By applying the appropriate polarity and voltage, the unit can move in the three Cartesian directions. The feedback electronics is designed to maintain the interaction of tip and the surface at a certain value. To do the imaging, the sample is moved under the tip by a rastering motion and the image is constructed by correlating point-by-point the output signal of the feedback loop that is necessary to maintain the setpoint.
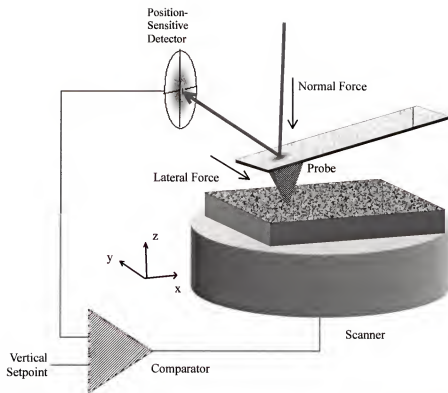
Figure 3-10. Scheme for detection of tip-surface interaction in an atomic force microscope. Adapted from the Digital Instrument SPM Manual[169]

The tip is mounted under a cantilever that provides support and means of detecting the movement of the tip. It can be made from silicon-based materials or other materials that permit microfabrication. They can also be functionalized to allow imaging of chemical and electrostatic forces on the surface.[170] Probes are available in a wide variety of sizes and spring constants. Probes having smaller spring constants are suitable in imaging soft and delicate surfaces such as Langmuir-Blodgett films. These probes are very sensitive but unfortunately prone to entrapment by surface tension and electrostatic forces on the sample surface. Stiffer probes can easily breakout from surface but they are less sensitive. For surface mechanical analysis, a stiff probe consisting of a diamond chip mounted on a stainless steel wire is used.

Tip-surface interaction is measured by detecting the position of the laser beam bouncing off the cantilever to the four quadrants of the position-sensitive detector. The

three basic tip movements that can be detected are oscillation in the z-direction, bending along the cantilever main axis, and twisting perpendicular to the same axis. These are correlated to normal, buckling, and lateral forces measured by the system, the latter being equivalent to frictional force between the tip and the sample.

X-ray Diffraction

X-ray diffraction studies have provided much of the current understanding of the structure and phases in Langmuir monolayers[71] and Langmuir-Blodgett films.[171,172]

While the classical x-ray diffraction technique is suitable to analyze the inter-lamellar structures and molecular packing in transferred films, it is not appropriate for Langmuir monolayers at the air-water interface. The main shortcoming is the low radiation intensity available in the conventional systems. The experiment time would run into long hours which is expectedly impractical and experimentally challenging. The technique essentially had to wait until synchrotron sources were developed in the early 1980s.

Synchrotron source

Conventional sources of X-ray radiation[173] such as filament tube and the rotating anode types provide inadequate intensities for the study of surfaces. Various other techniques have been used to study surface structures but technical problems limit their applications.[174] The introduction of grazing incidence x-ray scattering technique using high-brightness x-ray synchrotron in 1979[175] and the subsequent demonstration of its surface sensitivity in 1984,[176] ushered a new era in surface science. Introduction to the theory and applications of synchrotron radiation (SR) can be found in several books, like that of Koch[177] and review article.[178]

The energy spectrum produced in a synchrotron facility can range from the infra-red band up to the hard x-ray region of several hundreds keV.[177] In addition, the intensi-

ties of SR are the highest known to the scientific field. Figure 3-11 below shows a comparison of several synchrotron facilities and the spectral intensities of the radiation they are capable of producing. Note that in comparison to conventional sources, synchrotron radiation is at least two orders of magnitude more intense.
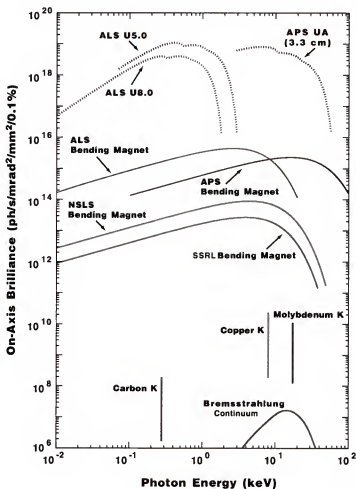


10.97

Figure 3-11. Spectral intensity of various x-ray sources. Courtesy of the Advanced Photon Source, Argonne National Laboratory. (ALS =Advanced Light Source; Lawrence Berkeley National Labs; NSLS= National Synchrotron Light Source, Brookhaven National Laboratory; APS = Advanced Photon Source, Argonne National Laboratory; SSRL=Stanford Synchrotron Radiation Laboratory, Stanford University)
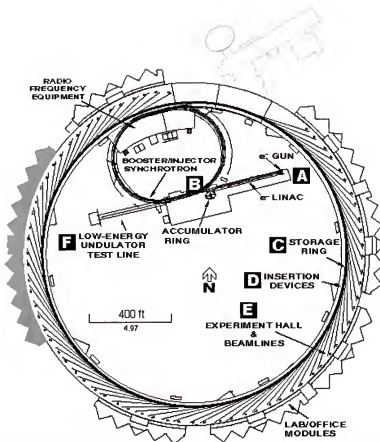
Figure 3-12. Layout of the APS facility. Particles are produced by an electron gun (**A**) in the linear accelerator. It is then transported towards the booster ring (**B**), then injected to the storage ring (**C**) where undulators and bending magnets inserted and produce x-ray emissions tangential to the ring. Courtesy of the Advanced Photon Source, Argonne National Laboratory.

Synchrotron radiation originates from the electromagnetic wave emitted by highly-relativistic ($E \gg m_o c^2$) particles moving around a circular path. At the Advanced Photon Source (APS) in Argonne National Laboratory, Chicago, IL, the circular path  (or "storage ring") is about 1104 m in circumference (see Figure 3-12). It is configured as a set of curves connected by straight sections. In each of these straight sections, an insertion device (ID) made of north-south permanent magnets with alternating polarity is inserted. X-ray emission results as the particles pass trough these alternating fields and their trajectories or speeds are altered.

Figure 3-13 shows the basic configuration of an insertion device. Depending on the strength and periodicity of the alternating magnetic fields, the particles can either wiggle (in high magnetic field, long periods) or undulate (in low magnetic field, short periods). The characteristics of the resulting x-ray differ dramatically in these two configurations. Wiggler IDs yield very intense radiation over a wide spectrum while undulator IDs yield narrow and intense bands that can be tuned to the demand of the experiment.



INSERTION DEVICE (WIGGLER OR UNDULATOR)
PERMANENT MAGNETIC MATERIAL
Nd-Fe-B

Length @ 5 m

N

Gap @ 1-3 cm

Magnetic Period

S

$\lambda_0$

Electrons

Synchrotron
Radiation
X-rays
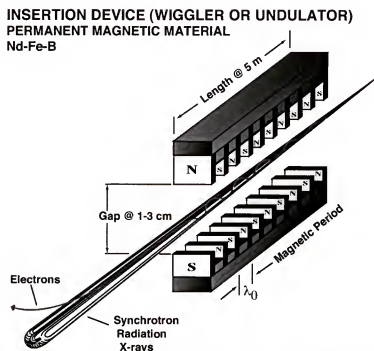
Figure 3-13. Diagram of a Type-A insertion device at the APS. Courtesy of the Advanced Photon Source, Argonne National Laboratory.

Principles of x-ray diffraction

The following discussion is taken mainly from the review papers by Kuzmenko et al. and Als-Nielsen et al.[179,180]

In both 3-D and 2-D crystal systems, diffraction from an array of crystal planes occurs when the Bragg condition is satisfied, i.e.,

$$\lambda = 2d \sin 2\theta \qquad\qquad\qquad 3\text{-}12$$

where $\lambda$ is the x-ray wavelength; $d$ is interplanar spacing; and $\theta$ is the angle between the plane and reflected beam. In terms of kinematics, this condition is equivalent to having the length of scattering vector $\boldsymbol{k}$ (given by $(4\pi/\lambda)\sin\theta = |\boldsymbol{k}_{out} - \boldsymbol{k}_{in}|$ ) equal to $2\pi d^*$ where $d^*$ is the reciprocal of the interplanar spacing. The vector $\boldsymbol{d^*}$ drawn from an arbitrary origin of the reciprocal lattice to any point in it is related to the Miller indices $hkl$ of the plane by the relation $\boldsymbol{d^*} = h\boldsymbol{a^*} + k\boldsymbol{b^*} + l\boldsymbol{c^*}$ where $\boldsymbol{a^*}$, $\boldsymbol{b^*}$, $\boldsymbol{c^*}$ are the reciprocal vectors of the unit-cell. In the case of the 2D system, the vector $\boldsymbol{c^*}$ is of course non-existent.
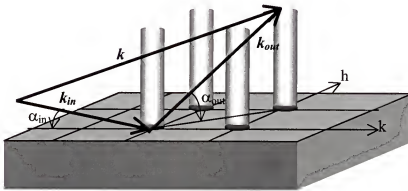


Figure 3-14. Scattering geometry in 2-D system where the lattice elements are shown as rods ("Bragg rods"). The incoming and outgoing wave vectors are defined by $\boldsymbol{k}_{in}$ and $\boldsymbol{k}_{out}$. The corresponding angles are $\alpha_{in}$ and $\alpha_{out}$. The scattering wave vector $\boldsymbol{k}$ has components $\boldsymbol{k}_{xy}$ parallel to the monolayer plane and $\boldsymbol{k}_z$ normal to it. Adapted from J. Als-Nielson, et al.[180]

The components of the scattering vector $\boldsymbol{k}$ given by $\boldsymbol{k}_{xy}$ and $\boldsymbol{k}_z$ define the inplane ordering of the 2D crystal. All diffraction patterns that have been measured so far showed that the monolayer is a mosaic of randomly ordered domains (a 2D "powder"). Consequently, a crystalline region of the right orientation would always be in the path of the incident beam and result in a diffraction pattern in the direction of the horizontal compo-

nents $k_{xy}$. The component $k_z$ is determined by the vertical electron density distribution in the molecules.

In grazing incidence x-ray diffraction, the angle $\alpha_{in}$ is held below the total external reflection to maximize sensitivity and minimize scattering from the subphase. Snell's law allows the calculation of the critical angle (see Figure 3-15):

$$n_1 \cos \alpha_{in} = n_2 \cos \alpha_r \qquad 3\text{-}13$$

For air which has $n_1 = 1$ and $n_2 < 1$ for hard x-rays, the critical angle for external reflections is

$$\alpha_c = \cos^{-1}(n_2) \qquad 3\text{-}14$$

The refractive index $n_2$ can be then be calculated from[181]

$$n_2 = 1 - \frac{\lambda^2 \rho r_o}{2\pi} \qquad 3\text{-}15$$

where $\lambda$ is the wavelength, $\rho$ is the electron density, and $r_o = 2.83 \times 10^{-13}$ cm is the classical electron radius. For the air-water interface at $\lambda = 1.24$ Å (10 keV) and the knowing that the electron density in the water phase is 0.335 Å$^{-3}$, the critical angle for total external reflection $\alpha_c \approx 2.1$ mrad. The refractive index for x-ray radiations at $\lambda \sim 1$ Å can be approximated directly from the real component only (as seen in Eqn. 3-15) since the complex component is small and can be neglected for practical purposes.
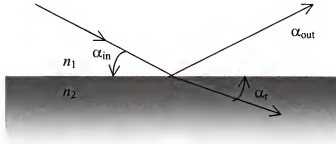
Figure 3-15. Diagram showing the incident beam impinging the surface at an angle $\alpha_{in}$ (where $\alpha_{out} = \alpha_{in}$) and the beam being refracted at an angle $\alpha_r$. The refractive index of the material is $n_1$ while the medium about it has a refractive index of $n_2$.

For the incident angle $\alpha_{in} < \alpha_c$, an evanescent wave will be the transmitted and propagate along the surface. This propagating plane wave will have an exponentially damped amplitude in the inward direction normal to the surface. The wave is also characterized by a penetration length that is independent of $\alpha$ as long as $\alpha < \alpha_c$. In addition, the penetration length at $\alpha_{in}/\alpha_c \ll 1$ is independent of the wavelength $\lambda$ and is only a function of the inherent property of the material.[179] At the water surface, Als-Nielsen[180] estimated that the penetration length is in the order of 50Å for $\alpha_{in} < 0.5\alpha_c$, making it highly surface sensitive. This evanescent wave is responsible for the diffraction of crystalline materials at the water surface and forms the basis for grazing incidence x-ray diffraction.

X-ray reflectivity technique

Specular x-ray reflectivity is another scattering technique that is relevant to the characterization of Langmuir and Langmuir-Blodgett films. As in x-ray diffraction and other scattering techniques, specular reflectivity consists of measuring x-ray intensity reflected off a surface. However, unlike in x-ray diffraction, the incident and reflected angles are equal so that *k* is directed normal to the surface and is therefore sensitive to

structures that are parallel to the surface. A good introduction in this area can be found in a paper by Chason and Mayer.[182]

Most applications of x-ray reflectivity have been on the characterization of Langmuir-Blodgett films such as that by Lvov and coworkers[183] who investigated the superlattice structure of a complex multilayer film of polyelectrolytes. Li et al.,[184] on the other hand, performed x-ray reflectivity studies of diblock copolymers in an attempt to relate the structures of their surface micelles in Langmuir films and as LB films. Detailed discussions of more applications and the practice of x-ray reflectivity can be found elsewhere.[185-188]

<center>Other Techniques</center>

Several other analytical tools are used to characterize monolayer and transferred multilayer films. These techniques include surface electrical measurements and

Surface Potential Measurements

One of the basic electrical measurements that can be done to characterize monolayers at the interface is surface potential measurement. By assuming that the dipole moments of $n$ molecules at the interface are additive, Davies and Rideal[11] applied the Hemholtz equation to obtain the surface potential $\Delta V$ for any interface

$$\Delta V = 4\pi n \mu_{total} \qquad \text{3-16}$$

where $\mu_{total}$ is the net dipole contribution. Measuring the surface potential $\Delta V$ (using techniques discussed in Gaines,[10] Adamson,[189] and Davis[11]) can provide a good insight into the changes in the dipole moments at the interface and hence the orientation of the molecules. In addition, by holding the monolayers at constant surface pressure to maintain the

same molecular orientation, the surface potential can be used to measure the kinetics of a reaction in monolayers.[189]

## UV-Vis, Infrared and other Spectroscopic Techniques

Like in any other techniques for monolayer characterization, the main problem limiting the application of various spectroscopic techniques is the very weak signal originating from the monolayer material. Thus, for example, UV-Vis spectroscopy is limited to materials which have strongly absorbing chromophores such as porphyrins[190,191] Useful information that can be obtained includes molecular aggregation and complexation,[191,192], level of mixing in the monolayer,[193] photoisomerization,[194] and phase transitions[195]

Phase behavior in Langmuir films is most often studied by infrared spectroscopy.[196] Reflection mode is preferred[62,197] rather than the more conventional transmission mode where the intense absorption signal of water makes it impractical. Using this technique, Baekmark[63,64] studied the phase transitions in polymeric Langmuir films.

Fluorescence spectroscopy coupled with near-field scanning optical microscopy (FL-NSOM) was also used to probe the nanoscale structure. In stained phospholipid monolayers deposited on glass substrates at moderate surface pressures, the FL-NSOM images revealed the phase separations and phase transitions in the monolayer as it is compressed.[198]

## Summary

This chapter gave an overview the various experimental techniques used to characterize Langmuir films. The discussions were not intended to be comprehensive but just enough to cover techniques that are relevant to this work.

The classical technique of pressure-area isotherm measurement still serves as the core of most analytical tools. It is simple and convenient to perform and gives fundamental insight into the phase behavior of monolayers. Various other techniques such as rheological measurements are important in studying the flow behavior of monolayers as well as their mechanical stability. The importance of understanding these and other monolayer properties have fundamental and practical significance

CHAPTER 4
THE CHEMISTY AND INTERFACIAL BEHAVIOR OF ALKOXYSILANES

Introduction

Monomolecular-thin films prepared at an aqueous interface continue to provide an attractive means to form well-defined molecular assemblies for surface modification and ultrathin-film applications. For these purposes, high molecular weight, polymeric Langmuir-Blodgett films[199] have the potential of being more robust materials compared to their low-molecular weight analogs. Of course, the same entanglement of polymer backbones which gives rise to the transient network formation and attractive mechanical properties in bulk polymeric materials is less effective in a quasi-two dimensional LB layer. Several groups have considered cross-linking monolayers as a means of enhancing properties of these materials.[200-205]

Kloeppner recently demonstrated that an extended network formed from polymerization of bolaform alkylaniline monolayers results in a sufficiently stable and flexible material in which individual self-supporting monolayers could be drawn from the water surface as thin films and fibers of macroscopic size.[206] Can the chemical transformations in these types of reactions be more quantitatively correlated to the resulting physical properties?

The results of this study will show some insight on the network formation of amphiphilic n-octadecyltrimethoxysilane (OTMS, $CH_3(CH_2)_{17}Si(OCH_3)_3$) at air/water interfaces by measuring changes in surface rheology of the reacting system in real time. Such measurements should be broadly applicable to other reactive amphiphiles.

Background

The sol-gel route towards the preparation of advanced materials has been pursued with great rigor in recent years.[207-209] Applications of materials derived from sol-gel process ranges from mechanical stabilization[210], interlayer dielectrics[211], catalysis,[212-214] and photonics.[215,216] Typically, alkoxides of silanes (Si(OR)$_3$) where R=Me, Et) are the primary precursor materials although SiH$_3$[217] and SiCl$_3$[218] have also been used. One of the advantages of the silane chemistry is the stability of the Si-C bond against hydrolysis and the thermal treatment that usually accompany sol-gel processing.

The chemistry of silane alkoxides and related compounds is well understood and numerous NMR studies have been done to study the kinetics and mechanism of this reaction in solution.[219,220]

In bulk solutions, alkoxysilanes are well-known to undergo acid or base catalyzed hydrolysis and form siliceous materials.[221] Polysilsesquioxanes, RSiO$_{3/2}$, offer intriguing models to examine this; as in this work, the *R* group can be strongly hydrophobic. Such materials form oligomeric cage, polymeric ladder, and three dimensional network structures depending upon reaction conditions and the nature of the *R* group.[209] Equations 4-1 to 4-4 shows the hydrolysis and condensation reactions in alkoxysilanes.



4-1



4-2



4-3

$$R{-}O \underset{\underset{R}{|}}{\overset{\overset{R'}{|}}{C}} OH \ + \ HO \underset{\underset{R}{|}}{\overset{\overset{R'}{|}}{C}} O{-}R \ \rightleftharpoons \ R{-}O \underset{\underset{R}{|}}{\overset{\overset{R'}{|}}{C}} O \underset{\underset{R}{|}}{\overset{\overset{R'}{|}}{C}} O{-}R \ + \ H_2O \qquad \qquad 4\text{-}4$$
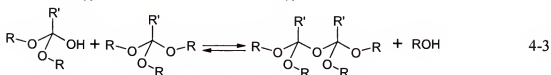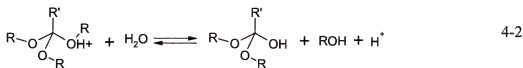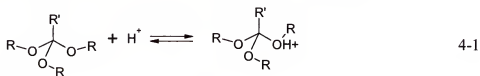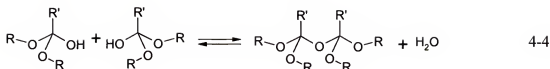
The above equations are actually an oversimplication of the reactions occurring in alkoxysilanes. Figure 4-1 below shows a complete reaction map for an alkyltrialkoxysilane. The set of $(x, y, z)$ numbers represent the species of alkoxysilane where $x$ indicates the number of –OR substitutions, $y$ the number of –OH substitutions, and $z$ the number of –O-Si substitutions.[222] The figure also depicts vertical reactions (e.g., (0,3,0) → (0,2,0)) as water-producing reactions and diagonal reactions (e.g., (3,0,0)→(2,0,1)) as alcohol-producing reactions.

$$
\begin{array}{ccccccc}
(3,0,0) & \rightarrow & (2,1,0) & \rightarrow & (1,2,0) & \rightarrow & (0,3,0) \\
 & \searrow & \downarrow & \searrow & \downarrow & \searrow & \downarrow \\
 & & (2,0,1) & \rightarrow & (1,1,1) & \rightarrow & (0,2,1) \\
 & & & \searrow & \downarrow & \searrow & \downarrow \\
 & & & & (1,0,2) & \rightarrow & (0,1,2) \\
 & & & & & \searrow & \downarrow \\
 & & & & & & (0,0,3)
\end{array}
$$

water-producing condensation

alcohol-producing condensation
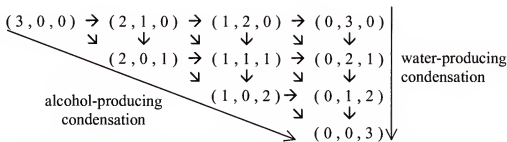
Figure 4-1. A map of the various hydrolysis and condensation reaction paths in a trialkosysilane. From Britt and Hlady.[222]

Langmuir monolayers of OTMS at the air/water interface have been reported[222,223] to form a condensation product. The chemical composition of the various products have been confirmed by electron spectroscopy for chemical analysis (ESCA)[224] and by inelastic electron tunneling spectroscopy.[225] While the molecular weight and architecture of the product have not been reported, some have suggested that OTMS and similar materials should form linear[223,224] rather than network polymers due to the 2D restrictions in the environment around the silane head group.

## Experimental Method

### General

All monolayer and polymerization studies were conducted on KSV LB5000 (KSV, Finland) equipment at 25°C using a trough and barriers made of PTFE. The trough measured 150 x 675 mm². The surface pressure ($\Pi$) measurements were obtained using the Wilhelmy plate technique. High-purity water passed through a 4-cartridge Milli-Q (Millipore) filter system was used (resistivity $\geq 18 M\Omega$-cm). The pH of the subphase was adjusted with HCl. n-Octadecyltrimethoxy silane (OTMS) (>95%, Gelest. Inc.) was used as received. To prepare the spreading solution, a small amount of OTMS was added in a volumetric flask containing chloroform (ACS Grade, Fisher) to make up a solution with an approximate concentration of 1 mg mL$^{-1}$. During the preparation of the solution, utmost care was taken so that the exposure of OTMS to the atmosphere is minimized. The spreading solutions were placed in cold storage until needed.

### Surface Viscosity Measurement

Surface viscosity experiments were done on an alternating trough system designed by KSV. This is configured to have dual control system so that the two barriers can be controlled by two independent feedback systems.

Figure 4-2 shows a drawing of the Teflon canal. The canal edges were angled at 72° to compensate for PTFE/water contact angle. Width and length were 1.35 and 93.78 mm, respectively. In the experiments, the surface pressure in which the amphiphile is initially spread was set at 8 mN m$^{-1}$. A piece of PTFE block was placed at the entrance of the canal to prevent the monolayer from flowing to the other side. Once the experiment is started, that PTFE piece is removed and the pressure gradient was maintained at 1.0 mN m$^{-1}$.

Figure 4-2. Teflon canal used in the surface viscometry measurement. The knife-edges are angled at 72°.

For an insoluble monolayer flowing under a pressure gradient $\Delta\Pi$ though a canal of width $w$ and length $L$, the surface viscosity $\eta_s$ can be related to the flow rate by the equation

$$\eta_s(t) = \frac{\Delta\Pi w^3}{12LQ(t)} - \frac{w\eta_o}{\pi} \qquad 4\text{-}5$$

where $\eta_o$ is the bulk viscosity of the subphase. Equation 4-5 is the 2D analog of the Poiseuille formula and derived from Navier-Stokes approximation for laminar flow.[157]

For monolayer films of significant surface viscosity such as a cross-linking system, Eqn. 4-5 can be approximated as

$$\eta_s(t) = \frac{\Delta\Pi w^3}{12LQ(t)} \qquad 4\text{-}6$$

since the value of the second term is less than 0.4 smP (surface milliPoise) at 25 °C and for canal width $w\sim1.3$ mm. A similar approximation was used by Rolandi et al.[226] to calculate the surface viscosity of polymerized films.

The area flow rate $Q(t)$ is calculated from $Q(t) = \Delta A_f/\Delta t$ where $\Delta t$ is the time interval of measurement and $\Delta A_f$ is the change in area in the high-pressure side of the canal.

The change in area was calculated indirectly from the known width $w_t$ of the trough and the barrier displacement $\Delta s$, i.e., $\Delta A_f = w_t \times \Delta s$.

Since the measurement involves a reacting system, the area change due to the reaction should be deconvoluted from the area change due to the actual flow of material across the canal, i.e.,

$$A_f = (MMA)_t \left[ \frac{A_o}{(MMA)_o} - \frac{A_t}{(MMA)_t} \right]$$

4-7

where $A_o/(MMA)_o$ is the original number of molecules and $A_t/(MMA)_t$ is the remaining number of molecules at time $t$ in the high-pressure side. The mean molecular area at time $t$, $(MMA)_t$, was obtained independently in a parallel isobaric area relaxation experiment of OTMS at identical conditions and no flow. The difference is then multiplied by the mean molecular area at that point of the reaction to obtain the amount of material that has flowed across the canal.

Brewster Angle Microscopy

Studies using Brewster angle microscopy (BAM) were done using a NanoFilm Technologie BAM-1 system (NFT, Germany) with a 10 mW HeNe laser ($\lambda$=632.8 nm). The incident angle of the laser beam was carefully adjusted to where the intensity of the reflected beam off a clean water surface is zero. The polarization of the laser beam was also adjusted to where the reflection is at the minimum (p-polarized). Directly underneath where the beam is incident to the subphase, an optical filter was placed to absorb any parasitic scattering.
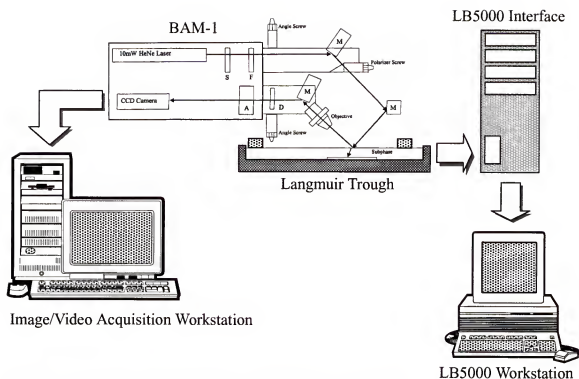
Figure 4-3. Schematic of the Brewster angle microscopy setup.

The schematic of the setup is shown in Figure 4-3. For image acquisition, the output of the BAM CCD camera was connected to a PC workstation which has a high-accuracy and low-noise monochrome frame grabber card (DT3155, Data Translations). The original setup involved a VCR and video monitor attached directly to the CCD output. Images were later captured from the VCR using Snappy® (Play, Inc.) device that is attached to the parallel port of a PC. Not only that the acquisition is slow in this case but the process of recording to a VCR degrades the fidelity of the images that are acquired. The fully digital image acquisition setup proves to be a significant improvement.

ImageTool (Ver. 2.00, University of Texas Health Science Center) was used as the image acquisition software. All images shown here are raw and unfiltered except for some contrast and brightness adjustments. In very few instances, a "jitter correction" filtering was used to fix alignment problems between the odd and even row pixels.

Data acquisition and control of the LB5000 system is done using a separate work-station running MS-DOS.

<div align="center">Results and Discussion</div>

Isotherms

The behavior of OTMS and related amphiphiles was investigated as they are spread at the air-water. Typically, 70-80 µL of a 1 mg mL$^{-1}$ solution is required to cover a trough with an area of 1000 cm$^2$. Once the solution is spread, compression is commenced within two minutes to minimize any reaction that might occur prior to the start of the ex-periment.

The chemical structures of the amphiphiles used in this study are presented in Figure 4-4 and the resulting surface pressure-area (Π-A) isotherms in Figure 4-5.

The Π-A curve of OTMS exhibited an onset of an *LE* phase between 75-80 Å$^2$ which continues until around 40 Å$^2$ where an apparent plateau follows. The break in the curve towards the plateau region was observed to be highly dependent on the compres-sion rate. On average, this break is manifested at surface pressures between 10-12 mN m$^{-1}$. On further compression, a less compressible region starts to appear just below 30 Å$^2$. At much smaller mean molecular area (MMA) another plateau appears where the methoxy groups are assumed to be in staggered positions to minimized the mo-lecular area.[227] This feature is then followed by slowly sloping region which can only be attributed to the final collapse of the monolayer.
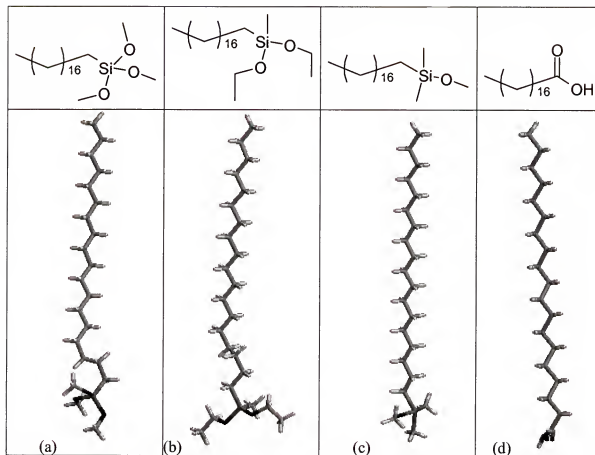
Figure 4-4. Chemical structures and molecular models of amphiphiles used in this study. (a) n-Octadecyltrimethoxysilane (OTMS); (b) n-Octadecylmethyldiethoxysilane (OM-DES); (c) n-Octadecyldimethylmethoxysilane (ODMS); and (d) Stearic Acid (SA).

The first plateau region is ideally a first-order phase transition and should be a sharp discontinuity in the Π-A curve. In the case of OTMS, this phase transition only becomes sharp at low compression rates. Vidon and Leblanc[223] have suggested that because of the hydrophobicity of the alkoxy headgroup, only a minimal amount of work is required for the *LE* phase to collapse and should result in a clear first-order transition. However, its long alkyl chain enhances its hydrophobicity such that the monolayer can become unstable at room temperature. These two factors both contribute to yield the indistinct phase transition between the *LE-LC* regions. Furthermore, the formation of the weak *LC* phase has been suggested to be due to the van der Waals interaction of the alkyl

groups being counteracted by the tendency of the large and hydrophobic alkoxy headgroups to form a liquid phase.[223] This becomes apparent when the isotherm of OTMS is taken at pH 3.5 (see Figure 4-6). Here, the methoxy headgroups have been hydrolyzed to a more hydrophilic silanol groups and the isotherm shows a more distinguishable *LC* phase. Also, the monolayer does not collapse even at $\Pi = 60$ mN m^{-1}. Stearic acid (SA) shows similar feature because of the more hydrophilic and smaller carboxyl headgroup.
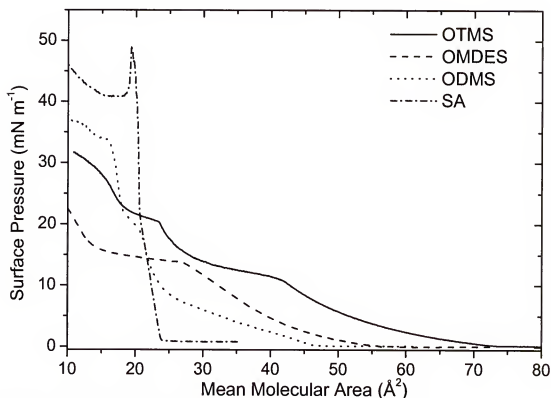


Figure 4-5. Isotherms of obtained from the amphiphiles in Figure 4-4.

Pressure-area isotherms of two other alkoxysilanes are shown for comparison. These silanes differ from OTMS in the alkoxy substitution at the silicon. n-Octadecylmethyldiethoxysilane (OMDES) with a relatively large headgroup exhibits a wide *LE* phase between 60-30 Å². On further compression, only a single transition is

noted and this probably continues towards the collapse of the monolayer altogether. The large headgroup apparently prevents the alkyl chain from close-packing hence the absence of any hint of a *LC* phase. This is in great contrast of the isotherm exhibited by n-octadecyldimethylmethoxysilane (ODMS). The *LE* of ODMS is apparent between 45-27 Å$^2$, followed by the *LC* phase at around 25 Å$^2$. A phase transition appearing at $\Pi = 20$ mN m$^{-1}$ leads to a highly incompressible phase which is almost certainly the solid phase made of closely-packed ODMS molecules. Of the three silanes studied, only ODMS showed a distinct solid phase and exhibited the highest collapse pressure at approximately 34 mN m$^{-1}$.

Kinetics of Monolayer Reaction

The pH-dependence of the reaction kinetics of OTMS is very apparent from the two isotherms shown in Figure 4-6. These two isotherms were obtained in the same Langmuir trough and compressed at the same rate of 5 mm min$^{-1}$. At this compression rate, a mean molecular area of 25 Å$^2$ is reached after approximately 46 min. In the case of OTMS spread over a pH 3.5 subphase, enough hydrolysis must have occurred while the barriers are compressing to result in the reduction of the onset of the *LE* phase to 32 Å$^2$. This becomes obvious when OTMS is compressed at 100 mm min$^{-1}$ at the same subphase. At this rate, it takes less than 3 mins to get to 25 Å$^2$ and results in a negligible difference in the isotherm.
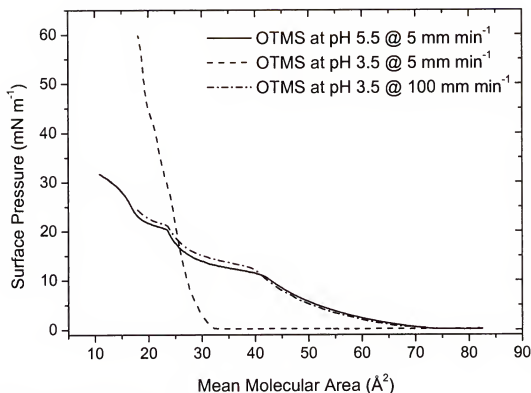
Figure 4-6. Pressure-area isotherms of OTMS at pH 5.5 and 3.5.

The kinetics of reactions in 2D is conveniently measured in a Langmuir trough either by monitoring the change in the surface pressure at constant area ("isochoric") or the change in mean molecular area at constant pressure ("isobaric") experiments. Both of these methods have their own advantages and disadvantages. In an isochoric approach, an ideal condition is accomplished in which the molecules have the same molecular area as the reaction progresses thus they would have the same collision rate regardless of the extent of the reaction. Linden et al.[228] found this technique suitable to investigate the reaction of OTMS since extensive hydrolysis/condensation is assumed to have taken place before reaching the target pressure if an isobaric experiment is instead preferred. On the other hand, isobaric technique becomes ineffective when significant molecular area reduction occurs. When such condition takes place the surface pressures drops close to zero surface pressure and any possibility of measuring the kinetics of the reaction becomes

difficult. This is where isobaric technique will do extremely well and is actually preferred in most cases.[229] In addition, isobaric technique provides a measurable quantity, i.e., MMA that can be correlated with results from complementary techniques such as x-ray diffraction.

Packing density and reactivity

A series of $A(t)$ isobars at pH 3.5 subphase are shown in Figure 4-7a. These isobars were obtained at surface pressures of 2, 8, 15, 20 and 25 mN m$^{-1}$ representing different surface concentrations corresponding to increasing packing densities, respectively.

Reactions made at the *LE* phase ($\Pi = 2$ and 8 mN m$^{-1}$) and to some extent reactions done at the *LC* phase ($\Pi = 15$ and 20 mN m$^{-1}$) showed the expected area reduction consistent with the hydrolysis of the methoxy groups. However, the extent of area reduction as it approaches the asymptote differs significantly between the different isobars with the least dense monolayer showing the greatest area reduction. Figure 4-7b illustrates the relationship of surface density to the degree of area reduction which was calculated from

$$\Delta A = \frac{A_i - A_\infty}{A_i}$$

4-8

where $A_i$ is the initial MMA and $A_\infty$ is the known ultimate MMA of 21 Å$^2$, determined from later experiments conducted at more extended reaction times.

The apparent linear relationship between the decrease in the MMA to the surface density of the monolayers agrees with the idea that during the hydrolysis/condensation reactions, OTMS remains as a stable monolayer and that insignificant amount is lost either by dissolution to the subphase or by other mechanisms.
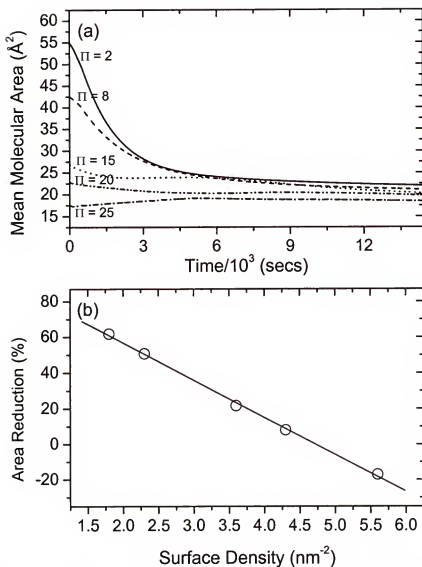
Figure 4-7. (a) $A(t)$ isobars of a reacting OTMS at various surface pressures and at pH 3.5; (b) Area reduction relative to the surface density of the monolayers.

The monolayer prepared at $\Pi = 25$ mN m$^{-1}$ exhibited an isobar in which the molecular area appears to increase with time. This is also exhibited to a lesser degree by the monolayer compressed at $\Pi = 15$ mN m$^{-1}$. Two possible factors can account for the expanding MMA. Since the monolayers are highly compressed initially in these conditions, the expansion might indicate a dynamic relaxation of the monolayer in an attempt to reach the equilibrium molecular packing. Another reason for the expansion can be specu-

lated by recognizing the reaction mechanism involved. The initial protonation (see Eqn. 4-1) of the alkoxide group to form the oxonium ion intermediate brings about electrostatic repulsion between the headgroups resulting in the initial expansion. This was earlier noted by Britt and Hlady.[230] Eventually, a net area reduction will prevail as the alkoxide groups are converted to silanols or Si-O-Si covalent bonds.

Kinetics of hydrolysis in OTMS monolayer

The hydrolysis and condensation reaction of alkoxysilanes in an acidic medium can proceed in a variety of routes. The complexity of the possible reaction paths is depicted in Figure 4-1 which shows at least 10 species are involved in 18 reactions. The diagram does not include protonation equilibria and the statistics on the formation of oligomeric species which can further complicate any attempt to study this system quantitatively. Experimental techniques based on $^{29}Si$ nuclear magnetic resonance is the most popular analytical method to study the kinetics of this system in solution.[219,231,232] The interest in $^{29}Si$ NMR is made possible by the high sensitivity of the Si nucleus towards changes in its chemical environment. Also, the availability of NMR methods such as IN-EPT (insensitive nuclei enhanced by polarization transfer) and DEPT (distortionless enhancement by polarization transfer) have allowed quantitative determination of the composition of the reaction product.[219,220]

*In situ* investigations of kinetics of simple reactions (e.g., one step *reactant →  product* reaction) at the air-water interface on the other hand can be as quantitative as other techniques. However, in a complicated reacting system in which several species and reactions are involved, there exists a difficulty in establishing the actual reaction kinetics and mechanism involved because there is no information about speciation of reactants and products. This is clearly shown in this system involving *in situ* study of the reaction

in OTMS monolayer where the experimental data is only limited to MMA in the monolayer. This is not adequate to completely describe the kinetics of the reaction since some of the products have very similar MMA values. For example, the MMA of the ultimate hydrolysis product, silanetriol, is not much different from the monomeric unit of the polysiloxane condensation product.[233] While the importance of obtaining the overall kinetics of the reactions is recognized, it might only be prudent, given the situation, to limit the discussion to the hydrolysis stage at the early stages of the reaction where it is the predominant reaction. The attribution that the initial process is due to hydrolysis alone is valid since for the condensation reaction to start, a significant concentration of silanol must be present.
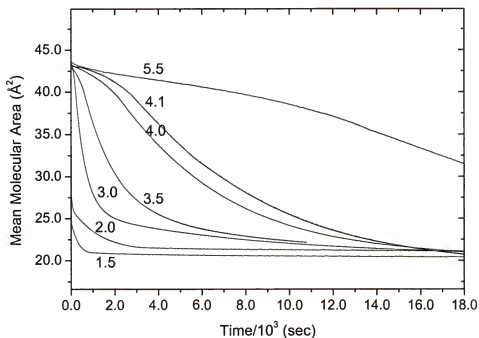


Figure 4-8. $A(t)$ isobars of OTMS at various subphase pH. $\Pi = 8$ mN m$^{-1}$, T = 25°C.

Figure 4-8 shows a series of isobars corresponding to the area relaxation of OTMS at different subphase pH values and $\Pi = 8$ mN m$^{-1}$. As expected, the area of the monolayer decreases with time and the apparent rate of area reduction is inversely related

to the subphase pH. The isobar at pH 5.5 shows two distinct segments in the curve start-

ing with a lower-sloped segment followed by a segment at a steeper slope. The point of

inflection was estimated at t = 13 x $10^3$ sec in pH 5.5 subphase and appears to occur at

earlier times as the pH of subphase is varied to lower values, disappearing eventually at

much lower pH. It is apparent from the curves at higher pH that the change in MMA ap-

pears to be slower initially then gradually accelerate with time. This "induction" period

can be accounted for by two factors related to the initial protonation of the OTMS

monolayer. First, the protonation step would take time before an equilibrium concentra-

tion of oxonium ions is reached. This process would be significantly slower at higher pH.

The other contributing factor is the expansion of the MMA due to electrostatic interaction

between oxonium ions which offsets the area reduction caused by hydrolysis. Eventually,

as the equilibrium condition is reached, a net reduction of MMA is observed. In subse-

quent analysis, the rate of hydrolysis was then calculated from the steeper-sloped seg-

ment of $A(t)$ curves.

To simplify the analysis, it is assumed that the hydrolysis reactions for the three

alkoxy groups have equal rates. Also, OTMS and the related silanols and siloxanes are

assumed to stay at the interface and that the hydrolysis product $CH_3OH$ diffuses into the

subphase. In addition, it is assumed that the resulting products consisting of silanols and

siloxanes form an ideal mixture with the original monolayer so that the areas are additive.

In this case, $\xi$, the fraction of reactant that has reacted can be shown to be:[10,189]

$$\xi = \frac{n}{n_o} = \frac{A - A^\infty}{A^o - A^\infty}$$ 4-9

where $n_o$ and $n$ are the original and remaining moles of reactant at time $t$, respectively; $A$,

$A^o$, $A$  are the mean molecular areas at time $t$, at the start, and at the end of the reaction.

With these assumptions, the kinetics of the hydrolysis reaction can now be examined. The reactions involved are Eqns. 4-1 and 4-2:

$$R'–Si(OR)_3 + H^+ \rightarrow R'–Si(OR)_2ORH^+ \qquad \text{4-1}$$

$$R'–Si(OR)_2ORH^+ + H_2O \rightarrow R'–Si(OR)_2OH + ROH + H^+ \qquad \text{4-2}$$

By assuming that Eqn. 4-1 is fast, the overall net equation can be shown to be

$$R'–Si(OR)_3 + H_2O \rightarrow R'–Si(OR)_2OH + ROH \qquad \text{4-10}$$

The rate equation can then be expressed as a pseudo-first order since $H_2O$ is in excess. Hence,

$$\frac{d[SiOR]}{dt} = -k[SiOR] \qquad \text{4-11}$$

where $k$ is the rate constant and $[SiOR]$ is the concentration of the alkoxysilane. Integration                                                                                        yields

$$\xi = \frac{[SiOR]}{[SiOR]_o} = \exp(-kt) \qquad \text{4-12}$$

$$\ln \xi = -kt \qquad \text{4-13}$$

The curves of $\ln \xi$ vs. $t$ (see Figure 4-9) were examined and the initial linear segment was assumed to be a direct result of the hydrolysis reaction occurring. Ideally, the linear regression resulting from the use of Eqn. 4-13 should yield a zero intercept on the ordinate ($\ln \xi$ axis). However, significant deviation was observed especially at low pH. This was seen as an indication of the extent of hydrolysis that has already occurred before the experiment was actually started.
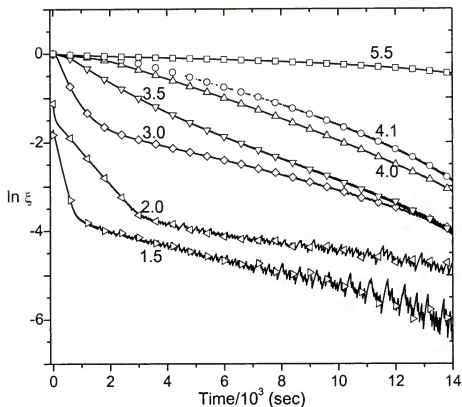
Figure 4-9. Plots of ln ξ against time for reactions at various subphase pH values.

Table 4-1. Result of linear regression of the $A(t)$ data using Eqn. 4-13; $k$ is the calculated slope; $\alpha$ is the intercept; $R$ is the correlation coefficient; and $t$ is the approximate time interval at which the linear regression was calculated.

| pH | $k \times 10^{-4}$, sec$^{-1}$ | $\log k$ | $\ln \alpha$ | $R$ | $t$ |
|-----|------|-------|-------|-------|------------------|
| 1.5 | 27.2 | -2.58 | -1.71 | -0.99 | 0-600 sec |
| 2.1 | 7.4  | -3.13 | -1.46 | -1.00 | 0-1400 sec |
| 3.0 | 12.6 | -2.90 | 0.06  | -1.00 | 0-2000 sec |
| 3.5 | 3.4  | -3.47 | 0.05  | -1.00 | 1000-5000 sec |
| 4.0 | 2.4  | -3.62 | 0.43  | -1.00 | 2000-13000 sec |
| 4.1 | 2.3  | -3.64 | 0.60  | -0.99 | 2000-14000 sec |
| 5.5 | 0.71 | -4.15 | 0.53  | -1.00 | 10000-20000 sec |

Since most kinetic studies of alkoxysilane hydrolysis in the bulk are done in the presence of very small amount of water, there are very few similar studies in which these results can be compared with. Recently, Beari et al.[234] studied a series of organofunctional alkoxysilanes in dilute aqueous solution using $^1$H and $^{29}$Si NMR. Their results for

the hydrolysis of 3-methacryloxypropyltrimethoxysilane (2% in solution) revealed an over-all first-order kinetics with a rate constant of $2.8 \times 10^{-4}$ sec$^{-1}$ at pH 6. This result is in agreement and yields a rate constant that is in the same order of magnitude as the one obtained from the isobaric $A(t)$ curves.

Having obtained the various rate constants at different pH, it is now possible to obtain a direct relationship between rate of reaction and the pH of the subphase to illustrate the catalytic effect of the hydronium ion.

Assuming a general acid-base catalysis[235]

$$\text{Rate} = k_o[\text{SiOR}] + k_{H^+}[\text{SiOR}][H^+] + k_{OH^-}[\text{SiOR}][OH^-] \qquad 4\text{-}14$$

where $k_o$ is the rate constant for the uncatalyzed reaction; $k_{H^+}$ is the rate constant for catalysis by hydrogen ions with a bulk concentration of the hydronium ions; and $k_{OH^-}$ is the rate constant for catalysis by hydroxide ions with a bulk concentration of hydroxide ions. A first-order rate constant can be defined as

$$k \equiv \frac{\text{Rate}}{[\text{SiOR}]} \qquad 4\text{-}15$$

and therefore,

$$k = k_o + k_{H^+}[H^+] + k_{OH^-}[OH] \qquad 4\text{-}16$$

For reactions in an aqueous environment, Eqn. 4-16 can be written as

$$k = k_o + k_{H^+}[H^+] + \frac{k_{OH^-}k_w}{[H^+]} \qquad 4\text{-}17$$

where $k_w = [H^+][OH^-]$. In the acidic subphases in which the system that was studied, the third term of Eqn. 4-16 can be neglected and so in the low-pH region, the rate constant $k$ is essentially equal to $k_{H^+}[H^+]$. Therefore,

$$\log k = \log k_{H^+} + \log[H^+] \qquad\qquad 4\text{-}18$$

or

$$\log k = \log k_{H^+} - pH \qquad\qquad 4\text{-}19$$

From the linear regression analysis of the data in Table 4-1, the actual hydrolysis

rate constant, $k_{H^+}$, was calculated to be 8.1 x 10$^{-3}$ mol$^{-1}$ L sec$^{-1}$.
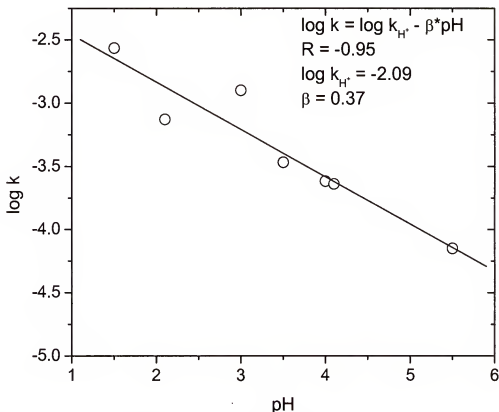


Figure 4-10. Acid catalysis in the hydrolysis of OTMS.

The slope, denoted by β, was also calculated to be 0.37 indicating a likely differ-

ence in the bulk pH and the actual pH near the interface. The difference between bulk and

surface concentration of ions is actually well established and the gradient can be ex-

pressed in terms of the Boltzman distribution of the ions:[236]

$$[\text{H}^+]_s = [\text{H}^+]_b \exp\left(-\frac{e\psi}{kT}\right) \qquad \text{4-20}$$

where the hydronium concentration $[\text{H}^+]$ at the surface and in the bulk is denoted by the subscripts $s$ and $b$, respectively; $e$ is the electronic charge; $\psi$ is the interfacial potential; $k$ is the Boltzman constant; and T is the absolute temperature. In logarithmic terms,

$$\text{pH}_s = \text{pH}_b + \frac{e\psi}{2.3kT} \qquad \text{4-21}$$

Referring back to the interfacial reaction of OTMS, it is likely that immediately upon spreading the interface takes up a potential $\psi$ different from that of the bulk subphase, similar to what Peters has noted.[237] In this case, the $\psi$ is negative[223] and will result in the hydronium ion being attracted towards the electronegative oxygen. The result would be that the surface would have a slightly lower pH compared to the bulk of the subphase. With this argument, it is possible that

$$\text{pH}_s = \beta\text{pH}_b \qquad \text{4-22}$$

Dynamic Surface Rheology

Experiments involving isobaric area relaxation that were discussed in the kinetics section gave an insight on the progress of hydrolysis reaction. However, very little information can be extracted from them regarding the structure formation resulting from subsequent condensation reactions. Two fundamental properties that probe such transformation will be discussed here.

Surface compressional modulus

The surface compressional modulus of a quasi-two dimensional monolayer is a measure of the film stiffness and generally should scale proportionately to the molecular weight increase similar to three-dimensional materials. The modulus was obtained by

applying brief mechanical stimuli *in situ* during the course of the hydrolysis and conden-
sation reactions. This was accomplished by introducing a series of periodic compression-
expansion cycles as shown schematically in Figure 4-11. Each compression-expansion
cycle gave rise to two isotherm curves; Figure 4-13 is a plot of the resulting series of sur-
face pressure/area/reaction time curves describing the compression cycles. Each curve is
an instantaneous record of mechanical properties at a defined point in the chemical reac-
tion.

The Gibbs compressional modulus is defined as

$$K^s = -\frac{d\Pi}{d\ln A} \qquad\qquad\qquad 4\text{-}23$$

where $\Pi$ is the surface pressure and $A$ is the molecular area in the film.[10] In the work, $K^s$
was calculated directly from the slope of the condensed region of the corresponding iso-
therm, at $\Pi \sim 20$ mN m$^{-1}$ and area centered at A $\sim 25$ Å$^2$. Between each compression-
expansion cycles (~80% of total reaction time) the monolayer was maintained at isobaric
conditions of $\Pi = 8$ mN m$^{-1}$. Control experiments at isobaric conditions determined that
the mechanical stimulus did not measurably change the reaction kinetics and that the
monolayer follows a similar area relaxation curve.
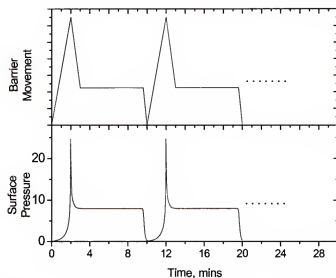
Figure 4-11. A diagram showing two cycles of the oscillatory compressive stimuli applied to the reacting monolayer; the bottom curve represents the measured surface pressure response. From Carino et al.[238]
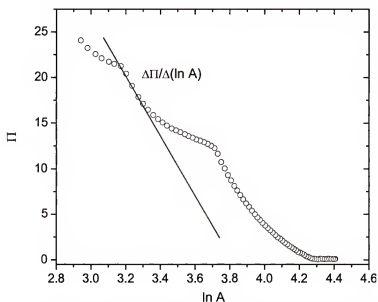


Figure 4-12. A diagram showing the section of the isotherm where $K^s$ were derived.
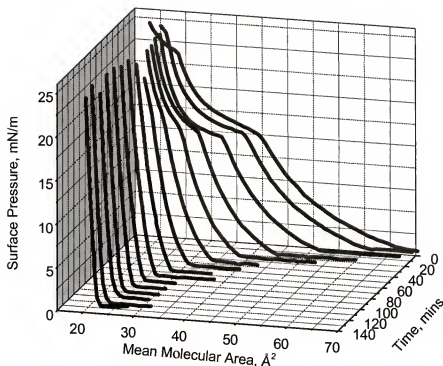
Figure 4-13. A typical set of Π-*A* isotherms at pH 3.5 subphase from which the plot in Fig. 4-14 was calculated; obtained between 0-25 mN m⁻¹ at 25°C. From Carino et al.[238]

As shown in Figure 4-14, $K^s$ for the reacting monolayer increases about tenfold with polymerization time in a non-linear manner. At the start of the reaction, $K^s$ has a value of 30 mN m⁻¹, increasing to a plateau at about 70 mN m⁻¹ from 20 - 60 mins. The modulus then increased exponentially and eventually became more constant at a value of about 280 mN m⁻¹. The sharp jump in the modulus near the end of the reaction suggests that a threshold degree of reaction is required to attain a critical concentration where possible entanglements or network links appear.

Additional chemical insight is obtained by plotting $K^s$ vs the mean molecular area as shown in Figure 4-15. The initial modulus increase observed in Figure 4-14 can now be attributed to an approximately 50% decrease in surface area, consistent with the methoxy-alcohol transformation expected from the hydrolysis reaction. The magnitude of the
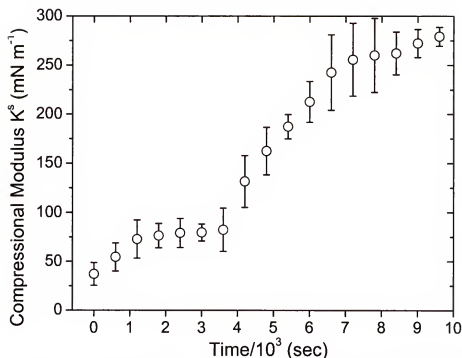
Figure 4-14. Surface compressional modulus of OTMS during reaction on a pH 3.5 sub-phase and at $\Pi = 8$ mN m$^{-1}$. From Carino et al.[238]

modulus may also be meaningful; for example, compressed monomolecular films of other common simple surfactants like stearic acid ($C_{17}H_{35}COOH$) and 1-decanol ($C_{10}H_{21}OH$)have surface compressional moduli of $1000 \pm 200$ and $2500 \pm 500$ mN m$^{-1}$,[239] respectively. Table 4-2 shows the relative compressional modulus at different phases of the monolayer.[11]

Table 4-2. Relative compressional modulus of different substances and states of the film. Adapted from Davies and Rideal[11]

| Monolayer | Compressional Modulus, $K^s$ |
|---|---|
| Clean Surface | 0 |
| Ideal | $\Pi$ |
| Protein (A≈1 m$^2$/mg) | 1 to 20 |
| Liquid Expanded | 12.5 to 50 |
| Liquid Condensed | 100 to 250 |
| Solid Condensed | 1000 to 2000 |
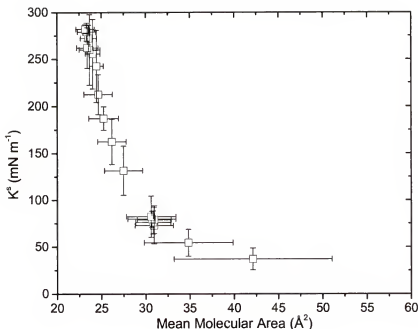
Figure 4-15. The surface compressional modulus $K^s$ vs mean molecular area of the reacting system calculated from data in Figure 4-14. Surface area is expressed as area per Si atom in the monolayer.

This dynamic transformation in the reacting OTMS monolayers can be explained in several ways. One of these is the fact that the during the time frame of the experiment, the system is still in a highly inhomogeneous state and that domains of close-packed and polymerized areas coexist with the *LE* phase. It is very likely that the compressional modulus measured here is limited by the compressibility of the *LE* phase rather than that of the close-packed domains. As the reaction progresses, the *LE* phase is continuously transformed into the close-packed domains, hence the increase in the modulus.

Another explanation is based on the percolation nature of the network formation and scaling behavior as proposed by de Gennes[240] and Stauffer[241]

Percolation theory describes in detail the phenomenon of gelation and is suitably applicable to explain the time dependence of various rheological properties of a reacting monolayer film. In the context of percolation theory, the monomers are assumed to occupy fixed sites in a periodic lattice. As the reaction progresses, bonds along the edges joining the fixed sites are formed and the conversion factor $p$ increases correspondingly. The gel point $p = p_c$ is identified as the point in which an infinite network or cluster starts to form. At this point, the material exhibits viscoelastic behavior[242,243] Figure 4-16 illustrates this dynamic process occurring in a reacting two-dimensional system, depicted with a hexagonal lattice structure to make it appropriate for comparison with the tri-functional OTMS. At the initial stage, molecular self-assembly and hydrolysis occurs (Frame 1). This is followed by the formation of individual small clusters made out of oligomeric structures resulting from the polycondensation reaction (Frame 2). As the reaction continues, further polycondensation reaction yields larger clusters characterized by a broad size distribution (Frame 3). At $p = p_c + \Delta p$ (Frame 4) where $\Delta p$ is positive and small, an infinite cluster is formed mixed with small amounts of finite clusters. This transition from $p < p_c$ to $p > p_c$ characterizes a sol-gel transition: at $p < p_c$ only a sol exists while at $p > p_c$ both sol and gel coexist in the matrix.[244]
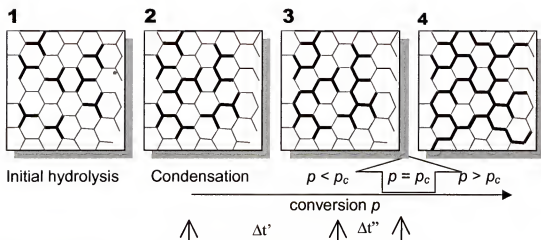
Figure 4-16. Evolution of structures in a network-forming material as the conversion increases. The monomers are considered to be fixed at the lattice points. The conversion factor $p$ is the probability that neighboring molecules can react together and form a bond (dark lines). At $p = p_c$, half of the total number of reactive groups are expected to have reacted.

At the point just above the threshold $p_c$, the material is believed to have a self-similar structure (i.e., fractal)[245] and properties such as radius of gyration, gel fraction, weight average degree of polymerization scale predictably as a function of $|p-p_c|$.[241]

For two-dimensional materials, it is known that the elastic moduli $E$ scales analogous to

$$|p - p_c|^x \sim E \qquad\qquad 4\text{-}24$$

where $x$ is in the order of about 1.2-1.4.[240,241,246] This scaling behavior is a universal relationship and should be independent of the type of network. This has been experimentally confirmed from surface rheology studies of 2D network materials by Veyssie and co-workers,[200,247] and more recently by Rehage.[248,249]

Miyano and Veysié[200] assumed that close to $p_c$, the number of connected bonds is proportional to the total irradiation time so that the shear modulus $\mu$ is related to time $t$ by a relationship similar to Eqn. 4-24

$$\mu \sim (t - t_c)^x \qquad\qquad\qquad 4\text{-}25$$

where $t_c$ is the observed onset of gelation.

     A similar argument is used in the case of the compressibility modulus of OTMS. The log-log plot in Figure 4-17 indicates that $K^s$ follows a scaling behavior similar to a percolating network. At $t_c = 3600$ sec, the average slope of plots obtained over several trials was found to be $0.37 \pm 0.04$.
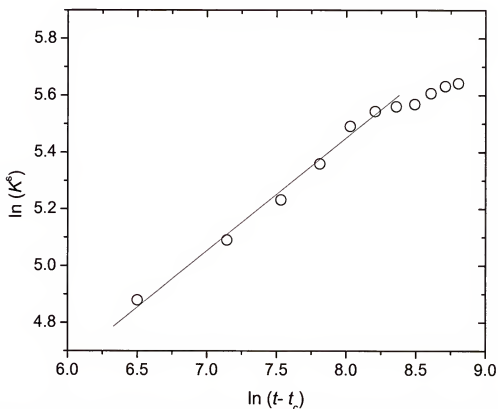


Figure 4-17. Typical scaling behavior of the compressional modulus $K^s$ against $t\text{-}t_c$ for OTMS at pH 3.5 and T = 25°C.

     The low magnitude of the scaling factor compared to the expected value of 1.2-1.3 can be caused by several factors. Rehage[249] cited several of these factors, including relaxation phenomena and the formation of ring structures. There is also the possibility that the "lattice" assumption may not accurately describe the reaction in OTMS since re-

duction of the molecular area during the hydrolysis process can allow lateral mobility, hence, diffusion effects will be significant.

However, in the case of OTMS, the most important factor could be perhaps that $p$ is not proportional to $t$ and that at the gel point a good fraction of the monomers are associated with dangling chains. These dangling chains contribute to the gel fraction but not to the elastic modulus. This is the same argument that de Gennes applied in justifying how the scaling factor of the gel fraction does not vary in the same magnitude as the scaling factor for the elastic modulus, which intuitively should be proportional to the former.[240]

The probability of dangling chains in the OTMS network is not improbable. In fact, because of the tetrahedral geometry at the Si atom it would be impossible for all the three functional groups to be in the same plane with the methylene groups in the alkyl chain in an all-*trans* configuration. This will result in only two of the functional groups to react, the other one being inaccessible and directed towards the subphase (see Figure 4-18a). The final product would then be expected to be a linear polymer, as suggest by Vidon[223] and Sjöblom[224] However, in the presence of a *gauche* defect in the alkyl chain, the silane headgroup can reorient and all three functional groups may get exposed to react (see Figure 4-18b). This possibility can exist at large values of MMA or at low surface pressures where the alkyl chain can have unrestricted movement and can possess *gauche* defects. For these reasons, it is likely that polycondensation reactions leading to the formation of the network occur while the monolayer exists in the *LE* or *mesophase*. Near the end of the reaction, polycondensation reaction only results in the formation of linear chains.
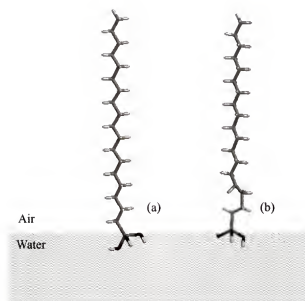
Figure 4-18. Conformation of octadecyltrisilanol at the air-water interface with the alkyl chain in (a) all-trans configuration; (b) gauche defect in the $C_2$ position.

Overall, the value of the ultimate modulus for the polymerized system is consistent with a soft, flexible monolayer material [96] rather than 3D crosslinked silica, which should give a more rigid material. The magnitude of the modulus might be dependent on how defect-free the resulting film is and might be kinetics dependent. Furthermore, it is likely that coagulation of small cross-linked domains may also have a significant contribution

Surface viscosity

Real-time surface viscometry was performed using a flow-trough canal similar to the ones described by Harkins and Kirkwood[160] and Sacchetti[250]. It is the two-dimensional analog the conventional Ostwald viscometer used for bulk fluids.
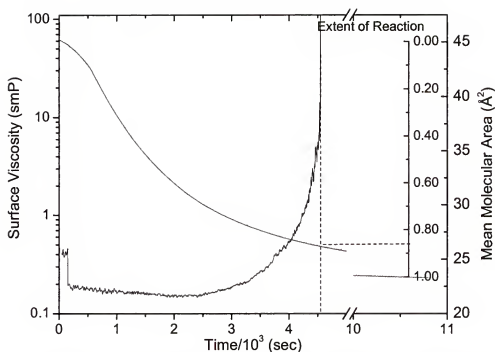
Figure 4-19. Surface viscosity and area relaxation of OTMS in a pH 3.5 subphase during reaction (units of surface viscosity is surface milliPoise, smP = g s$^{-1}$). The ordinate scales at the right side correspond to the isobaric area relaxation curve. From Carino et al. [238]

The surface viscosity profile of the reacting system is shown above in Figure 4-19 overlaid against an isobaric area relaxation curve to show the progress of the reaction as it relates to the viscosity profile.

The initial surface viscosity is consistent with that of small amphiphilic molecules such as stearic acid which was measured at 0.34 smP (see Table 4-3). After the initial compression, a slight initial viscosity drop was reproducibly noted starting at $t\sim200$ sec and may be evidence of the hydrolysis that occurs resulting in replacing methoxy with hydroxy groups.

As the reaction proceeds, viscosity slowly increases and then rapidly diverges. Extrapolation of this vertical segment to the horizontal time axis yields the gelation point, approximately $4.5\pm0.5 \times 10^3$ sec after the reaction was started. This point corresponds to

the same time at which the compressional modulus is increasing. The divergence of the surface viscosity is a manifestation of a possible cross-linking reaction and not just the formation of a linear polymer.[251]

Additional chemical insight is provided assuming that the area change per chemical reaction is constant; the resulting inset scale then gives an approximation of the extent of reaction as monomer converts to products, even though the exact chemical nature of the product is not completely known. The extrapolation of the gel point line corresponds to about 85% of the extent of reaction. The fact that this is significantly above a random 2D percolation threshold and that an initial slow increase precedes the gelation point may indicate that a substantial fraction of the network is made of linear, ladder-like segments with occasional cross-linking.

Table 4-3. Surface viscosity of various monolayer materials.

| Monolayer | Surface Viscosity (smP) | Reference |
|---|---|---|
| Stearic acid, $\pi = 10$ mN/m | 0.15 | Sacchetti[250] |
| Stearic acid | 0.34 | This work |
| n-octadecyltrimethoxysilane, pH 5.6 | 0.24 | This work |
| 1-octadecanol, $\pi = 2$ mN/m | 1.95 | Sacchetti[250] |
| Polyvinyl acetate (DP 16000) | 5.3 | Leblanc[252] |
| Polyvinyl stearate | 19.0 | Leblanc[252] |

Morphology of monolayer film

Brewster angle microscopy offers direct information regarding the morphology of the monolayer at the air-water interface. Here a description of the morphological changes in the monolayer as a function of time will be presented.

Figure 4-21 shows a series of BAM images obtained at various time intervals during an isobaric area relaxation experiment at $\Pi = 8$ mN m$^{-1}$ and pH 3.5. These images were picked from an original series obtained at 5 min intervals. The bright features in the

images indicate the presence of monolayer. These images are unfiltered and the apparent curvature in the images is due to the spherical beam profile of the laser.

Although it is not shown in the series, the very first image captured at $t = 0$ min actually shows a dark field with no features at all. As the reaction proceeds, small bright spots begin to appear. The first frame in Figure 4-21 was taken at $t = 17$ mins and shows the already discernible morphological features of the monolayer with sizes estimated to be less than 10 µm. These bright spots continue to grow into larger spots and form multi-arm irregular domains. The presence of irregular structures (see Figure 4-20) that appear to be incipient dendrites is an indication of anisotropic growth pattern[253] brought about by non-random aggregation.

At approximately $t = 80$ mins, the spots appear to coalesce and form a continuous film. Beyond the point of coalescence, another morphological transition occurs. This time dark spots are observed to form within the film matrix. The first transition occurring at $t = 80$ mins can be an indication of the sol-gel transition in the film. This is in reasonable agreement with the result from surface viscosity and compressional modulus measurements. The transition was observed to occur within a period of 10 mins as could be seen from the sequence of images in Figure 4-22
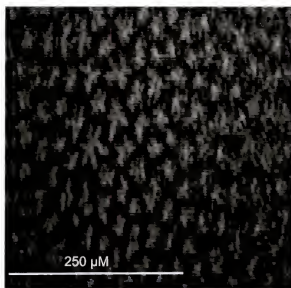
Figure 4-20. A magnified view of the growing domains.
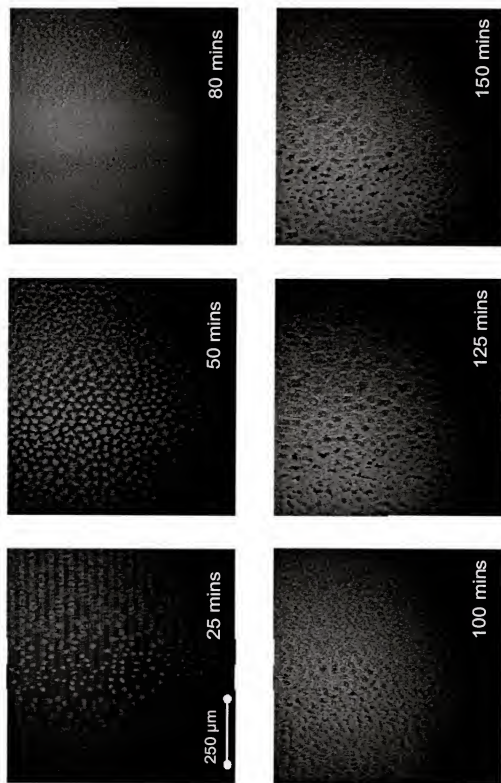
Figure 4-21. Brewster angle microscopy images of a reacting OTMS at pH 3.5 subphase.
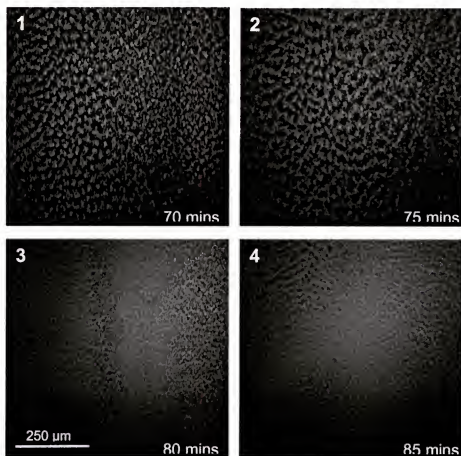
Figure 4-22. Gelation of the OTMS monolayer as observed from BAM images.
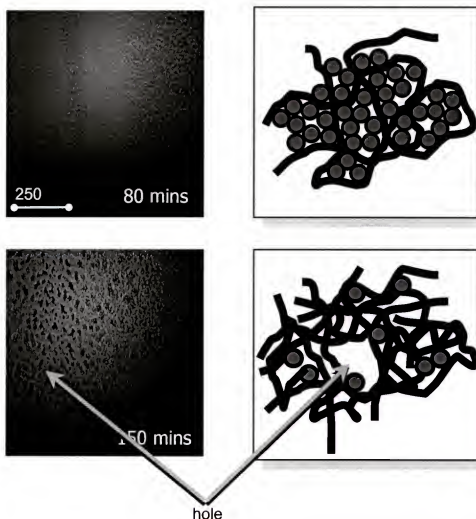
Figure 4-23. A depiction of the formation of holes in the OTMS matrix. The light-colored circles are unreacted monomers trapped within a loose matrix of OTMS network.

Noting that at $t = 80$ mins the MMA is about 85% of the ultimate MMA, the holes appearing in the OTMS matrix can be due to the presence of fully or partially unhydrolyzed OTMS. This is illustrated in Figure 4-23. The top cartoon next to the BAM image at $t = 80$ mins shows monomers trapped within a network of OTMS. These monomers, which are occupying larger molecular areas compared to the final product, are laterally constrained and confined within these 2D cages. As the molecules react further, either by condensation or by hydrolysis, the molecular area they occupy shrinks resulting in the emergence of holes. It is also possible that these holes are manifestation of disordered

phase in the monolayer. The transformation from the ordered to disordered phase during the reaction can be brought about by the disruption of the ordered lattice due to the polymerization that occurs.
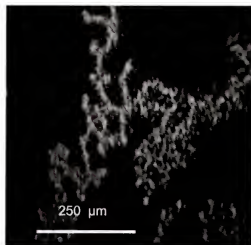


Figure 4-24. BAM image of the resulting product after 3 hrs of reaction time.

After three hrs of reaction time, the monolayer was allowed to expand to $\Pi = 0$ mN m$^{-1}$. Figure 4-24 above shows an image captured approximately 30 mins after the pressure has dropped to zero. This shows that indeed a network has formed but because of overall low cross-linking density, the material appears to separate into linear segments. If the density of junctions is high, it can be expected that an expansion of the film will yield islands of OTMS rather that the dendritic structure shown in the figure.

## Conclusions

Monolayer characterization of OTMS showed that it forms a stable monolayer at the air-water interface. The use of acidic subphase initiates a cross-linking reaction which can be followed by monitoring the surface viscosity and compressional modulus of the film. Due to the complexity of the reaction involved, analysis of the $A(t)$ isobars was limited to the hydrolysis stage only although a full description of the overall kinetics is

greatly desired. The analysis yields a first-order hydrolysis kinetics that shows typical acid-catalysis.

The products of reactions have been shown by both surface viscosity and compressional modulus measurements to be a network material. The products also exhibit scaling behavior typical of network material albeit the density of junctions might be low due to restricted geometry in the silane headgroup. The 2D gelation of OTMS was also followed using Brewster angle microscopy. The observed morphological transition in BAM seems to agree reasonably with results from rheological measurements. Brewster angle microscopy also revealed that the resulting material forms a very loose network.

CHAPTER 5
## STRUCTURAL TRANSFORMATIONS IN POLYMERIZING MONOLAYERS

### Introduction

Alkylsilanes are widely used as components in hybrid materials[254,255] and to modify surface properties. For example, Finnie et al.[1] imprinted hydrophobic alkylsilane patterns on silicon oxide surfaces. Similarly, Zheng et al.[2] have utilized alkoxysilanes as a passivating layer for subsequent patterned assembling of gold nanoparticles. Numerous other groups[256] have studied the formation of alkylsilane thin films on silicon and metal oxide surfaces. Fundamental questions regarding the growth mechanism of these materials persist, in particular, the effect of the cross-linking reaction between individual silane molecules on the quality and molecular architecture of the resulting film. Dutta et al.[3] and several others,[4-6] have observed that silane on $SiO_2$ undergoes island growth as manifested by the invariant film thickness over the duration of deposition. However, several other spectroscopic studies[257,258] indicated homogeneous growth modes, where the film thickness was observed to increase with deposition time. Carraro et al.[7] have shown that these two conflicting mechanisms are actually temperature dependent and may be a consequence of a phase transition taking place in the transient Langmuir monolayer film at the substrate-solution interface. Another possibility, as originally proposed by Sagiv[8] and corroborated by Silberzan et al.,[259] is the hydrolysis and possible cross-linking of the silane while still physisorbed as a Langmuir monolayer onto the hydration layer of the oxide surface. This process is assumed to precede the actual chemical anchoring of the silane functional group to the substrate.[260,261]

The main focus in the study is the dynamics of formation of polyalkylsiloxane from n-octadecyltrimethoxysilane [OTMS, $CH_3(CH_2)_{17}Si(OCH_3)_3$] monolayers at the air-water interface. The primary motivation is to show the feasibility of real-time grazing incidence x-ray diffraction (GIXD) studies with sufficient time-resolution to follow structural changes induced by a moderately fast polymerization reaction. Such investigations should be of relevance to understanding the underlying chemical changes involved. To our knowledge, this is the first time structural evolution and polymerization of a self-assembled monolayer at the air/water interface has been investigated in situ. Advances in synchrotron science and beamline instrumentation at third generation synchrotron sources should make this kind of investigation feasible on a wide variety of surface reactions.

Due to the formation of siloxane bonds from the reactive methoxy substituents, adsorbed OTMS molecules can be laterally constrained from moving at the surface. This assertion was supported by atomic force microscopy studies of self-assembled monolayers which showed a larger degree of disorder at higher temperatures, where the chemical reactivity is enhanced.[262]   In such cases, the resulting molecular ordering is more glass-like than crystalline as cross-linking interferes with the in-plane reorganization of the monolayer following deposition.

As a Langmuir monolayer, polymerization of the OTMS monolayer can be readily controlled by pH and surface concentration.[222,223] Since the water interface is amorphous and lacks surface groups capable of forming directional chemical bonds, no substrate-induced in-plane positional ordering should occur. In this case, positional order is totally dependent on the intrinsic molecular packing induced by non-covalent interaction between the aliphatic chains and the polymerization of the headgroups of OTMS.

Experimental

<u>General</u>

Monolayers were spread from solutions containing approximately 1 mg/mL of OTMS (95%, Gelest) dissolved in chloroform (Fisher). The OTMS sample was kept in a cold storage and was used as purchased. The deionized water (Fisherbrand, Fisher) was further purified using an Ultrapure MilliQ system with a resulting resistivity of >18 MΩ-cm. The pH was adjusted using HCl (Fisherbrand, Fisher) and measured using a glass-electrode attached to a Accumet pH meter (Fisher). Between each experiment, the trough was drained of the subphase and wiped with cleaning tissues soaked in 95% ethanol (ACS Grade). The trough was then rinsed twice with purified water before use. The surface pressure of the monolayer was determined using a Wilhelmy plate technique.

Compounds used for powder x-ray diffractions were prepared from silane compounds obtained from Gelest and used without further purification. About 1 ml of the silanes was added drop by drop to a 0.1 M HCl solution. The resulting whitish suspension was left overnight to react. The next day, the suspension was filtered and the precipitate was washed with ethanol and then with copious amounts of purified water to remove any residual acid. The precipitate was then placed in vacuum and left to dry. To prepare samples for x-ray diffraction, a small amount of the dry powder was placed in between two adhesive tapes. This "taped" sample was then mounted in front of the x-ray source. This was found to be convenient as well as effective sample preparation for transmission x-ray diffraction. Subsequent background subtraction removes the broad scattering caused by the adhesive tape.

Grazing incidence x-ray diffraction experiments were performed at the surface of a Langmuir trough aligned to a high-brilliance x-ray beam of the MRCAT undulator at

the Advanced Photon Source (APS) synchrotron at Argonne National Laboratories (Argonne, IL). The incident x-ray beam was tuned either at 11.0 keV ($\lambda$ = 1.13 Å) or 10.0 keV ($\lambda$ = 1.24 Å). To achieve surface sensitivity, the angle of incidence was kept below the critical angle of total external reflection which can be calculated from Eqns. 3-14 and 3-15:

$$\alpha_c = \cos^{-1}\left(1 - \frac{\lambda^2 \rho r_o}{2\pi}\right) \qquad 5\text{-}1$$

This yields the angles of 2.0 at and 2.2 at 11 keV and 10 keV, respectively

Beamline Instrumentations

The beamline at the Materials Research Collaborative Team (MRCAT) is designed[263] for a variety of experiments ranging from transmission and fluorescence X-ray absorption fine structure (XAFS) to scattering and diffraction in liquids, powders and bulk solids. The beamline consists of two main sections (see Figure 5-1). The first section (the "A" hutch) located about 20 m from the source houses filters, a collimator, the monochromator systems and shutter/beamstop assemblies. The second section located about 30 m further downstream is the experimental station (the "B" hutch), connected to the "A" hutch by a 24 m long flight path maintained under high vacuum.

In the first section, the X-ray beam coming off the 10-ID undulator beamline is passed through a Bremsstahlung collimator and then reflected to a double Si(111) crystal monochromator.[263] The monochromator system was designed and constructed by a group from the Illinois Institute of Technology. It has a cryo-cooled first crystal and a second crystal maintained in thermal equilibrium with the enclosure. The second crystal is connected to servomotors that allow the crystal to rotate, as well as allowing Bragg-normal translation. The second crystal is also attached to piezoelectric actuator controlled by an

AC feedback circuit to maintain the peak intensity. The feedback circuit gets its input from an ion-chamber detector located close to the beryllium window where the beam exits in the "B" hutch.

In the "B" hutch section (or Experimental Section), is the 60-cm flat, vertically deflecting harmonic rejection mirror. The mirror has a maximum surface roughness of 3 Å and has platinum and rhodium stripes running parallel along its principal axis. The stripes have been deposited on a quartz slab and are used depending on the energy desired for the experiment. Usually, GIXD experiments were done at or below 11 KeV and the platinum stripe is therefore used since platinum has an absorption edge at 11.56 KeV. The rhodium stripe can allow higher energy, up to its absorption edge at about 23 KeV. The mirror is enclosed in an inert atmosphere of helium and mounted on a platform that allows it to be translated vertically and horizontally with respect to the beam. A pin on a servo motor mounted at the downstream end of the mirror controls its tilt.
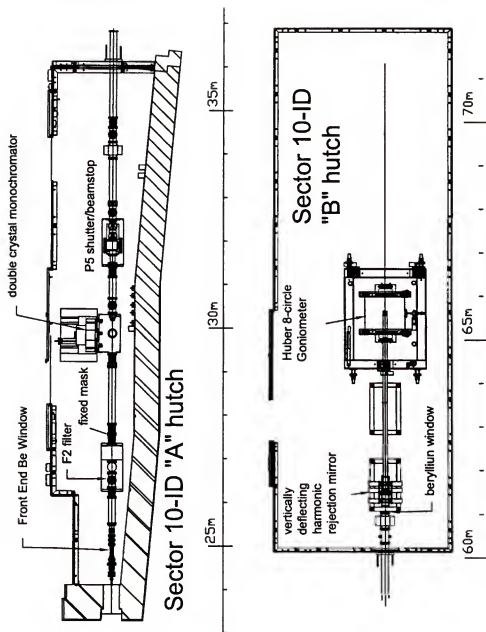
Figure 5-1. Layout of the Sector 10-ID at the MRCAT facility, Advanced Photon Source, Argonne National Laboratory. From Segre.[263] The bar under the drawings indicates the distance from the undulator source.
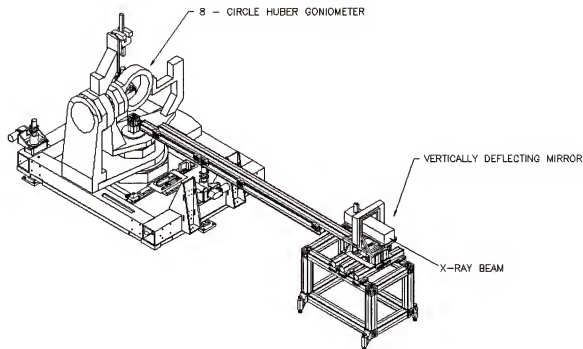
Figure 5-2. The 8-circle goniometer at the Materials Research Collaborative Access Team at the Argonne National Laboratory. Courtesy of MRCAT.

Figure 5-2 above shows the 8-circle Huber goniometer (Huber Diffraktionstechnik GmbH, Germany) located three meters downstream from the mirror. It is mounted on a heavy translation and lift table that can move the goniometer on top of it in the three Cartesian coordinates. All optical components are supported on a standardized X95 rail system for high rigidity and stability.

Grazing Incidence X-ray Diffraction

To achieve surface sensitivity of the x-ray diffraction, the incoming angle was kept below the critical angle for total external reflection (~2.0 mrad for air-water at this energy). In this "grazing incidence" mode, x-rays do not penetrate into the bulk sample but propagate as evanescent waves along the surface with a penetration depth of few nanometers at most.[180] This drastically improves the ratio of surface scattering to bulk background scattering originating from the subphase.

The schematic diagram in Figure 5-5 shows the set-up of the x-ray diffraction experiment performed at the 10-ID beamline, operated by the Materials Research Collaborative Access Team (MRCAT).

The most important components of the x-ray diffraction setup are described as follows. Inside the experimental station, a mirror **M1** with a Pt stripe provides harmonic rejection. A second Pt mirror, **M2**, deflects the beam further downward to tune the angle of incidence suitable for grazing reflection, approximately 1.5 mrad. A series of motorized slits were used to define the beam and eliminate background scattering. The intensity of the incident beam, $I_o$, was monitored using an ion chamber detector **D1**. The diffracted beam, normalized to $I_o$, was measured by a NaI scintilation detector. The detector resolution is defined by a set of vertical Soller slits and was calculated to be 0.15 nm$^{-1}$, sufficient to resolve the peaks observed in this study that have a typical FWHM of approximately 0.5 nm$^{-1}$. One particular problem with the use of a Soller slit array is that it should be perfectly aligned to the beam to be able to obtain maximum intensity. This difficulty led to a decision to change the optical design and use a pair of conventional slits of comparable resolution instead.

<u>Beam Alignment</u>

Alignment procedure discussed here only applies for the optics in the Experimental hutch. Prior to the alignment of the GIXD optics, it is assumed that the x-ray beam had been adjusted to the optimized setting. This is done by adjusting the optics in the "A" hutch. In addition, mirror **M1** is also assumed to have been moved so that the incoming beam is incident on the Pt strip to reject the higher harmonic emissions.

The alignment of the x-ray optics is excruciatingly difficult especially for inexperienced users. What makes the whole process difficult is the fact that the beamline can be

configured for several different experiments with different optical system requirements. Grazing incidence x-ray diffraction itself demands unparalleled precision in the alignment process relative to other x-ray scattering techniques.
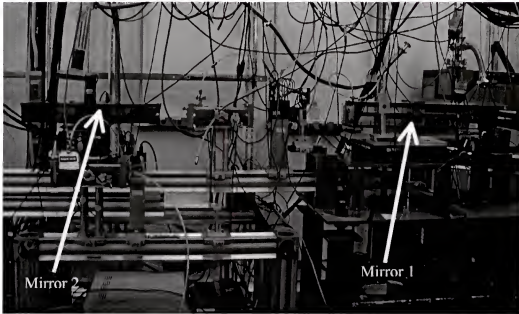


Figure 5-3. Locations of the mirrors upstream of the Huber goniometer inside the Experimental Station.

The process of beam alignment starts sequentially upstream at the first mirror then down to the detector that is mounted on one of the arms of the goniometer. Without the second mirror **M2**(see Figure 5-5) mounted on the rail, the beam coming off from the flight path from Hutch "A" is deflected downward on one of the reflective metal strips on mirror **M1**. The mirror is spring loaded on one end so that moving a pin up and down (using motor **Mirror1**, see Table A-1 for the motor nomenclatures) on the other end can change the inclination of the mirror with respect to the horizontal. It might also be necessary to move the mirror upward or downward so that it is aligned vertically with the beam.

Following a brief exposure of a piece of burn paper to the x-ray beam, the angle of the deflected beam to the incident beam can be determined by measuring the distance between two burn spots, i.e.

$$\alpha \approx \frac{l}{d} \text{ radians for } l << d \qquad \qquad 5\text{-}2$$

where $l$ is the distance between the burn spots of the deflected beam and the incident beam; and $d$ is the distance from the end of the mirror to the position where the burn was taken (see Figure 5-4). To achieve adequate accuracy of the angle measurement, the burn paper should be at least a meter away from **M1**. This usually results in the burn spots to be about 1 cm apart. At this point the deflected beam should have an angle $\alpha_{m1}$ approximately 11-14 mrad off the horizontal.
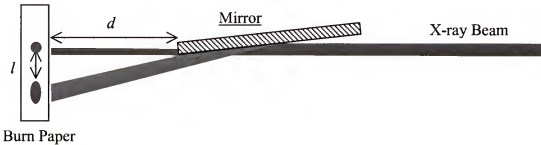


Figure 5-4. Measurement of angle between the incident beam and the reflected beam.
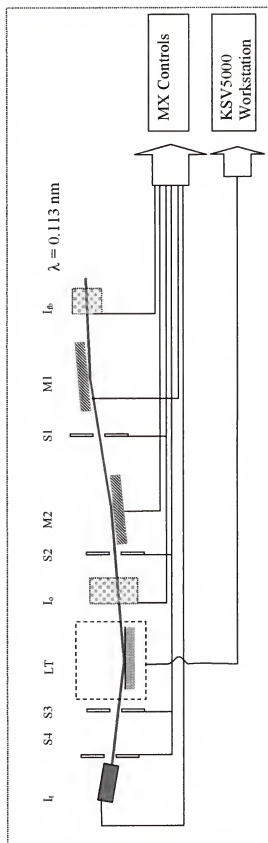
Figure 5-5. Experimental setup for the grazing-angle x-ray diffraction. S1, S2, S3, S4 = slits M1, M2 = platinum mirrors; D1 = ion-chamber detector; D2 = NaI scintillation detector; LT = Langmuir trough system. From Carino et al.[264]

Using the appropriate motors, the blades of the slit **S1** are adjusted so that the spill over of the main beam coming off the **M1** is blocked and only the deflected beam is allowed. All along, measurements of beam intensity are done by an ion-chamber detector. To confirm for the beam position at any point during the alignment procedure, a burn is taken using the burn paper. Alternatively, the x-ray beam can be located by a watching the glow off a fluorescent screen using several cameras that are strategically located inside the hutch and that are hooked up to a TV monitor at the control station.

The next step is then to mount the mirror **M2** on the stage located about 1 m downstream from **M1**. The stage is similarly designed to be translated across the beam and in the vertical direction to get it aligned to the beam. To align the mirror parallel to the beam the following procedure is followed. First, the mirror is adjusted to be roughly on the horizontal and vertically offset off the beam path. The intensity of the $1^{st}$ reflected beam is then measured and recorded. The mirror is then moved vertically so that the beam is completely blocked. Then the mirror is rocked using motor **Mirror3** until the intensity is half of the intensity of the unblocked beam. When this is done, the mirror is now parallel to the beam. By adjusting the tilt of this mirror, the angle of incidence can be set to the desired value which should be about 85% of the critical angle for total external reflection. The x-ray incident angle measurement follows the same procedure as the alignment in **M1**. However, in this case the measurement has to be more accurate since this will determine the actual grazing angle off the water surface. Accuracy can be achieved by placing the burn paper further downstream.

Once the two mirrors have been aligned and the slits adjusted to block any spill over of the primary beam, the Huber diffractometer can now be aligned so that it is cen-

tered to the beam. Shibata[265] has outlined the procedure and is summarized as follows. A mini-goniometer with a needle is mounted on the phi motor of the diffractometer. The crosswire on the telescope is then centered on the tip of the needle by translating and rotating the stage of the mini-goniometer. At the end of this exercise, the tip of the needle would be at the crosswire and at the center of rotation of the Huber. To center the beam to the center of rotation of the Huber, a piece of burn paper is placed at the tip of the needle and the spot where the burn spot appear is observed. If the burn spot does not coincide with the tip of the needle, the whole goniometer is moved by translating the Huber table vertically and horizontally.

The alignment of the detector arm to coincide with $k_{xy} = 0$, a horizontal scan of the arm coupled to the motor *hnu* is done. The value of *hnu* at which the intensity is maximum is set as $k_{xy} = 0$. A similar procedure is done on the arm that moves in the vertical direction: the value of *hdelta* at maximum intensity is set as $k_z = 0$.

Table 5-1. Positions of the first 10 diffraction peaks from SRM 660a using x-ray radiation equivalent to Cu K$\alpha$ ($\lambda = 0.1541$ nm) and the calculated $k_{xy}$. From NIST SRM 660a certification.[266]

| Peak No. | *hkl* | 2θ, Cu Kα | $k_{xy}$ |
|---|---|---|---|
| 1 | 100 | 21.3578 | 18.78 |
| 2 | 110 | 30.3847 | 26.56 |
| 3 | 111 | 37.4417 | 32.53 |
| 4 | 200 | 43.5064 | 37.56 |
| 5 | 210 | 48.9573 | 41.99 |
| 6 | 211 | 53.9886 | 46.00 |
| 7 | 220 | 63.2182 | 53.12 |
| 8 | 300 | 67.5474 | 56.34 |
| 9 | 310 | 71.7452 | 59.39 |
| 10 | 311 | 75.8438 | 62.29 |

At this point, the goniometer is now fully aligned and ready for calibration. The standard used for calibration was NIST Standard Reference Material (SRM) 660a (Na-

tional Institute of Standards and Technology). Certified SRM 660a is lanthanum hexaboride ($LaB_6$) powder intended for use as line position and line shape standard for diffraction.[266] If the goniometer is properly aligned, the peaks found in Table 5-1 can be obtained.

Langmuir Trough System

The Langmuir trough system was jointly designed by the Florida group.[267] and KSV Inc., Finland, to fit in the center of the 8-circle Huber goniometer of the MRCAT beamline. The trough measures 7.36 cm x 42.55 cm and about 1 cm in depth. A remote controlled integrated vertical actuator allows the alignment of the liquid surface with the x-ray beam, such that maximizing the intensity of the reflected beam was conveniently achieved. The trough also features an adjustable barrier lateral tilt angle, symmetric compression geometry, and barrier drive components well beneath the water surface to maximize usefully available interfacial surface for scattering spectroscopy and diffraction studies. The entire instrument is mounted within the *chi* circle (see Figure 5-6) of the goniometer and fixed to an active vibration isolation table (MOD-1, Halcyonics, Germany). Later experiments would require that the trough be mounted in front of the *chi* circle (see Figure 5-7) instead of mounting it on the top to do away taking out the *phi* motor.

To prevent possible x-ray-induced damage on the monolayer and to minimize the background scattering from air, the trough and all of its mechanical components were enclosed in a plexiglass box with Kapton-covered windows. Also, a continuous stream of helium gas is flushed through the plexiglass enclosure.
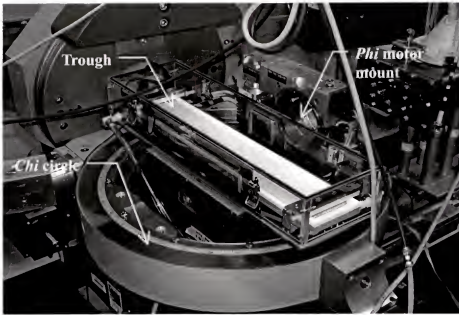
Figure 5-6. The Langmuir trough is mounted on top of the *chi* circle. The *phi* motor was taken out from its mount to let the beam pass through.
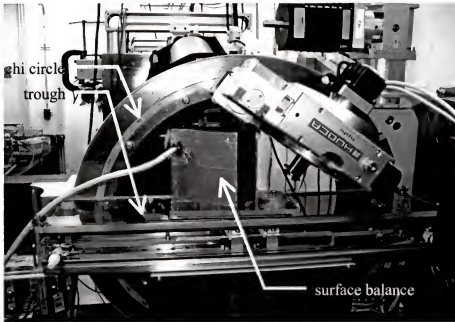


Figure 5-7. Modified Langmuir trough setup used in later experiments.

Data Collection and Analysis

Control and data acquisition at the MRCAT are done using MX, a customized beamline control software running under Debian Linux and designed by Lavender.[268] MX

controls all the motors, including those in the 8-circle goniometer, X-Y translation stage, mirrors, and sets of slits. In addition, it acquires the data from all the scalers attached to the various detectors being used. The software is highly configurable and allowed quick modification of data acquisition routines. Thus, for example, a quickscan routine describer later was successfully implemented to enable real-time diffraction at the MRCAT.

Data obtained from diffraction experiments are obtained as text-formatted files. These data files can easily be imported in scientific data analysis software such as Origin® (OriginLab Corp). For convenience, however, the files are first converted to a format where the detector angle position is converted to appropriate values of $k$. Once the data is imported into Origin®, the background signal is manually subtracted then pure Lorentzian function fitting is done.

For kinetics datasets, the time stamp of the file was used as the reference time frame. This would mean that the time $t$ in the kinetics run would be actually be the time at which the scan was completed.

<u>X-ray Powder Diffraction</u>

Wide-angle x-ray diffraction was obtained from a Siemens Platform diffractometer with a Hi-Star GADDS (General Area Diffraction System) using a Cu K$\alpha$ source ($\lambda = 1.542$ Å). The detector was positioned at around 60 cm from the sample. The calibration of the angle and detector distance was done using a fine corundum powder placed in a capillary or sandwiched between transparent adhesive tapes. The generator was operated at 50 kV and 40 mA and data was collected for at least 1 hour. After the data acquisition, the image was unwarped and the plot of 2$\theta$ against intensity were obtained by integration along the chi ($\chi$) direction.

Results and Discussion

Grazing Incidence Diffraction of Reacted OTMS Monolayer

Solution of OTMS monolayer was spread on the water surface and compressed to 8 mN m$^{-1}$. At this surface pressure, the monolayer has an initial average molecular area of 43.5 ± 0.7 Å$^2$ and corresponds to the liquid expanded phase. With time, the average molecular area has decreased (see Figure 5-18) to 21 ± 2 Å$^2$, a value that is close to within experimental error to the final average molecular area of 20 Å$^2$ reported by Fontaine et al.[269] At pH 1.5, OTMS rapidly undergoes hydrolysis and condensation such that the reactions are essentially complete in 1.5 hour.[269]

For the initial GIXD measurement, OTMS was spread on a pH 1.5 subphase and allowed to react. Approximately 2 hrs later, a diffraction measurement was done. A peak was detected with a full width at half maximum (FWHM) of 0.51 ± 0.12 nm$^{-1}$ centered at $k_{xy}$ = 15.48 ± 0.04 nm$^{-1}$ (see Figure 5-9), determined after background subtraction and fitting a Lorentzian function by nonlinear least squares algorithm to the data. If this peak is assigned to reflection {10}, the second-order diffraction peak corresponding to {1$\bar{1}$} should appear at $\sqrt{3}\, k_{xy}$ or 27 nm$^{-1}$. Further scans toward higher $k_{xy}$ did not yield any other peaks that can be assigned to higher reflection orders. It is however possible that instrumental limitation is responsible for the non-detection of higher-order peaks since they are expected to be considerably less intense in the first place.

A peak appearing around 16.7 nm$^{-1}$ has such a low intensity, barely rising above the background noise that it can be considered as insignificant.

If the single diffraction peak is assigned as the triply degenerate {10} + {01} + {1$\bar{1}$} peak for hexagonally packed lattice, the Bragg $d$-spacing can be calculated using

$$d = \frac{2\pi}{k_{xy}} \qquad\qquad 5\text{-}3$$

and the lattice spacing $a$ from

$$\frac{1}{d_{10}^2} = \frac{4}{3}\left(\frac{h^2 + hk + k^2}{a^2}\right) \qquad\qquad 5\text{-}4$$

$$a = \left(\frac{2}{\sqrt{3}}\right)d_{10} \qquad\qquad 5\text{-}5$$

yielding $4.06 \pm 0.02$ Å and $4.69 \pm 0.03$ Å, respectively. These values are characteristic for close-packing of alkyl chains[270] albeit deviating a small amount from the previously reported value of $4.76 \pm 0.02$ Å$^2$ for this system.[269]
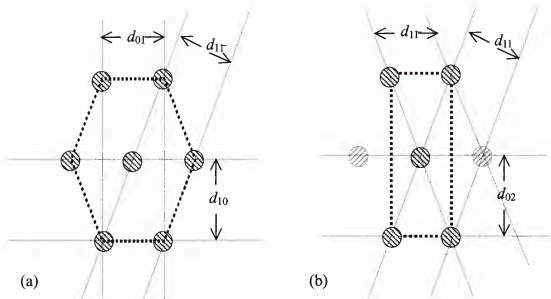


Figure 5-8. (a) Periodicity and Bragg spacing in a distorted 2D hexagonal lattice. In the ideal, non-distorted hexagonal lattice, all the spacings are equivalent, hence the {10} + {01} + {1$\bar{1}$} reflections are degenerate; (b) alternative equivalent lattice indexation using a centered rectangular cell. From Daillant[271]

Assuming exponential decay of positional correlation with increasing separation, i.e., $e^{-r/\xi}$, the positional correlation length $\xi$ can be estimated from

$$\xi = \frac{2}{FWHM(k_{xy})} \qquad\qquad 5\text{-}6$$

which yields 3.9 ± 0.1 nm for the uncorrected FWHM. In comparison, small amphiphiles such as fatty acids are known to have correlation length in the range of 10 nm[67,270,272] and 500 nm, in the case of phospholipids.[273]
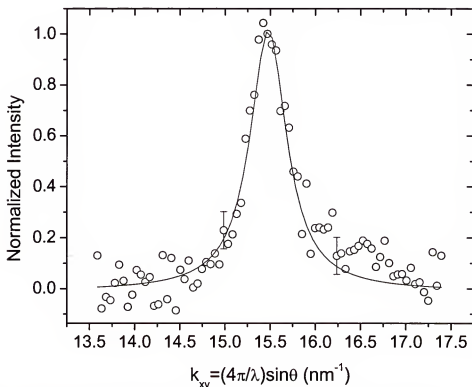


Figure 5-9. First order peak detected from an OTMS Langmuir monolayer.

Comparison with Bulk Silanes

Wide-angle x-ray powder diffraction curves of reacted and dried silanes are shown in Figure 5-10. Table 5-2 shows a summary of the data obtained primarily by fitting a Lorentzian fit to the data. These silanes all have the same number of methylene groups in the alkyl chain with the exception of compound **B** which contains quaternary amine and an extra propyl moiety in the alkyl chain. Compounds **A**, **C** and **D** only differ in the number of methyl substitution in the silane head group having three, two and one methyl groups,

respectively. Compound **C** is diethoxy substituted but it should not influence the ultimate

packing of the molecules since the ethoxy group is eliminated during the hydrolysis reac-

tion.

Table 5-2. Data obtained from Lorentzian function on the diffraction curves in Figure 5-
10. The peaks are described as weak(w), medium(m), strong(s), and very strong(vs)
based from their relative intensities.

| Silane | $2\theta$ $\lambda=1.542$ Å | $k$ nm$^{-1}$ | $d$-spacing Å |
|---|---|---|---|
| (A) n-octadecyltrimethoxysilane | 3.28(w) | 2.33 | 26.97 |
| | 5.11(w) | 3.63 | 17.30 |
| | 21.28(vs) | 15.05 | 4.17 |
| (B) octadecyl-(3-trimethoxysilylpropyl)-ammonium chloride | 2.45(w) | 1.74 | 36.11 |
| | 4.97(m) | 3.53 | 17.80 |
| | 21.38(s) | 15.12 | 4.16 |
| (C) n-octadecylmethyldiethoxysilane | 21.44(vs) | 15.16 | 4.14 |
| (D) n-octadecyldimethylmethoxysilane | 18.16(vs) | 12.86 | 4.89 |
| | 21.68(vs) | 15.33 | 4.10 |
| | 23.20(vs) | 16.39 | 3.83 |

The bulk OTMS shows a strong peak at 21.28° and minor peaks at 5.11° and

3.28°. Applying Braggs' law, these $2\theta$ values correspond to $d$ spacings of 4.17 Å,

17.30 Å and 26.97 Å, respectively. The former agrees with the chain-chain packing meas-

ured from GIXD of OTMS monolayer in this study and those reported by Tippman-

Krayer[270]. The other peaks close to the small-angle region indicate the tendency of this

compound to self-assembly and form lamellar structures, although weak judging from the

intensity of the peak. The peak corresponding to $d = 26.97$ Å matches with the expected

length of 26-27 Å obtained from molecular models of a fully-extended OTMS molecule.

The $d$-spacing of 17.30 Å is difficult to assign in the absence of other supporting data.

However, Parikh [221] reported a head-to-head bilayer structure of this compound, which

yields                                                                                    a

123



Figure 5-10. X-ray diffraction spectra of selected alkoxysilanes.

primary reflection with $d$ = 52.4 Å. In this case, the $d$-spacing corresponding the third-order or (003) peak should appear at around the location of the second peak in Figure 5-10A. The only other silane that showed lamellar structure is Compound **B**. It exhibited a strong peak located at 2.45° and a minor peak at 4.97°. Judging from resulting $d$-spacing, the second peak is apparently a second-order reflection originating from the same structure feature that yields the peak at 2.45°. This strong manifestation of a lamellar structure is most likely due to the strong hydrophilic character of the quaternary amine moiety. Compound **C** did not show evidence of any lamellar structure

In general, all these silanes showed the typical alkane chain closed-packing with $d$ spacings around 4.14 - 4.17. Even compound **C** which has a methyl substitution at the headgroup surprisingly exhibited chain-chain packing very close to that of OTMS. Apparently, the presence of the methyl group at the silane headgroup does not distort the crystal lattice very much. The presence of two methyl groups in Compound **D**, however, ruins the hexagonal lattice observed in the other silanes. It now appears to be a triclinic with the alkyl chains tilted at an arbitrary direction.

Compression-Induced Ordering in Unreacted Monomer

A solution of OTMS was spread on neutral water (pH ~5.5) at 25°C and a compression of the monolayer was initiated in a step-wise manner. Each step was made to correspond to surface pressures along the isotherm shown in Figure 5-11a. Diffraction was initiated when the surface pressure was $\Pi$ = 9 mN m$^{-1}$ and every 1 mN m$^{-1}$ thereafter. Resulting diffraction curves are shown in Figure 5-11b with Lorentzian fits and the background already subtracted.

As shown in Figure 5-11b, the region with mean molecular area (MMA) ranging

from 80 Å$^2$ to 40 Å$^2$ is an isotropic liquid phase with no detectable structure. The first

evidence of an emerging structure was detected at $\Pi$=15 mN m$^{-1}$ with MMA in the range

of 30 Å$^2$. On further compression towards smaller MMA, the peak grows steadily against

the applied surface pressure then rising steeply as $\Pi$ = 21 mN m$^{-1}$ (see Figures 5-12 and

5-13).
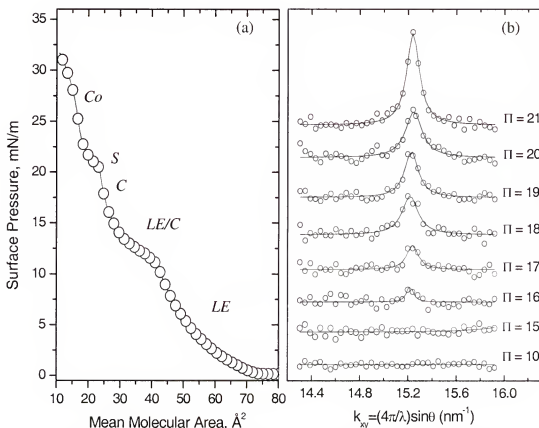


Figure 5-11. (a) $\Pi$-A isotherm of OTMS on pH 5.5 subphase at 25°C; (b) Diffraction spectra obtained at various pressures along the isotherm in (A). Diffraction curves for $\Pi$ < 10 mN m$^{-1}$ are not shown.
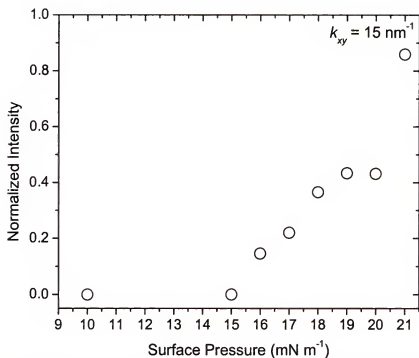
Figure 5-12. Diffraction intensities of peak at about $k_{xy}$ = 15 nm$^{-1}$ plotted against surface pressure.
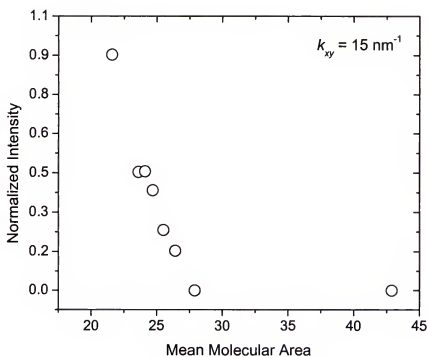


Figure 5-13. Diffraction intensities plotted against mean molecular area.

The increase in scattering intensity with rising surface pressure is usually attributed to the favorable increase in population of molecules in the *trans* conformation. This conformational transformation of amphiphiles has been suggested by previous x-ray studies[274] and confirmed by reflection-absorption Fourier transform infrared spectroscopy (RAFTIR) experiments done on pentadecanoic acid.[275] In the latter study, a disordered conformation with a large number of gauche bands was proposed for the monolayer in the liquid expanded (*LE*) region, while in the condensed phases (*C and S*) chains were highly ordered with trans bonds mostly. This information was obtained mainly from the analysis of the C-H stretching vibrations. A similar experiment using polarized modulated external infrared reflection absorption spectroscopy (PM-IRRAS)[276] also showed a similar transformation from *gauche* → *trans* as the monolayer undergoes liquid → solid phase transformation as the temperature is reduced.
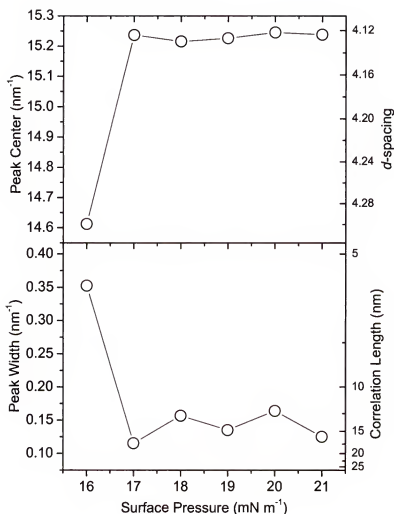
Figure 5-14. Peak center of the first order peak (Top) and the corresponding peak widths as determined from the Lorentzian fit (Bottom). At the right *y*-axes of both graphs are the calculated Bragg *d*-spacing (Top) and the positional correlation length (Bottom).

Figure 5-14 shows the calculated FWHM and location of the peak, two distinct attributes relevant to molecular organization and packing. At the lowest pressure where the first diffraction peak was observed, the molecules have a wider *d*-spacing and low positional correlation. As the pressure is increased, the *d*-spacing is reduced and the positional correlation has increased. This observation would imply that the molecules initially form loose organized domains that are squeezed together as the pressure is increased. In

the same process of compression, these domains increase in size as reflected from the increase in the positional correlation. One interesting observation regarding the positional correlation of the molecules is that once the condensed phase has formed, it appears that the organized domain size becomes limited to some finite value and that further compression does not alter their size.

At $\Pi = 21$ mN m$^{-1}$, a scan towards higher $k_{xy}$ was done and the resulting diffraction curve is shown in Figure 5-15. Unlike the one obtained for OTMS spread over pH 1.5 subphase, the monolayer in this case showed a broad peak at around 26 nm$^{-1}$ (see inset in Figure 5-15). This would actually closely match the second-order {11} peak expected for a structure with a first order {10} at $k_{xy} = 15.24$ nm$^{-1}$.
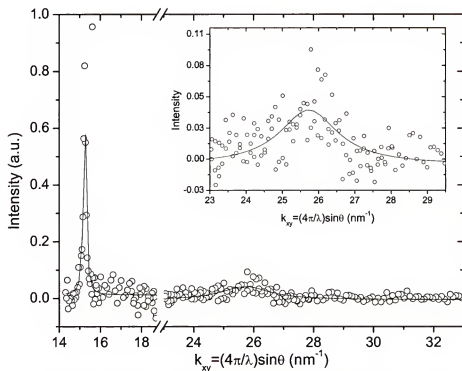


Figure 5-15. GIX diffraction spectra of OTMS at $\Pi = 21$ mN m$^{-1}$. Inset is an expanded view of the 23-29 nm$^{-1}$ region. The intensities are not corrected for Lorentzian polarization.

The appearance of an additional peak at $k_{xy} = 26$ nm$^{-1}$ implies the lifting of the degeneracy of the first order peak and that the lattice is actually distorted from the ideal hexagonal structure. This is not at all unexpected since the OTMS hydrolysis reaction at pH 5.5 is slow and that the monolayer is predominantly consists of alkyltrialkoxysilanes with the headgroup occupying a larger cross-sectional area than the tailgroup (see Figure 5-16). To compensate for the large headgroup, the molecules are tilted since the packing is now determined by the space requirements of the headgroup rather than the alkyl chain. This has been similarly observed in fatty acids with chain branching at the 2-position.[277]
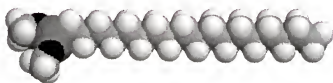


Figure 5-16. Space-filling molecular model of an OTMS molecule showing the relative cross sections of the tail and headgroup.

<u>Insights on the Kinetics of Self-Organization and Film Formation</u>

Since the first reported GIXD at the air-water interface by Dutta et al.[27] and Kjaer et al.[28], the focus of most synchrotron studies of monolayers have been generally about *in situ* investigations of the effect of compression and temperature on the structures and phases. Very little has been cited in the literature regarding x-ray studies of time-dependent effects in floating monolayers. Obviously, the main problem is the weakness of the scattered signal and the demand for high-intensity sources so that the data acquisition can be done in the required time and at an adequate resolution.

Dynamics in Langmuir-Blodgett films, on the other hand, are studied more routinely since these are usually prepared as multilayers and so the scattering cross-section would be several times greater. For example, Rapp investigated the multilayer spacing and total film thickness of a 28-monolayer thick film of magnesium stearate as it is heated with a time resolution of 10 seconds.[278] Using a multiple imaging-plate (IP) detector system and focusing monochromator, Foran was able to achieve signal-to-noise ratio far higher than the conventional scanning method.[279,280] Their instrumental innovation allowed them to do a time-resolved grazing-incidence diffraction studies of metal fatty acids at a shorter time.[281]

In the case of Langmuir films, the scattering cross-section from the monolayer-thick film is reduced drastically such that a typical scan usually lasts anywhere from 20 mins to 1 hr, depending on the desired resolution. This limits significantly the type of time-resolved studies to dynamic systems that take hours to complete or reach equilibrium. Fortunately, certain reactions in monolayers have this characteristic kinetics. For instance, the photoisomerization in certain azobenzene surfactants can take up to 1000 sec (at $\Pi = 14$ mN m$^{-1}$) to reach completion.[282] Similarly, the UV-induced condensation reaction in dilinoleoylphosphatidylethanolamine monolayers occurs equally slowly.[283] These systems are good candidates where real-time GIXD can be used to investigate the structural transformations occurring during the reaction.

Dynamics in monolayers can also involve other processes. Previously, Lin et al. investigated the time-dependent effects that are observed as amphiphiles are compressed. They have identified for the first time that a microscopic relaxation mechanism occurs as

the monolayer reorganizes from a pseudohexagonal structure, formed upon compression, to an undistorted hexagonal structure.[284]

<u>Real-time Grazing Incidence X-ray Diffraction</u>

The series of experiments that will be discussed hereafter was designed to exploit and further improve the GIXD technique as a method of investigating the structural transformation in real-time. The alkoxysilane system provides an excellent platform in which these goals can be achieved since its chemistry is very easily controlled by subphase pH and surface concentration.

Initial experiments were done at constant pressure of $\Pi = 8$ mN m$^{-1}$, T=27°C and subphase pH=4.0 where the reaction is sufficiently slow to be followed by conventional diffraction scans. Unlike the earlier described GIXD experiments, scanning of the detector was commenced as soon as the monolayer was spread. The "dead time" between monolayer formation to getting the hutch evacuated and having the controls started is about two minutes. This is appropriately accounted for in the calculation of the scan time.

Once the first scan was done, the subsequent scans were started automatically and repeated until intensity reached an asymptotic value. This was easily achieved by running a command script at the control workstation. For each complete scan, a file is generated and its time stamp is used as the reference time frame for that run. This might appear an imperfect approach especially for kinetic runs in which single scans takes time to complete. This, however, is the best systematic approach applicable in this case.

Initially, there is no evidence of order, as represented by the absence of x-ray scattering peaks in the first 100 mins. The onset of ordering is manifested by the appearance of a fairly symmetrical peak observed at $k_{xy} = 15.24$ nm$^{-1}$, becoming resolvable at an av-

erage macroscopic molecular area of 32.6 ± 2.3 Å$^2$ as shown in the isobaric area relaxation curve in Figure 5-18. This peak grows in intensity, leveling off at reaction times consistent with the end of the reaction as measured by isobaric area change.
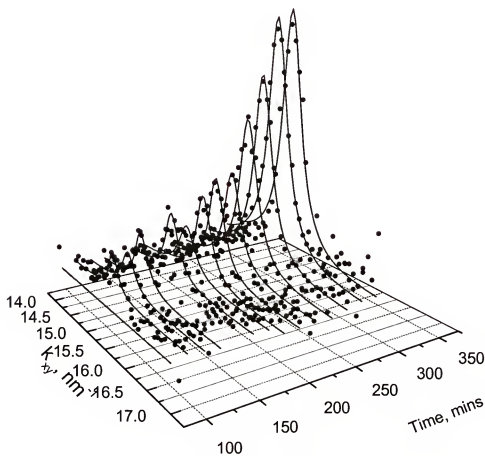


Figure 5-17. Real-time x-ray diffraction peaks of the reacting OTMS system at pH 4.0 subphase. From Carino et al.[264]
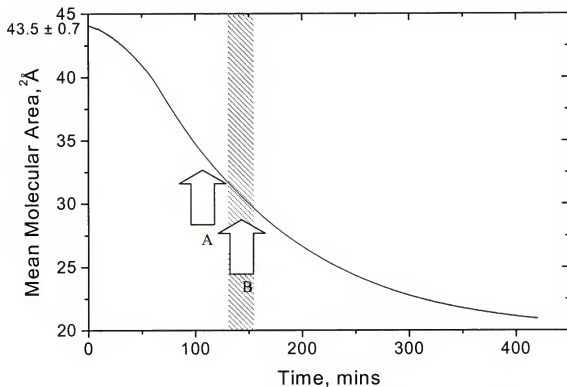
Figure 5-18. Area relaxation of OTMS in pH 4 subphase and $\Pi = 8$ mN m$^{-1}$ and T = 25°C. Arrow **A** points to the onset of the diffraction peak; arrow **B** indicates the window of gelation time from 2D viscometry. From Carino et al.[264]

The chemically interesting feature of the data is that the position of the peak does not change substantially with time, indicating that the spacing between the alkyl chains in the organized regions is constant. It is reasonable to assume that in the beginning of the reaction small domains of ordered alkyl chains form, giving rise to a weak scattering peak. Interestingly, the onset of a detectable diffraction peak occurs at surface areas significantly larger than the MMA attributed to the alkyl chain as reported by Fontaine et al.[269]

In fact, at such surface areas (corresponding to about 50% conversion), one would anticipate that the alkyl chains would be liquid-like and not ordered. Arrow **A** in Figure 5-18 also illustrates that diffraction also occurs prior to the gel point indicated by Arrow **B**, whose measurement is described in the earlier chapter. The appearance of the single

peak so early in the reaction, corresponding to such a large MMA, supports the notion of a formation of organized domains. Such results clearly demonstrate the value of obtaining direct structural data by GIXD to elucidate the mechanism of film formation on a molecular level.

These ordered domains most probably consist of fully hydrolyzed and partially condensed silane molecules dispersed in primarily disordered and partially reacted OTMS, consistent with the results obtained by Rondelez, et al.[261]

Clearly, the appearance of a diffraction peak indicates that OTMS undergoes a phase transition as the methoxy groups are hydrolyzed and the headgroups become smaller. At an MMA of 32.6 $Å^2$ (point A in Figure 5-18) the monolayer exists in a phase analogous to the condensed phase C in the unreacted OTMS as shown in Figure 5-11a. Interestingly, the initial appearance of order also occurred around the same MMA (~28 $Å^2$, see Figure 5-13) as when the unreacted monomer is being compressed.

The diffraction peak close to the onset of the condensed phase is commonly treated as due to hexatic order.[71] Unlike in truly crystalline structures, the molecular backbones in a structure possessing hexatic order are randomly oriented although there exist a long-range orientational order normal to the interface exists. This difference in molecular packing is depicted in Figure 5-19. In addition, hexatic structures have a short-range positional order in the range of few lattice units.[285]

Although there have been doubts regarding the assignment of certain phases as possessing hexatic order,[70] some indirect evidence has been brought out. Rivière[286] has shown that this phase is optically isotropic and possesses one first-order diffraction peak in the powder pattern. This would suggest that the structure could be a 2D liquid analo-

gous to a smectic liquid crystal, a hexagonal crystal or a hexatic. The fact that the usual peak width exceeds the resolution limit, i.e., broad diffraction peak, with positional correlation larger than that expected for liquid make the hexatic order as the most plausible structure in this phase.[71]



(a)                                  (b)
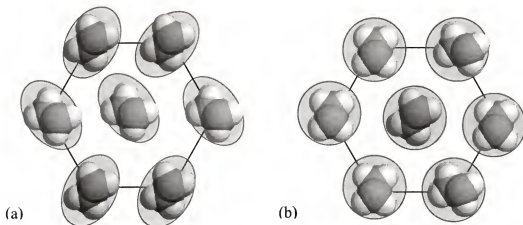
Figure 5-19. Molecular packing in (a) crystalline lattice and (b) hexatic lattice as seen normal to the interface. The shaded oval and circles indicates the average molecular orientation in the domain. Adapted from Kaganer and Loginov.[29]

For the hexatic order to arise, the molecular area must be larger than that that of close-packed alkyl chain to allow for the large degrees of freedom inherent in these structures. An indication of this possibility is shown in Figure 5-20 which illustrates that the molecular area is larger at the onset of the diffraction and shrinks by about 2% after 300 mins. This is comparable to the decrease in molecular area observed by Kaganer and co-workers in octadecanol monolayer as it undergoes $LS \rightarrow S$ transition.[285]

At this point, results have indicated that both unreacted OTMS and its product exhibit ordering at the air-water interface. While the unreacted OTMS shows evidence of a

distorted hexagonal lattice, the products seems to exhibit packing characteristic of hexagonally packed alkyl chains.

In the following section, it will be shown that the molecular packing at the onset of the diffraction is less densely packed than the final structure, further supporting the notion of hexatic order at least in the early part of the film-formation.
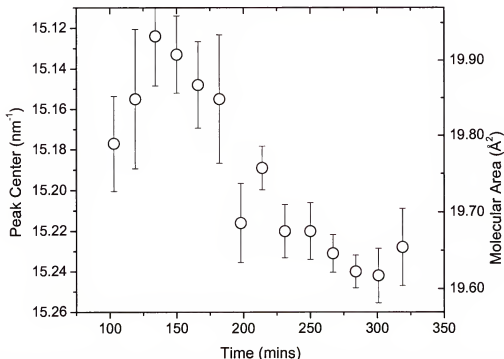


Figure 5-20. Variation in the peak center (left axis) and lattice parameter *a* (right axis) with reaction time.

"Rapid" Grazing Incidence X-ray Diffraction

The experiments described in the previous section were performed on a fairly slowly reacting system. As the pH is lowered, the rate of hydrolysis and condensation reactions can change drastically such that at pH 1.5 the reaction is complete after one hour.[269] This is supported by the results of area relaxation experiments discussed in the earlier Chapter. To be able to monitor the transformation in these systems, a modification of the scanning technique was made.

In the absence a wide area detector such as a CCD or an imaging plate, experiments were limited to the use of a scintillation counter point detectors. The conventional method of scanning a point detector at a predetermined angular step is painfully time consuming. In addition to the time required to move the detector arm and acquire the data, extra time is needed to allow the water surface to settle down after the detector arm has finished moving to the desired angle. This additional wait period can account for about 5-10 secs per step and slow down the complete scan for as much as 5 mins. The alternative approach is to sweep the detector arm continuously ("quickscan") at a predetermined scan rate.

The implementation of the quickscan scheme involves an alteration in the input/output controller (IOC) routines during data acquisition. In the conventional step-scan technique, the control software sets up the scaler (Joerger) hardware so that the IOC stops and resets the data acquisition after a certain number of counts are detected. In the quickscan scheme, the 10 Mhz internal clock of the scaler is used as the time base that defines an acquisition gate. The IOC then comes in to fetch the data for the duration of the preset acquisition time. This usually results to a decrease in the detected intensity by a factor of 10-100. However, this is inconsequential since the incident beam has sufficient intensity required for the experiment.

Using quickscan routines the reaction of OTMS monolayers at pH 1.5, 2.0, 3.0, and 3.5 were investigated. The fastest scan rate that was attained using this new scanning scheme was approximately 56 sec, a considerable improvement compared to the best scan rate of 16 mins for the conventional scanning.

Figure 5-21 shows typical peak intensity vs. time plot acquired for about an hour from a reacting OTMS system at pH 1.5. Similar to the observation described earlier, the peak intensity grows as the reaction time progress, up to a certain asymptotic value. However, in this case the ordering occurs very rapidly indicated by the early onset of diffraction at 100 sec.
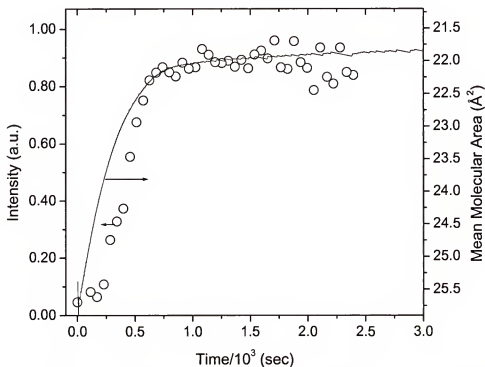


Figure 5-21. Intensity of the peak around $k_{xy}$ = 15 nm$^{-1}$ plotted against reaction time at subphase pH=1.5. Superimposed is the area relaxation curve of OTMS spread on the same subphase.

Also shown in Figure 5-21 is the result of an independent area relaxation experiment similar to ones described in the previous Chapter. Since the reaction is very rapid at this condition, the MMA rapidly decreases even before the desired surface pressure is attained. In this case, the initial value that was measured is already around 25 Å$^2$. The remarkable observation apparent here is that there seems to be a complete correspondence between the two curves although they characterize different length scales. While

the intensity data represents a microscopic description of the system, the mean molecular area curve is a representation of a gross macroscopic trend.

At higher pH, however, it was noted that the two datasets hardly coincide. As shown in Figure 5-22, the diffraction peak did not start to appear until more than 2000 sec has elapsed for a system at pH 3.5. At this point the monolayer has a MMA of ~30 Å$^2$, a value very close the onset of diffraction observed at pH 4.0 (see Figure 5-18). At $t = 7 \times 10^3$ sec, the diffraction peak height started to reach a plateau but the MMA curve has not reached its asymptote of 21 Å$^2$. This observation indicates that the hydrolysis occurs in random sites and that a significant amount of hydrolysis needs to occur before the molecules can self-assemble into ordered domains. The observation made at pH 1.5 was simply a consequence of the fast hydrolysis occurring in that system.
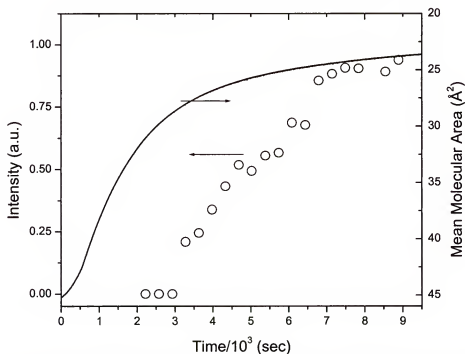


Figure 5-22. Intensity of the peak around $k_{xy} = 15$ nm$^{-1}$ plotted against reaction time at subphase pH=3.5. Superimposed is the area relaxation curve of OTMS spread on the same subphase.
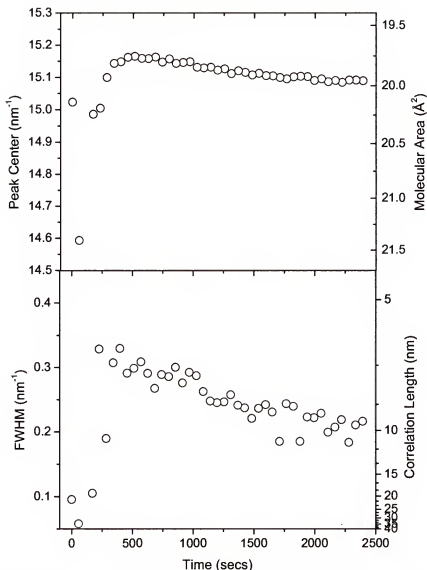
Figure 5-23. Variation in the peak centers and calculated FWHM for the reacting OTMS at pH 1.5 subphase.

The data shown in Figure 5-23 also mirrors the results obtained from slower kinetics at pH 4.0. The only difference is that the peak center was detected at $k_{xy}$= 14.6 nm$^{-1}$ which is equivalent to a molecular area that is larger than that initially measured previously. The correlation length was noted to generally increase with time consistent with the idea that the domains are growing in size with time. The initial increase in the FWHM is most likely an artifact, a consequence of poor peak resolution in the early stage of the reaction which results to abnormally narrow fits. This suspected artifact was also ob-

served but to a lesser extent in reactions at other pH values (see Figure 5-24, for example).
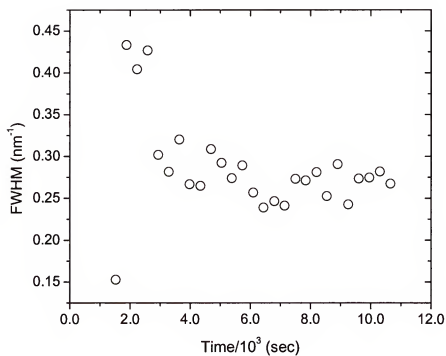


Figure 5-24. FWHM of diffraction peaks for OTMS reacting at pH 3.0.
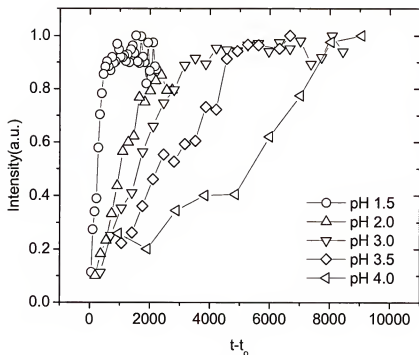
Figure 5-25. Intensity of diffraction plotted against ($t$-$t_o$) where $t_o$ is the onset of diffraction.

Figure 5-25 shows plots of normalized intensity of diffraction against $t$-$t_o$ where $t_o$ is the time at which a diffraction peak first appeared (see Table 5-3). The pH dependence of the rate at which the peak grows has very strong resemblance to the hydrolysis rate seen in the previous chapter. This clearly suggests that indeed the formation of silanols has a strong influence in the monolayer ordering.

Table 5-3. Onset of diffraction vs. pH

| pH | $t_o$, sec |
|---|---|
| 1.5 | 176 |
| 2.0 | 916 |
| 3.0 | 1522 |
| 3.5 | 2224 |
| 4.0 | 7140 |

To be able to have a better understanding of this evolution of peak height against time, it is necessary to look into scattering phenomena at the fundamental level.

For any set of scattering atoms, the intensity of diffraction is proportional to the square of the structure factor which can be expressed as

$$A(\mathbf{K}) = \sum_j f_j(K) \exp(i\mathbf{K} \cdot r_j) \qquad 5\text{-}7$$

where $\mathbf{K}$ is the scattering vector equal to the difference of the incident wave vector $\mathbf{k}_{in}$ and the scattered wave vector $\mathbf{k}_{out}$; $f_j(\mathbf{K})$ is the scattering factor of the $j$th atom located at $r_j$.[285] Depending on the crystal system, the structure factor can be a simple sum of $f_j$ or zero, in certain combinations of $hkl$ indices where the selection does not apply.[173] In any case where it is non-zero, the increase in the diffraction intensity would be proportional to the density of scattering elements. This would mean that in the case of this reacting monolayer system, the increasing intensity would be a result of either an increase in the number of nuclei of ordered domains or the continuous growth of the existing ones. In the former case, one would observe the correlation length of the domains to stay the same. If it were the latter case, on the other hand, one would observe some initial process that would eventually lead to an increase in the correlation length. This last hypothesis is partially confirmed in Figure 5-23.

If the abscissa in Figure 5-25 is transformed to ln($t$-$to$) instead, an interesting result is obtained. Not only that the monolayers seem to grow in a discontinuous manner but the curves seem to mirror each other. These curves might actually suggest that some universality in the manner in which the film grows. Looking at the time $t_d$ at which the discontinuity occurs, it appears to correlate within reasonable experimental error with gelation time $t_g$ determined from surface viscometry experiments. Unfortunately, surface viscosity determinations were only possible to be measured in two subphase pHs.

Table 5-4. Correspondence between the gelation time $t_g$ as determined from surface viscometry and the point of discontinuity, $t_d$.

| Subphase pH | $t_g/10^3$ sec | $t_d/10^3$ |
|---|---|---|
| 3.5 | $4.5 \pm 0.5$ | 4.0 |
| 4.0 | $8.7 \pm 0.8$ | 10.7 |
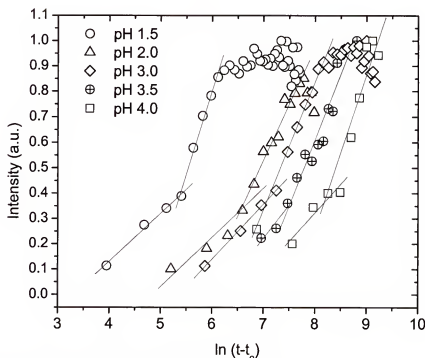


Figure 5-26. Plot of diffraction intensity against ln $(t-t_o)$.

The plots in Figure 5-26 indicate some sort of power scaling law similar to what was observed from compressibility modulus measurements. In fact, a distinctly similar scaling law has been found to govern the kinetics of cluster growth. At least two cases of aggregations have been considered: one in which the clustering process is controlled by diffusion and one in which no diffusion occurs. In the latter case, the clusters are static and exhibit growth pattern that scales similar to the properties of a percolating network. According to Ernst and Hendriks[287], the cluster size distribution $c_k(t)$ near the gel point $t_c$ behaves as

$$c_k(t) \sim k^{-\tau} \Phi\left(k|t - t_c|^{1/\sigma}\right)$$  5-8

where $k$ is the number of units in the cluster. The observation that the slope of the curves are very similar points to the universality predicted by Eqn. 5-8.

<u>Irradiation Damage</u>

Another remarkable result of this measurement is the exceptional chemical stability of the OTMS system to x-ray irradiation. As an illustration, the inset in Figure 5-27 shows a diffraction scan recorded at pH = 4 and $\Pi$ = 8 mN/m after more than 5 hours of reaction and irradiation; the second curve was obtained 15 minutes later from the same monolayer, but with the beam laterally displaced by about 1.5 cm, exposing a "fresh" area which had not previously been irradiated. These results indicate that the immense ($\sim 10^{13}$ photons/sec incident to the hutch) flux of 11 keV photons on the film did not break significant numbers of Si-O or Si-C bonds, or that any cleaved bonds reform almost quantitatively.
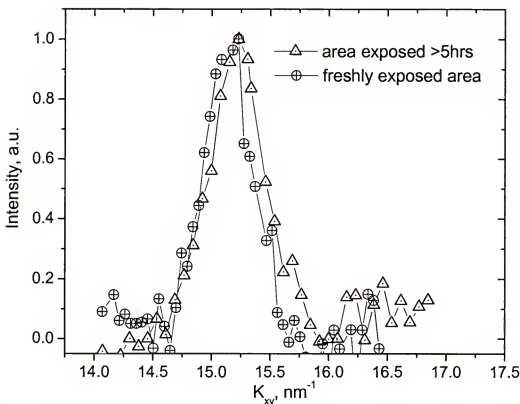
Figure 5-27. Diffraction peaks of the same film area where the diffraction curves in Figure 5-17 after cross-linking and 5 hours of X-ray irradiation is compared to an unirradiated surface ~15 minutes later, revealed by lateral displacement of trough surface.

## Conclusions

The studies discussed here have shown that high-brilliance synchrotron radiation can be used to take comparatively fast in-plane diffraction scans to follow a surface reaction *in situ*. The alkyl chains in OTMS spread on a clean water subphase self-assemble in small domains showing a characteristic in-plane spacing. Such a mechanism appears possible at fluid interfaces and thus in the absence of any anchoring to a solid substrate. The short-range positional order between the alkyl chains does not significantly change during the course of the reaction. The increase in intensity of the diffraction peaks with time can be interpreted either as an increase in the number of such ordered domains or the

transformation of the smaller domains into larger organized assemblies as the polymerization progresses.

Overall, these kinetics experiments have shown the potential of fast GIXD scans to study the surface dynamics of a variety of reactive amphiphile systems. It should be noted that the experimental setup described for these initial measurements is not yet optimized for highest brilliance and overall experimental speed. Further optical and detection enhancements such as the use of an area detector being currently planned should easily allow the scan time required for similar quality diffraction data to be reduced significantly.

CHAPTER 6
CONCLUSIONS AND RECOMMENDATIONS

Monolayer studies of OTMS showed that it forms a stable monolayer at the air-water interface. The use of an acidic subphase initiates cross-linking reaction which can be followed by monitoring the instantaneous surface compressional modulus and surface viscosity. Both techniques indicated that the product is potentially a network material. Brewster angle microscopy provided an insight into the film morphology at the early part of the reaction and around the gel point.

Comparison with a theoretical model based on percolation theory did not yield the exact behavior as predicted although the product exhibits the general behavior for a per-colating network, with a well-defined sol-gel transition observed from both compres-sional modulus and viscosity measurements. Percolation theory alone may not be ade-quate to describe the network formation in these types of materials because of several considerations, foremost of which is the frustration of network linkage due to the geomet-rical restriction around the silane headgroup. Other factor may include the shortcoming of the "lattice" assumption and the formation of cyclic oligomers. The former is most likely true since OTMS molecules, once hydrolyzed and occupy a smaller molecular area, may not entirely be restricted to static lattice points and may actually possess some freedom to move laterally such that diffusion might be a significant factor.

Although a full account of the reaction kinetics can not be derived because of the complexity of the reaction, analysis of the $A(t)$ relaxation curves has shown that the early part of the reaction can be analytically described by assuming that only hydrolysis reac-

tions occur and that the polycondensation reactions are insignificant at this stage. Results of this analysis indicate that the hydrolysis proceeds as a typical acid-catalyzed reaction with a first-order rate constant that reasonably compares to a reaction in bulk solution.

Grazing incidence x-ray diffraction studies were done to look into the kinetics of film formation in reacting OTMS monolayers. Initial results done at neutral pH subphase have shown that unreacted OTMS monolayer self-assembles into ordered domains. The domains show the characteristic in-plane ordering of a close-packed distorted hexagonal lattice. The product of reacted OTMS, on the other hand, was observed to be close-packed hexagonal with no molecular tilting detected.

To study the film formation at lower pH values where the kinetics is expected to be faster, a modification of the scanning routine was implemented. Preliminary investigation indicated that the technique is capable of reducing signal acquisition from tens of minutes down to less than a minute for scans of $k_{xy}$ of sufficient spatial and temporal resolution. One of the disadvantages of this scanning technique is the reduction of the detected intensity by at least an order of magnitude compared to the conventional scanning technique. However, this is of no serious consequence since the synchrotron source can yield photon flux $\sim 10^{13}$ photons/sec. Assuming proper alignment of the optics has been achieved, this intense radiation should consequently yield diffraction intensities that are sufficiently intense to be detected.

Using the modified technique, the reaction of OTMS at pH 1.5 subphase was successfully monitored with scans being completed at less than one minute interval. The results showed that the short-range positional ordering between the alkyl chains does not significantly change during the course of the reaction. However, the correlation length,

which indicates the extent of ordering, generally increases with time. This suggests that during the course of the reaction, the early nucleation sites grow in size to form larger clusters of ordered domains. This increase in cluster size can be brought about by the hydrolysis of OTMS molecules that are within the vicinity of the growing cluster or by the reaction of the silanol products with OTMS molecules at the periphery of the clusters to form condensation products. Eventually at the point of gelation, smaller clusters aggregate with other smaller clusters to yield larger clusters.
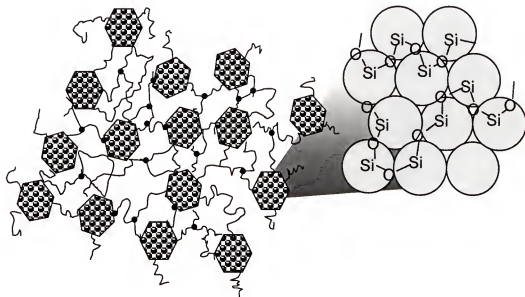


Figure 6-1. A depiction of the possible network morphology of the reaction product of OTMS. The inset shows the possible structure inside the ordered domains of hexagonally-packed lattice.

GIXD of OTMS at different pH values gave insight to the kinetics of film growth. Although the analysis is yet to be completed for this part of the study, the initial examination of the results pointed to some type of universality in the dynamics of film growth.

Overall, the results from both x-ray structural studies and interfacial measurements indicate possible network morphology similar to what is depicted in Figure 6-1. In this model, the origin of x-ray scattering is possibly from domains consist of hydrolyzed OTMS and linear polycondensation product. Separating these domains are regions of amorphous materials where possible network junctions are present. This model is in agreement with views presented in the literature, such as those suggested by Sjöblom[224] and Vidon.[223] It is also consistent with the observation regarding the precedence of onset of diffraction to the actual gel point as determined from viscometry.

In general, the current description of the network architecture in OTMS monolayers is still sketchy. Several additional investigations need to be pursued. Most important of these is molecular weight characterization, possibly during and after the reaction. If a real-time MW profile can be obtained, a direct correlation of $|t-t_c|$ and $|p-p_c|$ can be established and will contribute immensely to a better understanding of the network formation in OTMS.

Future studies should be also focused in investigating further the kinetics of film growth in these types of monolayers. Since the techniques presented here are broadly applicable to other monolayer systems, it would be also be interesting to investigate other similar systems. To achieve efficiency and convenience in future x-ray studies, a charge-couple device (CCD) detector is needed. It should allow for faster data acquisition and increased spatial resolution.

A series of related results that was not presented here concerning the preparation of hybrid thin films and core-shell particles should also be pursued. This area, which is a

direct offshoot of this study, can yield materials with interesting properties and novel applications.

# APPENDIX
## MOTOR NOMENCLATURE AT THE MRCAT BEAMLINE 10-ID

Table A-1. Goniometer and mirror motors designation as used in the MX software.
Adapted from a manuscript provided by MRCAT.

| Motor | MX Designation | "+"moves it |
|---|---|---|
| outboard table height | tab_out | up |
| inboard table height | tab_in | up |
| upstream table height | tab_upst | up |
| horizontal table | tab_tran | towards wall (as opposed to door side) |
| vertical table | tab_vert | up |
| Huber phi circle | hphi | clw |
| Huber chi circle | hchi | clw |
| Huber theta(vertical) | htheta | cclw |
| Huber 2theta(vertical) | hdelta | cclw |
| Huber theta(horizontal) | hmu | clw |
| Huber 2theta(horizontal) | hnu | cclw |
| Harmonic rejection mirror vertical | mirror1_vert | up |
| Harmonic rejection mirror angle | mirror1 | tilt up |
| Mirror 2 mount | hsmx | towards wall |
| Mirror 2 mount | hsmy | up |
| Mirror 2 tilt | mirror3 | tilt up |

Table A-2. Slit motors designation used in the MX software[1]

| MX designation | Motor | "+" moves |
|---|---|---|
| a_top | top horizontal | towards center |
| a_bottom | bottom horizontal blade | towards center |
| a_in | left vertical blade | towards center |
| a_out | right vertical blade | towards center |

Table A-3. Pseudo Motors on a Slit

| MX designation | motor | "+" moves |
|---|---|---|
| ah_center | coupled movement of *a_top* and *a_bottom* blades, moving at constant vertical separation | up (depending on the orientation of the motors) |
| ah_size | coupled movement of *a_top* and *a_bottom* blades to adjust their separation from *ah_center* | towards larger separation |
| av_center | coupled movement of *a_in* and *a_out* blades, moving at constant horizontal separation | away from the base |

| av_size | coupled movement of *a_in* and *a_out* blades to adjust their separation from *av_center* | towards larger separation |
|---|---|---|

Legend:
      clw: clockwise
      cclw: counter clockwise.

Note:
      [1]XIA slits are controlled by id2 and powered by a separate power supply; Up to four slits can be daisy-chained onto one power supply and one signal cable.

LIST OF REFERENCES

(1)   Finnie, K. R.; Haasch, R.; Nuzzo, R. G. *Langmuir* **2000**, *16*, 6968.

(2)   Zheng, J. W.; Zhu, Z. H.; Chen, H. F.; Liu, Z. F. *Langmuir* **2000**, *16*, 4409.

(3)   Richter, A. G.; Durbin, M. K.; Yu, C. J.; Dutta, L. *Langmuir* **1998**, *14*, 5980.

(4)   Cohen, S. R.; Naaman, R.; Sagiv, J. *J. Phys. Chem.* **1986**, *90*, 3054.

(5)   Schwartz, D. K.; Steinberg, S.; Israelachvili, J.; Zasadzinski, J. A. N. *Phys. Rev. Lett.* **1992**, *69*, 3354.

(6)   Bierbaum, K.; Grunze, M.; Baski, A. A.; Chi, L. F.; Schrepp, W.; Fuchs, H. *Langmuir* **1995**, *11*, 2143.

(7)   Carraro, C.; Yauw, O. W.; Sung, M. M.; Maboudian, R. *J. Phys. Chem. B* **1998**, *102*, 4441.

(8)   Sagiv, J. *J. Am. Chem. Soc.* **1980**, *102*, 92.

(9)   Dynarowicz-Latka, P.; Dhanabalan, A.; Oliveira, O. N. *Adv. Colloid Interface Sci.* **2001**, *91*, 221.

(10)  Gaines, G. L. *Insoluble Monolayers at Liquid-Gas Interfaces*; Interscience Publishers: New York, 1966.

(11)  Davies, J. T.; Rideal, E. K. *Interfacial Phenomena*; 2nd ed.; Academic Press: New York, 1963.

(12)  Adam, N. K. *The Physics and Chemistry of Surfaces*; 3d ed.; Oxford University Press H. Milford: London, 1941.

(13)  Petty, M. C. *Langmuir-Blodgett Films: An Introduction*; Cambridge University Press: Cambridge ; New York, 1996.

(14)  Roberts, G. *Langmuir-Blodgett Films*; Plenum Press: New York, 1990.

(15)  Ulman, A. *An Introduction to Ultrathin Organic Films : From Langmuir-Blodgett to Self-Assembly*; Academic Press: Boston, 1991.

(16)  Franklin, B. *Philos. Trans. R. Soc. London* **1774**, *64*, 445.

(17)  Langmuir, I. *J. Am. Chem. Soc.* **1917**, *39*, 1848.

(18)  Pockels *Nature* **1891**, *43*, 437.

(19)  Rayleigh, R. *Proc. R. Soc.* **1890**, *47*, 364.

(20)  Hardy, W. B. *Proc. R. Soc.* **1913**, *A88*, 303.

(21)  Hardy, W. B. *Proc. R. Soc.* **1912**, *A86*, 610.

(22)  Devaux, H. *Smithsonian Inst., Ann. Rept.* **1913**, 261.

(23)  Langmuir, I. *J. Am. Chem. Soc.* **1916**, *38*, 221.

(24)  Blodgett, K. *J. Am. Chem. Soc.* **1935**, *57*, 1007.

(25)  Harkins, W. D.; Copeland, L. E. *J. Chem. Phys.* **1942**, *10*, 272.

(26)  Ställberg-Stenhagen, S.; Stenhagen, E. *Nature* **1945**, *156*, 239.

(27)  Dutta, P.; Peng, J. B.; Lin, B.; Ketterson, J. B.; Prakash, M.; Georgopoulos, P.; Ehrlich, S. *Phys. Rev. Lett.* **1987**, *58*, 2228.

(28)  Kjaer, K.; Als-Nielsen, J.; Helm, C. A.; Laxhuber, L. A.; Mohwald, H. *Phys. Rev. Lett.* **1987**, *58*, 2224.

(29)  Kaganer, V. M.; Loginov, E. B. *Phys. Rev. E* **1995**, *51*, 2237.

(30)  Langmuir, I. *Metall. Chem. Eng.* **1916**, *15*, 469.

(31)  Harkins, W. D. *J. Am. Chem. Soc.* **1917**, *39*, 354.

(32)  Harkins, W. D. *J. Am. Chem. Soc.* **1917**, *39*, 541.

(33)  Tadros, T. F. *Surfactants*; Academic Press: London ; Orlando, 1984.

(34)  Chattoraj, D. K.; Birdi, K. S. *Adsorption and the Gibbs Surface Excess*; Plenum Press: New York, 1984.

(35)  Gibbs, J. W.; Bumstead, H. A.; Van Name, R. G.; Longley, W. R. *The Collected Works of J. Willard Gibbs*; Longmans Green: New York, 1931.

(36)  Guggenheim, E. A. *Thermodynamics; an Advanced Treatment for Chemists and Physicists*; 5th rev. ed.; North-Holland Pub. Co.: Amsterdam, 1967.

(37)  Ehrenfest, P. *Proc. Koninkl. Akad. Amsterdam* **1933**, *36*, 115.

(38)  Miyano, K. A., M.; Ketterson, J.B.; Xu, S.Q. *J. Chem. Phys.* **1983**, *78*, 4776.

(39) Barton, S. W.; Goudot, A.; Bouloussa, O.; Rondelez, F.; Lin, B. H.; Novak, F.; Acero, A.; Rice, S. A. *J. Chem. Phys.* **1992**, *96*, 1343.

(40) Gaines, G. L. *J. Chem. Phys.* **1978**, *69*, 924.

(41) Lifschitz, E. M. *Acta Physichochim. U.R.S.S.* **1944**, *19*.

(42) Lundquist, M. *Chem. Scripta* **1971**, *1*, 5.

(43) Ries, H. E. *Sci. Am.* **1961**, *204*, 152.

(44) Germer, L. H.; Storks, K. H. *J. Chem. Phys.* **1938**, *6*, 280.

(45) Teissie, J. *J. Colloid Interface Sci.* **1979**, *70*, 90.

(46) von Tscharner, V.; McConnell, H. M. *Biophys. J* . **1981**, *36*, 409.

(47) von Tscharner, V.; McConnell, H. M. *Biophys. J* . **1981**, *36*, 421.

(48) McConnell, H. M.; Tamm, L. K.; Weis, R. M. *Proc. Natl. Acad. Sci. (Phys. Sci.)* **1984**, *81*, 3249.

(49) Lösche, M.; Sackmann, E.; Möhwald, H. *Ber. Bunsen-Ges. Phys. Chem. Chem. Phys.* **1983**, *87*, 848.

(50) Lösche, M.; Möhwald, H. *Rev. Sci. Instrum.* **1984**, *55*, 1968.

(51) Albrecht, O.; Gruler, H.; Sackmann, E. *J. Phys.* **1978**, *39*, 301.

(52) Cadenhead, D. A.; Müller-Landau, F.; Kellner, B. M. J. In *Ordering in Two Dimensions*; Sinha, S. K., Ed.; Elsevier/ North Holland Biomedical Press: Amsterdam, 1980; p 73.

(53) Honig, D.; Möbius, D. *J. Phys. Chem.* **1991**, *95*, 4590.

(54) Hénon, S.; Meunier, J. *Rev. Sci. Instrum.* **1991**, *62*, 936.

(55) Overbeck, G. A.; Mobius, D. *J. Phys. Chem.* **1993**, *97*, 7999.

(56) Lautz, C.; Fischer, T. M. *Jpn. J. Appl. Phys. Part 1 - Regul. Pap. Short Notes Rev. Pap.* **1997**, *36*, 5703.

(57) Lautz, C.; Fischer, T. M. *J. Phys. Chem. B* **1997**, *101*, 8790.

(58) Lautz, C.; Fischer, T. M.; Kildea, J. *J. Chem. Phys.* **1997**, *106*, 7448.

(59) Lautz, C.; Fischer, T. M. *Materials Science & Engineering C-Biomimetic Materials Sensors and Systems* **1998**, *5*, 271.

(60) Lautz, C.; Fischer, T. M.; Weygand, M.; Losche, M.; Howes, P. B.; Kjaer, K. *J. Chem. Phys.* **1998**, *108*, 4640.

(61) Blaudez, D.; Buffeteau, T.; Desbat, B.; Turlet, J. M. *Current Opinion in Colloid & Interface Science* **1999**, *4*, 265.

(62) Mendelsohn, R.; Brauner, J. W.; Gericke, A. *Annu. Rev. Phys. Chem.* **1995**, *46*, 305.

(63) Baekmark, T. R.; Wiesenthal, T.; Kuhn, P.; Bayerl, T. M.; Nuyken, O.; Merkel, R. *Langmuir* **1997**, *13*, 5521.

(64) Baekmark, T. R.; Wiesenthal, T.; Kuhn, P.; Albersdorfer, A.; Nuyken, O.; Merkel, R. *Langmuir* **1999**, *15*, 3616.

(65) Wiesenthal, T.; Baekmark, T. R.; Merkel, R. *Langmuir* **1999**, *15*, 6837.

(66) Buontempo, J. T.; Rice, S. A. *J. Chem. Phys.* **1993**, *98*, 5835.

(67) Lin, B.; Shih, M. C.; Bohanon, T. M.; Ice, G. E.; Dutta, P. *Phys. Rev. Lett.* **1990**, *65*, 191.

(68) Shih, M. C.; Bohanon, T. M.; Mikrut, J. M.; Zschack, P.; Dutta, P. *Phys. Rev. A* **1992**, *45*, 5734.

(69) Doucet, J.; Denicolo, I.; Creievich, A.; Collet, A. *J. Chem. Phys.* **1981**, *75*, 5125.

(70) Sirota, E. B. *Langmuir* **1997**, *13*, 3849.

(71) Kaganer, V. M.; Mohwald, H.; Dutta, P. *Rev. Mod. Phys.* **1999**, *71*, 779.

(72) Peterson, I. R.; Kenn, R. M.; Goudot, A.; Fontaine, P.; Rondelez, F.; Bouwman, W. G.; Kjaer, K. *Phys. Rev. E* **1996**, *53*, 667.

(73) Bibo, A. M.; Knobler, C. M.; Peterson, I. R. *J. Phys. Chem.* **1991**, *95*, 5591.

(74) Knobler, C. M. *Mol. Cryst. Liquid Cryst.* **2001**, *364*, 133.

(75) Knobler, C. M. *Nuovo Cimento Soc. Ital. Fis. D-Condens. Matter At. Mol. Chem. Phys. Fluids Plasmas Biophys.* **1994**, *16*, 1367.

(76) Ruizgarcia, J.; Qiu, X.; Tsao, M. W.; Marshall, G.; Knobler, C. M.; Overbeck, G. A.; Mobius, D. *J. Phys. Chem.* **1993**, *97*, 6955.

(77) Schwartz, D. K.; Schlossman, M. L.; Pershan, P. S. *J. Chem. Phys.* **1992**, *96*, 2356.

(78) Brock, J. D.; Aharony, A.; Birgeneau, R. J.; Evanslutterodt, K. W.; Litster, J. D.; Horn, P. M.; Stephenson, G. B.; Tajbakhsh, A. R. *Phys. Rev. Lett.* **1986**, *57*, 98.

(79) Singh, S. *Phys. Rep.* **2000**, *324*, 107.

(80) Peterson, I. R. *Ber. Bunsen-Ges. Phys. Chem. Chem. Phys.* **1991**, *95*, 1417.

(81) Bibo, A. M.; Peterson, I. R. *Adv. Mater.* **1990**, *2*, 309.

(82) Kimelberg, H. K.; Papahadjopoulos, D. *Biochim. Biophys. Acta* **1971**, *233*, 805.

(83) Marshall, C.; Teer, E.; Knobler, C. M.; Schalke, M.; Losche, M. *Colloid Surf. A-Physicochem. Eng. Asp.* **2000**, *171*, 41.

(84) Miyashita, T.; Ito, Y. *Thin Solid Films* **1995**, *260*, 217.

(85) Adam, N. K. *Proc. R. Soc. London, Ser. A* **1923**, *103*, 687.

(86) Peterson, I. R.; Brzezinski, V.; Kenn, R. M.; Steitz, R. *Langmuir* **1992**, *8*, 2995.

(87) Stadler, C.; Schmid, F. *J. Chem. Phys.* **1999**, *110*, 9697.

(88) Polimeno, A.; Ros, J. M.; Levine, Y. K. *J. Chem. Phys.* **2001**, *115*, 6185.

(89) Ali, S.; Smaby, J. M.; Brown, R. E. *Biochemistry* **1993**, *32*, 11696.

(90) Schmid, F.; Schick, M. *J. Chem. Phys.* **1995**, *102*, 2080.

(91) Schmid, F.; Lange, H. *J. Chem. Phys.* **1997**, *106*, 3757.

(92) Schmid, F. *Phys. Rev. E* **1997**, *55*, 5774.

(93) Siegel, S.; Vollhardt, D.; Brezesinski, G.; Bringezu, F.; Mohwald, H. *Materials Science & Engineering C-Biomimetic and Supramolecular Systems* **1999**, *8-9*, 3.

(94) Brezesinski, G.; Dietrich, A.; Struth, B.; Bohm, C.; Bouwman, W. G.; Kjaer, K.; Mohwald, H. *Chem. Phys. Lipids* **1995**, *76*, 145.

(95) Crisp, D. J. *J. Colloid Sci.* **1946**, *1*, 49.

(96) Crisp, D. J. *J. Colloid Sci.* **1946**, *1*, 161.

(97) Fowkes, F. M. *J. Phys. Chem.* **1964**, *68*, 3515.

(98) Goedel, W. A. In *Organic Thin Films*, 1998; Vol. 695, pp 10.

(99)  Heger, R.; Goedel, W. A. *Macromolecules* **1996**, *29*, 8912.

(100) daSilva, A. M. G.; Filipe, E. J. M.; dOliveira, J. M. R.; Martinho, J. M. G. *Langmuir* **1996**, *12*, 6547.

(101) Faure, M. C.; Bassereau, P.; Lee, L. T.; Menelle, A.; Lheveder, C. *Macromolecules* **1999**, *32*, 8538.

(102) Bowers, J.; Zarbakhsh, A.; Webster, J. R. P.; Hutchings, L. R.; Richards, R. W. *Langmuir* **2001**, *17*, 131.

(103) Li, S.; Clarke, C. J.; Lennox, R. B.; Eisenberg, A. *Colloid Surf. A-Physicochem. Eng. Asp.* **1998**, *133*, 191.

(104) Zhu, J. Y.; Eisenberg, A.; Lennox, R. B. *J. Am. Chem. Soc.* **1991**, *113*, 5583.

(105) Schenning, A.; Elissen-Roman, C.; Weener, J. W.; Baars, M.; van der Gaast, S. J.; Meijer, E. W. *J. Am. Chem. Soc.* **1998**, *120*, 8199.

(106) Hilltrop, K.; Stegenmeyer, H. *Mol. Cryst. Liquid Cryst.* **1978**, *49*, 61.

(107) Kahn, F. J. *Appl. Phys. Lett.* **1975**, *22*, 386.

(108) Dimitrakopoulos, C. D.; Mascaro, D. J. *IBM J. Res. Dev.* **2001**, *45*, 11.

(109) Paloheimo, J.; Kuivalainen, P.; Stubb, H.; Vuorimaa, E.; Yli-Lahti, P. *Appl. Phys. Lett.* **1990**, *56*, 1157.

(110) Paloheimo, J.; Stubb, H.; Yli-Lahti, P.; Dyreklev, P.; Inganäs, O. *Thin Solid Films* **1992**, *210/211*.

(111) Barraud, A.; Rosilio, C.; R-Teixier, A. *J. Colloid Interface Sci.* **1977**, *62*, 509.

(112) Barraud, A.; Rosilio, C.; R-Teixier, A. *Thin Solid Films* **1980**, *68*, 91.

(113) Barraud, A.; Rosilio, C.; R-Teixier, A. *Thin Solid Films* **1980**, *68*, 99.

(114) Fariss, F.; Lando, J. B.; Rickert, S. *Thin Solid Films* **1983**, *99*, 305.

(115) Tsukruk, W. *Adv. Mater.* **2001**, *13*, 95.

(116) Carpick, R. W.; Salmeron, M. *Chem. Rev.* **1997**, *97*, 1163.

(117) Kuhn, H.; Möbius, D.; Bücher, H. In; Weissberger, A., Rossiter, B., Eds.; John Wiley: New York, 1972; Vol. 1, p 577.

(118) Kuhn, H. *Thin Solid Films* **1983**, *99*, 1.

(119) Charych, D.; Cheng, Q.; Reichert, A.; Kuziemko, G.; Stroh, M.; Nagy, J. O.; Spevak, W.; Stevens, R. C. *Chemistry & Biology* **1996**, *3*, 113.

(120) Casas, M.; Boissonnade, M. M.; Baszkin, A. *Colloids Surf.* **1992**, *68*, 207.

(121) Nutting, G. C.; Harkins, W. D. *J. Am. Chem. Soc.* **1939**, *61*, 2040.

(122) Stenhagen, E. In; Academic Press: New York, 1955; p 325.

(123) Sucker, C. *Kolloid Z.* **1963**, *190*, 146.

(124) Smith, T. *J. Colloid Interface Sci.* **1968**, *26*, 509.

(125) Fromherz, P. *Rev. Sci. Instrum.* **1975**, *46*, 1380.

(126) Zilversmit, D. B. *J. Colloid Sci.* **1963**, *18*, 794.

(127) Langmuir, I.; Schaefer, V. J. *J. Am. Chem. Soc.* **1937**, *59*, 2400.

(128) Wilhelmy, L. *Ann. Phys. Chem.* **1863**, *119*, 177.

(129) Dervichian, D. G. *J. Phys. Radium* **1935**, *6*, 221.

(130) Dervichian, D. G. *J. Chem. Phys.* **1939**, *7*, 931.

(131) Harkins, W. D.; Anderson, T. F. *J. Am. Chem. Soc.* **1937**, *59*, 2189.

(132) Adam, N. K.; Jessop, G. *Proc. R. Soc. London, Ser. A* **1926**, *112*, 362.

(133) Albrecht, O. *Thin Solid Films* **1983**, *99*, 227.

(134) Munger, G.; Leblanc, R. M. *Rev. Sci. Instrum.* **1980**, *51*, 710.

(135) Bonosi, F.; Renault, A.; Berge, B. *Langmuir* **1996**, *12*, 784.

(136) Berge, B.; Konovalov, O.; Lajzerowicz, J.; Renault, A.; Rieu, J. P.; Vallade, M.; Als-Nielsen, J.; Grubel, G.; Legrand, J. F. *Phys. Rev. Lett.* **1994**, *73*, 1652.

(137) Rieu, J. P.; Legrand, J. F.; Renault, A.; Berge, B.; Ocko, B. M.; Wu, X. Z.; Deutsch, M. *J. Phys. II* **1995**, *5*, 607.

(138) Zhu, R.; Wei, Y.; Scholl, B.; Schmitt, H. J. *Sens. Actuator A-Phys.* **1995**, *50*, 13.

(139) Peterson, I. R. *Thin Solid Films* **1985**, *134*, 135.

(140) Brockman, H. L.; Smaby, J. M.; Jarvis, D. E. *Journal of Physics E-Scientific Instruments* **1984**, *17*, 351.

(141) KSV Instruments Ltd. In: Helsinki, Finland.

(142) Navathe, C. P.; Dashora, B. L.; Roy, U. N.; Singh, R.; Maheswari, S.; Kukreja, L. M. *Meas. Sci. Technol.* **1998**, *9*, 540.

(143) Diniz, J. M. B. F.; Armitage, D. A.; Linford, R. G.; Pavlidis, V. H. *Langmuir* **1992**, *8*, 2084.

(144) Albrecht, O.; Matsuda, H.; Eguchi, K.; Nakagiri, T. *Thin Solid Films* **1999**, *338*, 252.

(145) Collins, S. J.; Mahesh, G. N.; Radhakrishnan, G.; Dhathathreyan, A. *Colloid Surf. A-Physicochem. Eng. Asp.* **1995**, *95*, 293.

(146) Dynarowicz-Latka, P.; Taylor, D. M.; Dhindsa, A. S.; Underhill, A. E. *Bull. Pol. Acad. Sci.-Chem.* **1997**, *45*, 459.

(147) Hasegawa, K.; Hosoi, K.; Tomioka, A.; Miyano, K. *Appl. Phys. Lett.* **1994**, *64*, 664.

(148) Welzel, P. B.; Weis, I.; Schwarz, G. *Colloid Surf. A-Physicochem. Eng. Asp.* **1998**, *144*, 229.

(149) Gaines, G. L. *J. Colloid Interface Sci.* **1984**, *98*, 272.

(150) Peng, J. B.; Barnes, G. T.; Abraham, B. M. *Langmuir* **1993**, *9*, 3574.

(151) Malcolm, B. R. *Thin Solid Films* **1989**, *178*, 191.

(152) Malcolm, B. R. *Thin Solid Films* **1989**, *178*, 17.

(153) Birdi, K. S. *Lipid and Biopolymer Monolayers at Liquid Interfaces*; Plenum Press: New York, 1989.

(154) Kokelaar, J. J.; Prins, A. *J. Cereal Sci.* **1995**, *22*, 53.

(155) Jarvis, N. L. "Surface Viscosity of Monomolecular Films on Water at Low Film Pressures," U. S. Naval Research Laboratory, 1962.

(156) Kawaguchi, M. *Prog. Polym. Sci.* **1993**, *18*, 341.

(157) Goodrich, F. C. In *Progress in Surface and Membrane Science*; Danielli, J. F., Rosenberg, M. D., Cadenhead, D. A., Eds.; Academic Press: New York, 1973; Vol. 7, pp 151.

(158) Hühnerfuss, H. *J. Colloid Interface Sci.* **1985**, *107*, 84.

(159) Myers, R. J.; Harkins, W. D. *J. Chem. Phys.* **1937**, *5*, 601.

(160) Harkins, W. D.; Kirkwood, J. G. *J. Chem. Phys.* **1938**, *6*, 53.

(161) Fischer, B.; Teer, E.; Knobler, C. M. *J. Chem. Phys.* **1995**, *103*, 2365.

(162) Binnig, G.; Rohrer, H. *Helv. Chim. Acta* **1982**, *55*, 726.

(163) Binnig, G.; Rohrer, H.; Gerber, C.; Weibel, E. *Appl. Phys. Lett.* **1982**, *40*, 178.

(164) Binnig, G.; Quate, C. F.; Gerber, C. *Phys. Rev. Lett.* **1986**, *12*, 930.

(165) Sakurai, T.; Watanabe, Y. *Advances in Scanning Probe Microscopy*; Springer: Berlin ; New York, 2000.

(166) Lillehei, P. T.; Bottomley, L. A. *Anal. Chem.* **2000**, *72*, 189R.

(167) Bottomley, L. A.; Coury, J. E.; First, P. N. *Anal. Chem.* **1996**, *68*, R185.

(168) Poirier, G. E. *Chem. Rev.* **1997**, *97*, 1117.

(169) Digital Instruments *Spm Software Ver 4.1 Manual*, 1993.

(170) Frisbie, C. D.; Rozsnyai, A.; Noy, A.; Wrighton, M. S.; Lieber, C. M. *Science* **1994**, *265*, 2071.

(171) Schwartz, D. K. *Surf. Sci. Rep.* **1997**, *27*, 245.

(172) Peng, J. B.; Barnes, G. T.; Gentle, I. R. *Adv. Colloid Interface Sci.* **2001**, *91*, 163.

(173) Cullity, B. D. *Elements of X-Ray Diffraction*; Addison-Wesley Publishing Company: Reading, MA, 1978.

(174) Fuoss, P. H.; Liang, K. S.; Eisenberg, P. In *Synchrotron Radiation Research: Advances in Surface and Interface Science*; Bachrach, R. Z., Ed.; Plenum: New York, 1992; Vol. 1, pp 385.

(175) Marra, W. C.; Eisenberger, P.; Cho, A. Y. *J. Appl. Phys.* **1979**, *50*, 6927.

(176) Eisenberger, P.; Marra, W. C. *Phys. Rev. Lett.* **1981**, *46*, 1081.

(177) Koch, E.-E. *Handbook on Synchrotron Radiation*; North-Holland Publishing Company: Amsterdam, 1983; Vol. 1A.

(178) Winick, H.; Bienenstock, A. *Annu. Rev. Nucl. Part. Sci.* **1978**, *28*, 33.

(179) Kuzmenko, I.; Rapaport, H.; Kjaer, K.; Als-Nielsen, J.; Weissbuch, I.; Lahav, M.; Leiserowitz, L. *Chem. Rev.* **2001**, *101*, 1659.

(180) Als-Nielsen, J.; Jacquemain, D.; Kjaer, K.; Leveiller, F.; Lahav, M.; Leiserowitz, L. *Phys. Rep.-Rev. Sec. Phys. Lett.* **1994**, *246*, 252.

(181) James, R. W. *The Optical Principles of Diffraction of X-Rays*; Ox Bow: Woodbridge, CT, 1982.

(182) Chason, E.; Mayers, T. M. *Crit. Rev. Solid State Mater. Sci.* **1997**, *22*, 1.

(183) Lvov, Y.; Essler, F.; Decher, G. *J. Phys. Chem.* **1993**, *97*, 13773.

(184) Li, Z.; Zhao, M. W.; Quinn, J.; Rafailovich, M. H.; Sokolov, J.; Lennox, R. B.; Eisenberg, A.; Wu, X. Z.; Kim, M. W.; Sinha, S. K.; Tolan, M. *Langmuir* **1995**, *11*, 4785.

(185) Jacquemain, D.; Wolf, S. G.; Leveiller, F.; Deutsch, M.; Kjaer, K.; Alsnielsen, J.; Lahav, M.; Leiserowitz, L. *Angew. Chem.-Int. Edit. Engl.* **1992**, *31*, 130.

(186) Decher, G. In *Photonic and Optoelectronic Polymers*, 1997; Vol. 672, pp 445.

(187) Sinha, S. K. *Curr. Opin. Solid State Mat. Sci.* **1996**, *1*, 645.

(188) Foster, M. D. *Crit. Rev. Anal. Chem.* **1993**, *24*, 179.

(189) Adamson, A. W.; Gast, A. P. *Physical Chemistry of Surfaces*; 6th ed.; Wiley: New York, 1997.

(190) Gruniger, H.; Möbius, D.; Meyer, H. *J. Chem. Phys.* **1983**, *76*, 3701.

(191) Ariga, K.; Kunitake, T.; Furuta, H. *J. Chem. Soc., Perkin Trans. 2* **1996**, 667.

(192) Engelking, J.; Menzel, H. *Thin Solid Films* **1998**, *327/329*, 90.

(193) Ubukata, T.; Seki, T.; Ichimura, K. *Macromol. Symp.* **1999**, *137*, 25.

(194) Matsumoto, M.; Miyazaki, D.; Tanaka, M.; Azumi, R.; Manda, E.; Kondo, Y.; Yoshino, N.; Tachibana, H. *J. Am. Chem. Soc.* **1998**, *120*, 1479.

(195) Taniike, K.; Matsumoto, T.; Sato, T.; Ozaki, Y.; Nakashima, K.; Iriyama, K. *J. Phys. Chem.* **1996**, *100*, 15508.

(196) Zhao, B.; Li, H. B.; Zhang, X.; Shen, J. C.; Ozaki, Y. *J. Phys. Chem. B* **1998**, *102*, 6515.

(197) Dluhy, R. A.; Stephens, S. M.; Widayati, S.; Williams, A. D. *Spectroc. Acta Pt. A-Molec. Biomolec. Spectr.* **1995**, *51*, 1413.

(198) Cordero, S. R.; Weston, K. D.; Buratto, S. K. *Thin Solid Films* **2000**, *360*, 139.

(199) Miyashita, T. *Prog. Polym. Sci.* **1993**, *18*, 263.

(200) Miyano, K.; Veyssie, M. *Phys. Rev. Lett.* **1984**, *52*, 1318.

(201) Heger, R.; Goedel, W. A. *Supramol. Sci.* **1997**, *4*, 301.

(202) Kolchens, S.; Lamparski, H.; Obrien, D. F. *Macromolecules* **1993**, *26*, 398.

(203) Sisson, T. M.; Lamparski, H. G.; Kolchens, S.; Elayadi, A.; Obrien, D. F. *Macromolecules* **1996**, *29*, 8321.

(204) Zhang, L. H.; Hendel, R. A.; Cozzi, P. G.; Regen, S. L. *J. Am. Chem. Soc.* **1999**, *121*, 1621.

(205) Schoberl, U.; Magnera, T. F.; Harrison, R. M.; Fleischer, F.; Pflug, J. L.; Schwab, P. F. H.; Meng, X. S.; Lipiak, D.; Noll, B. C.; Allured, V. S.; Rudalevige, T.; Lee, S.; Michl, J. *J. Am. Chem. Soc.* **1997**, *119*, 3907.

(206) Kloeppner, L. J.; Duran, R. S. *J. Am. Chem. Soc.* **1999**, *121*, 8108.

(207) Cerveau, G.; Corriu, R. J. P. *Coord. Chem. Rev.* **1998**, *180*, 1051.

(208) Mann, S.; Burkett, S. L.; Davis, S. A.; Fowler, C. E.; Mendelson, N. H.; Sims, S. D.; Walsh, D.; Whilton, N. T. *Chem. Mater.* **1997**, *9*, 2300.

(209) Baney, R. H.; Itoh, M.; Sakakibara, A.; Suzuki, T. *Chem. Rev.* **1995**, *95*, 1409.

(210) Hedrick, J. L.; Miller, R. D.; Yoon, D.; Cha, H. J.; Brown, H. R.; Srinivasan, S. A.; Di Pietro, R.; Flores, V.; Hummer, J.; Cook, R.; Liniger, E.; Simonyi, E.; Klaus, D. In *Organic Thin Films*, 1998; Vol. 695, pp 371.

(211) Yamada, N.; Takahashi, T. *J. Electrochem. Soc.* **2000**, *147*, 1477.

(212) Barton, T. J.; Bull, L. M.; Klemperer, W. G.; Loy, D. A.; McEnaney, B.; Misono, M.; Monson, P. A.; Pez, G.; Scherer, G. W.; Vartuli, J. C.; Yaghi, O. M. *Chem. Mater.* **1999**, *11*, 2633.

(213) Pajonk, G. M. *Catal. Today* **1997**, *35*, 319.

(214) Ward, D. A.; Ho, E. I. *Ind. Eng. Chem. Res.* **1995**, *34*, 421.

(215) Gvishi, R.; Narang, U.; Ruland, G.; Kumar, D. N.; Prasad, P. N. *Appl. Organomet. Chem.* **1997**, *11*, 107.

(216) Beecroft, L. L.; Ober, C. K. *Chem. Mater.* **1997**, *9*, 1302.

(217) Cerveau, G.; Corriu, R. J. P.; Lepeytre, C. *J. Organomet. Chem.* **1997**, *548*, 99.

(218) Barrie, P. J.; Carr, S. W.; Li Ou, D.; Sullivan, A. C. *Chem. Mater.* **1995**, *7*, 265.

(219) Alam, T. M.; Assink, R. A.; Loy, D. A. *Chem. Mater.* **1996**, *8*, 2366.

(220) Alam, T. M. *Spectroc. Acta Pt. A-Molec. Biomolec. Spectr.* **1997**, *53*, 545.

(221) Parikh, A. N.; Schivley, M. A.; Koo, E.; Seshadri, K.; Aurentz, D.; Mueller, K.; Allara, D. L. *J. Am. Chem. Soc.* **1997**, *119*, 3135.

(222) Britt, D. W.; Hlady, V. *J. Phys. Chem. B* **1999**, *103*, 2749.

(223) Vidon, S.; Leblanc, R. M. *J. Phys. Chem. B* **1998**, *102*, 1279.

(224) Sjöblom, J.; Stakkestad, G.; Ebeltoft, H.; Friberg, S. E.; Claesson, P. *Langmuir* **1995**, *11*, 2652.

(225) Brosseau, J.-L.; Vidon, S.; Leblanc, R. M. *J. Chem. Phys.* **1998**, *108*, 7391.

(226) Rolandi, R.; Gussoni, A.; Maga, L.; Robello, M.; Tundo, P. *Thin Solid Films* **1992**, *210/211*, 412.

(227) Taylor, D. M.; Gupta, S. K.; Dynarowicz, P. *Thin Solid Films* **1996**, *284-285*, 80.

(228) Linden, M.; Slotte, J. P.; Rosenholm, J. B. *Langmuir Turku,Finland Abo Akad Univ,Dept Biochem & Pharm,Biocity,Fin-20500 Turku,Finland* **1996**, *12*, 4449.

(229) Smith, R. D.; Berg, J. C. *J. Colloid Interface Sci.* **1980**, *74*, 273.

(230) Britt, D. W.; Hlady, V. *Langmuir* **1999**, *15*, 1770.

(231) Babonneau, F.; Maquet, J. *Polyhedron* **2000**, *19*, 315.

(232) Surivet, F.; Lam, T. M.; Pascault, J. P.; Pham, Q. T. *Macromolecules* **1992**, *25*, 4309.

(233) Sjöblom, J.; Ebeltoft, H.; Bjørseth, A.; Friberg, S. E.; Brancewicz, C. J. *Dispersion Sci. Technol.* **1994**, *15*, 21.

(234) Beari, F.; Brand, M.; Jenkner, P.; Lehnert, R.; Metternich, H. J.; Monkiewicz, J.; Siesler, H. W. *J. Organomet. Chem.* **2001**, *625*, 208.

(235) Leidler, K. J. *Chemical Kinetics*; 3rd ed.; HarperCollinsPublishers, Inc.: New York, NY, 1987.

(236) Davies, J. T. *Adv. Catal.* **1954**, *6*, 1.

(237) Peters, R. A. *Trans. Faraday Soc.* **1930**, *26*, 197.

(238) Carino, S. R.; Duran, R. S.; Baney, R. H.; Gower, L. A.; He, L.; Sheth, P. K. *J. Am. Chem. Soc.* **2001**, *123*, 2103.

(239) Zakri, C.; Renault, A.; Rieu, J. P.; Vallade, M.; Berge, B.; Legrand, J. F.; Vignault, G.; Grubel, G. *Phys. Rev. B* **1997**, *55*, 14163.

(240) de Gennes, P. G. *Scaling Concepts in Polymer Physics*; Cornell University Press: New York, 1979.

(241) Stauffer, D. *Phys. Rep.-Rev. Sec. Phys. Lett.* **1979**, *54*, 1.

(242) Arbabi, S.; Sahimi, M. *Phys. Rev. Lett.* **1990**, *65*, 725.

(243) Arbabi, S.; Sahimi, M. *Phys. Rev. B* **1993**, *47*, 695.

(244) Sahimi, M. *Applications of Percolation Theory*; Taylor and Francis: London, 1994.

(245) Tüzel, E.; Özmetin, M. S.; Yylmaz, Y.; Pekcan, Ö. *Eur. Polym. J.* **2000**, *36*, 727.

(246) Alexander, S.; Orbach, R. *J. Phys. (Paris), Lett.* **1982**, *43*, L625.

(247) Rehage, H.; Schnabel, E.; Veyssie, M. *Makromolekulare Chemie-Macromolecular Chemistry and Physics* **1988**, *189*, 2395.

(248) Burger, A.; Leonhard, H.; Rehage, H.; Wagner, R.; Schwoerer, M. *Macromol. Chem. Phys.* **1995**, *196*, 1.

(249) Rehage, H.; Veyssie, M. *Angew. Chem.-Int. Edit. Engl.* **1990**, *29*, 439.

(250) Sacchetti, M.; Yu, H.; Zografi, G. *Rev. Sci. Instrum.* **1993**, *64*, 1941.

(251) Rolandi, R.; Dante, S.; Gussoni, A.; Leporatti, S.; Maga, L.; Tundo, P. *Langmuir* **1995**, *11*, 3119.

(252) Leblanc, R. M. In.

(253) Gehlert, U.; Vollhardt, D. *Langmuir* **1997**, *13*, 277.

(254) Wen, J. Y.; Wilkes, G. L. *Chem. Mater.* **1996**, *8*, 1667.

(255) Judeinstein, P.; Sanchez, C. *J. Mater. Chem.* **1996**, *6*, 511.

(256) Ulman, A. *Chem. Rev.* **1996**, *96*, 1533.

(257) Vallant, T.; Kattner, J.; Brunner, H.; Mayer, U.; Hoffmann, H. *Langmuir* **1999**, *15*, 5339.

(258) Wasserman, S. R.; Whitesides, G. M.; Tidswell, I. M.; Ocko, B. M.; Pershan, P. S.; Axe, J. D. *J. Am. Chem. Soc.* **1989**, *111*, 5852.

(259) Silberzan, P.; Leger, L.; Ausserre, D.; Benattar, J. J. *Langmuir* **1991**, *7*, 1647.

(260) Allara, D. L.; Parikh, A. N.; Rondelez, F. *Langmuir* **1995**, *11*, 2357.

(261) Parikh, A. N.; Allara, D. L.; Azouz, I. B.; Rondelez, F. *J. Phys. Chem.* **1994**, *98*, 7577.

(262) Davidovits, J. V.; Pho, V.; Silberzan, P.; Goldmann, M. *Surf. Sci.* **1996**, *352*, 369.

(263) Segre, C. U.; Leyarovska, N. E.; Chapman, L. D.; Lavender, W. M.; Plag, P. W.; King, A. S.; Kropf, A. J.; Bunker, B. A.; Kemner, K. M.; Dutta, P.; Duran, R. S.; Kaduk, J. In *Synchrotron Radiation Instrumentation: Eleventh Us National Conference*; Piero Pianetta, J. A., Sean Brennan, Ed.; American Institute of Physics: Stanford, 2000; Vol. 521, pp 419.

(264) Carino, S. R.; Tostmann, H.; Underhill, R. S.; Logan, J.; Weerasekera, G.; Culp, J.; Davidson, M.; Duran, R. S. *J. Am. Chem. Soc.* **2001**, *123*, 767.

(265) Shibata, T. In *MRCAT Documentations for Users*, 1998.

(266) National Institute of Standards & Technology In: Gaithersburg, MD, 2000.

(267) Weerasekera, G. In *Chemistry*; University of Florida: Gainesville, 2000; pp xiv.

(268) Lavender, W. M. In *Synchrotron Radiation Instrumentation: Eleventh Us National Conference*; Piero Pianetta, J. A., Sean Brennan, Ed.; American Institute of Physics: Stanford, 2000; Vol. 521, pp 332.

(269) Fontaine, P.; Goldmann, M.; Rondelez, F. *Langmuir* **1999**, *15*, 1348.

(270) Tippmann-Krayer, P.; Kenn, R. M.; Mohwald, H. *Thin Solid Films* **1992**, *210*, 577.

(271) Daillant, J.; Alba, M. *Reports on Progress in Physics* **2000**, *63*, 1725.

(272) Kenn, R. M.; Bohm, C.; Bibo, A. M.; Peterson, I. R.; Mohwald, H.; Als-Nielsen, J.; Kjaer, K. *J. Phys. Chem.* **1991**, *95*, 2092.

(273) Seul, M.; Eisenberger, P.; McConnell, H. M. *Proc. Natl. Acad. Sci.* **1983**, *80*, 5795.

(274) Barton, S. W.; Thomas, B. N.; Flom, E. B.; Rice, S. A.; Lin, B.; Peng, J. B.; Ketterson, J. B.; Dutta, P. *J. Chem. Phys.* **1988**, *89*, 2257.
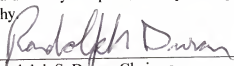
(275) Sinnamon, B. F.; Dluhy, R. A.; Barnes, G. T. *Colloid Surf. A-Physicochem. Eng. Asp.* **1999**, *146*, 49.

(276) Alonso, C.; Blaudez, D.; Desbat, B.; Artzner, F.; Berge, B.; Renault, A. *Chem. Phys. Lett.* **1998**, *284*, 446.

(277) Brezesinski, G.; Dietrich, A.; Struth, B.; Bohm, C.; Bouwman, W. G.; Kjaer, K.; Mohwald, H. *Chem. Phys. Lipids* **1995**, *79*, 145.

(278) Rapp, G.; Koch, M. H. J.; Hohne, U.; Lvov, Y.; Mohwald, H. *Langmuir* **1995**, *11*, 2348.

(279) Foran, G. J.; Peng, J. B.; Steitz, R.; Barnes, G. T.; Gentle, I. R. *Langmuir* **1996**, *12*, 774.

(280) Foran, G. J.; Garrett, R. F.; Gentle, I. R.; Creagh, D. C.; Peng, J. B.; Barnes, G. T. *J. Synchrot. Radiat.* **1998**, *5*, 500.

(281) Foran, G. J.; Gentle, I. R.; Garrett, R. F.; Creagh, D. C.; Peng, J. B.; Barnes, G. T. *J. Synchrot. Radiat.* **1998**, *5*, 107.

(282) Kim, I.; Rabolt, J. F.; Stroeve, P. *Colloids and Surfaces A: Physicochemical and Engineering Aspects* **2000**, *171*, 167.

(283) Viitala, T.; Peltonen, J. *Biophys. J.* **1999**, *76*, 2803.

(284) Lin, B.; Peng, J. B.; Ketterson, J. B.; Dutta, P.; Thomas, B. N.; Buontempo, J.; Rice, S. A. *J. Chem. Phys.* **1989**, *90*, 2393.

(285) Kaganer, V. M.; Brezesinski, G.; Mohwald, H.; Howes, P. B.; Kjaer, K. *Phys. Rev. E* **1999**, *59*, 2141.

(286) Riviere, S.; Henon, S.; Meunier, J.; Schwartz, D. K.; Tsao, M. W.; Knobler, C. M. *J. Chem. Phys.* **1994**, *101*, 10045.

(287) Ernst, M. H.; Hendriks, E. M. In *Kinetics of Aggregation and Gelation*; Family, F., Landau, D. P., Eds.; Elsevier Science Publishers, B. V: Amsterdam, 1984.
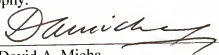
BIOGRAPHICAL SKETCH

Stephen Carino was born in the Philippines, on January 23, 1970. He obtained his bachelor's degree in chemistry in 1991 at the University of Nueva Caceres, receiving magna cum laude honors. While preparing for the national licensure examination for chemists the following year, he enrolled in the chemistry graduate program at the University of the Philippines at Diliman (UPD). During his stay at UPD, he worked as a research assistant on various projects at the Natural Sciences Research Institute. It was also during his stay in UPD that he met his future wife Czarina. After completing his master's degree in 1996, he left the Philippines to pursue a PhD degree at the University of Florida where he joined the research group of Dr. Randy Duran. His current interests are in the area of interfacial and colloidal physical chemistry.

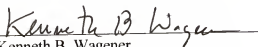Stephen and Czarina have a son, Aaron Derek, born on September 16, 1999.

I certify that I have read this study and that in my opinion it conforms to acceptable standards of scholarly presentation and is fully adequate, in scope and quality, as a thesis for the degree of Doctor of Philosophy.

Randolph S. Duran, Chairman
Associate Professor of Chemistry

I certify that I have read this study and that in my opinion it conforms to acceptable standards of scholarly presentation and is fully adequate, in scope and quality, as a thesis for the degree of Doctor of Philosophy.

David A. Micha
Professor of Chemistry and Physics

I certify that I have read this study and that in my opinion it conforms to acceptable standards of scholarly presentation and is fully adequate, in scope and quality, as a thesis for the degree of Doctor of Philosophy.

Kenneth B. Wagener
Professor of Chemistry

I certify that I have read this study and that in my opinion it conforms to acceptable standards of scholarly presentation and is fully adequate, in scope and quality, as a thesis for the degree of Doctor of Philosophy.

Dinesh O. Shah
Professor of Chemical Engineering

I certify that I have read this study and that in my opinion it conforms to acceptable standards of scholarly presentation and is fully adequate, in scope and quality, as a thesis for the degree of Doctor of Philosophy.

C. Russell Bowers
Associate Professor of Chemistry

This dissertation was submitted to the Graduate Faculty of the Department of Chemistry in the College of Liberal Arts and Sciences and to the Graduate School and was accepted as partial fulfillment of the requirements for the degree of Doctor of Philosophy.

August 2002

_____
Dean, Graduate School